The Physics of Negative Refraction and Transformation Optics

by

Wei Hsiung Wee

Thesis submitted for the degree of

Doctor of Philosophy

Condensed Matter Theory Group

Department of Physics

Imperial College London

June 2011

Declaration of Originality

This thesis is a result of the author's own work.
All other work contained within
are appropriately referenced
to the best of the author's knowledge.

Abstract

Whilst optics is one of the oldest field in science, there are still aspects of electromagnetism that we are only beginning to uncover. For instance, it was demonstrated that materials with simultaneously negative permittivity and permeability exhibit certain exotic behavior; where familiar physical phenomena, such as refraction, are reversed. As such, these materials came to be known as negative refractive index materials (NRIM) and their collective properties as negative refraction. One of the most important and remarkable property of NRIM is perfect lensing - the ability to transport both supra and sub-wavelength optical information from one surface (object plane) to another (image plane), forming images with unprecedented resolution, beyond the diffraction limit. Perfect lensing itself is a consequence of deeper symmetries in electromagnetism, encapsulated in the language of transformation optics - with which we have both a descriptive tool to unify diverse electromagnetic configuarations, as well as a prescriptive tool to design media which bends light at will. While, such transformation medium and NRIM have been demonstrably realised using metamaterials, several challenges remain, of which loss is the major challenge.

It is therefore under this trinity of concepts: metamaterials, negative refraction and transformation optics that this thesis is presented. In particular, this thesis illustrates the convergence of the later two concepts, giving rise to a novel class of perfect lens - the compact perfect lens. Here, we shall investigate, their unique properties, construction, challenges, and the dynamics of these lenses. In particular the formulation to study dynamics and effects of losses, is universal; applicable to lenses of any geometry. Finally we shall also propose an alternative universal, top-down approach to overcome losses in perfect lenses using phase conjugation, and demonstrate the capacity of such lenses to see through lossy, translucent obstacles.

Contents

List of Figures **11**

List of Tables **15**

List of Publications **17**

Acknowledgement **19**

Abbreviations and acronyms **21**

1 Introduction **23**

1.1 Historical perspective 23

1.2 Objective of report 26

2 Negative refraction **29**

2.1 Negative refractive index 29

2.2 Properties of negative refraction 31

2.2.1 Backward waves 31

2.2.2 Perfect lens 32

2.2.3 Negative Goos-Hanchen shift 34

2.2.4 Negative Doppler shift and Cherenkov effect 35

2.3 Thermodynamics and the necessity for dispersion 36

2.4 Criterion and terminology for negative refraction 38

3 Homogenisation and metamaterials **41**

3.1 Homogenisation 41

3.1.1 Length and time scales 42

3.1.2 Effective medium parameters 44
3.2 Metaparticles 46
3.2.1 Electric metaparticles ($\epsilon < 0$) 47
3.2.2 Magnetic metaparticles ($\mu < 0$) 49
3.2.2.1 Why are magnetic metaparticles necessary? 49
3.2.2.2 Split-ring resonators 51
3.2.2.3 Scaling to higher frequencies and limitations 52
3.2.2.4 Magneto-electric coupling 54
3.2.3 Negative refractive index materials 55

4 Perfect lens theorem and transformation optics 57
4.1 Perfect lens theorem 57
4.1.1 Statement of theorem 57
4.1.2 Proof of theorem 58
4.1.3 Consequence of Theorem 59
4.2 Transformation optics 61
4.2.1 General covariance begets transformation optics 62
4.2.2 Transformation media 64
4.2.3 Anisotropy in transformation 66
4.2.4 Minimising anisotropy - beyond the quasi-conformal transformation 67
4.3 Generalised PLT 70

5 Applications of the compact perfect lens I 73
5.1 What are super-scatterers? 74
5.2 Constructing the super-scatterer 75
5.2.1 Example - a cylindrical SS 77
5.3 Methods of analyzing scattering 79
5.3.1 Ray optics 79
5.3.2 Full wave solution 82
5.3.3 The localization principle 85
5.4 Scattering of a super-scatterer 86
5.4.1 Transparent super-scatterer 86

5.4.2 Absorber SS 88
5.4.3 Retro-reflector SS 91
5.4.3.1 Principles of retro-reflection 91
5.4.3.2 Results 93
5.5 Concluding remarks 96

6 Applications of the compact perfect lens II **99**
6.1 What are super phase arrays? 99
6.2 SPA and beam-forming 100
6.2.1 Phase array + transparent SS = SPA 100
6.2.2 N-array and beam-forming 102
6.3 Analytical model 103
6.3.1 Addition theorem 103
6.3.2 Transfer matrices 105
6.3.3 Resolving divergences 106
6.4 Results 108
6.4.1 Single displaced antenna 109
6.4.2 N-array antenna 110
6.4.2.1 Beam steering 111
6.4.2.2 Beam focusing 112
6.5 Concluding remarks 113

7 Dynamics of the perfect lens **115**
7.1 Model of a lossy dispersive lens 115
7.2 Simplification via symmetry 116
7.3 General solution of perfect lens 120
7.4 Equivalence to simple harmonic oscillators 121
7.5 Dynamics and limits of *any* perfect lens 123
7.6 Examples 124
7.6.1 Flat perfect lens 124
7.6.2 Cylindrical perfect lens 125
7.7 Concluding remarks 126

8 Overcoming losses - phase conjugate lens **129**

8.1 Strategy 130

8.2 Relationship between eigensolutions 132

8.3 Proof of strategy 133

8.4 Examples and applications 137

8.5 Summary of requirements 139

8.6 Experimental setup 142

8.6.1 Phase conjugation sheet 142

8.6.2 Further simplification 144

8.7 Concluding remarks 146

9 Conclusion **149**

A Appendix **155**

A.1 Dispersion of wire-mesh 155

A.2 Dispersion of SRR 156

A.3 Group theoretical considerations in metamaterial design 157

A.4 Scattering coefficients of the SPA 158

A.5 Explicit calculation of elements of transmission matrices 159

A.6 Alternative calculation of overall transfer matrix 160

List of Figures

1.1 Summary of the structure and intent of report. 28

2.1 Illustration of negative refraction. 32
2.2 The flat perfect lens. 33
2.3 Negative Goos-Hanchen effect 34
2.4 Negative Doppler shift 35
2.5 Negative Cherenkov radiation 36

3.1 Illustration of the process of Homogenisation. 41
3.2 Length Scales to consider for homogenisation. 44
3.3 Pendry's averaging procedure. 46
3.4 Wire mesh array 48
3.5 Cross sectional view of split-ring resonators (SRR). 51
3.6 Negative refractive index metamaterials 55

4.1 Illustration of the perfect lens theorem. 59
4.2 A complementary medium behaves like an optical antimatter. 60
4.3 Illustration of transformation optics. 65
4.4 Degree of anisotropy depends on asymmetry/aspect ratio of transformed unit cells. 68
4.5 Improper transformation optics have to be used with care 71

5.1 Illustration of super-scatterer 75
5.2 Illustration of the creation of super scatterers. 76
5.3 Coordinate transformation for a cylindrical lens 77
5.4 Ray trajectories and full wave solutions of transparent SS 80

5.5 Effects of loss on a transparent SS 87
5.6 Effects of loss on an absorber SS 90
5.7 Figure of the relative reflected scattering coefficient $a_m^{(r)}$ as a function of the order m of the Bessel functions 91
5.8 Fig of the back-scattered field magnitude at infinity $|E|_\infty$, as a function of the radius d 93
5.9 Contour plot of $|E_z(r,\phi)|$ showing the retro-reflection of a retro-reflecting SS 94
5.10 Gain of RR SS as a function of back-scattered angle 95
5.11 Graph of back-scattered intensity $I_\infty(r \to \infty, \phi = \pi)$ as a function of loss δ in the NRIM. 96

6.1 Illustration of super phase array 101
6.2 Illustration of the addition theorem. 104
6.3 Illustration of transfer matrices 105
6.4 The problem of field divergences for a perfectly homogeneous perfect lens 107
6.5 Figure of ray and full wave solution of a single antenna SPA 110
6.6 Fig (a) and (b) shows the field amplitude $|E_z|$ as a function of x at a distance 111
6.7 Fig (a) shows the contour plot of a $N = 19$ SPA demonstrating beam steering 112
6.8 Fig (a) shows the contour plot of a $N = 19$ SPA demonstrating beam focusing 113

7.1 Fig (a) Figure of a *general* compact perfect lens ... Fig (b) schematic of the simplification of boundary conditions 117
7.2 Illustration of the analogy between the perfect lens and it's mechanical analogue. 123
7.3 Graph of transmission coefficient $T_m(\omega_0)$ as a function of loss σ for the cylindrical perfect lens. 125
7.4 Time evolution of an image using a Cylindrical Perfect Lens (losses, $\sigma = 1.8 \times 10^{-3}$). 127

8.1 Illustration of the strategy for PCL 131
8.2 Fig (a) illustrates the relationship between the eigenmodes on both sides of the PCS ... Fig (b) shows the effect of channel mixing in general 134
8.3 Illustration of the various matrices in section 8.3 135
8.4 Numerical experimental setup of PCL 139
8.5 Numerical results (a)-(d) corresponding to the setup in Fig 8.4 . . . 140
8.6 Illustration of the perfect PCL. 141
8.7 Schematics of the PCS based on Aubry's design 145
8.8 Simplification to design of PCL 146
8.9 A PCL design *without* forward PC 147

A.1 Illustration of the various matrices used in section A.6 161

List of Tables

8.1 Requirements for constructing a PCL. 141
8.2 Comparison between a conventional NRIM PL and a PCL 142

List of Publications

Portions of this thesis have been drawn from the following publications:

Wee WH and Pendry JB, "Shrinking optical devices" *New Journal of Physics*, **11** 73033-56, (2009)

Wee WH and Pendry JB, "Super phase array" *New Journal of Physics*, **12** 033047, (2010)

Wee WH and Pendry JB, "Looking beyond the perfect lens" *New Journal of Physics*, **12** 053018, (2010)

Wee WH and Pendry JB, "Universal evolution of perfect lenses" *Phys Rev Lett*, **106** 165503, (2011)

Acknowledgement

This thesis would not have been possible apart from the encouragement, support and guidance of the following people to whom the author is very much grateful. First, I would like to thank my supervisor professor Sir John Pendry, who is one of the pioneers of this field, for his patience and superb guidance. Professor Pendry has an amazing depth of knowledge in many other areas of physics as well. This, together with his impeccable ability to explain complex concepts in very simple terms, that is not only understandable but also very illuminating, makes learning physics from him both very rewarding and inspirational. Besides his skills as a teacher, professor Pendry also has an amazing power of intuition. Very often, even if he does not know the details of a problem, he would be able to guess the approximate solution. Much of my work would have ended in dead ends if not for his timely guidance.

Other than my mentor, I would like to thank my family for their love, support and encouragement. In particular I like to thank my wife, Bee Him, for her many sacrifices. She has always been there for me, always patient, always willing to lend me a ear, and always a source of strength. Other than my wife, I would also like to dedicate this work to my children. I hope this piece of work may open a very small window to the wonderful world of physics for them.

I would also like to take this opportunity to thank my colleagues and friends at Imperial College, for all the fun and interesting discussions. In particular I would like to thank the members of the group (in no particular order of importance), Alexandre Aubry, Yonathan Sivan, Antonio Fernandez, Angela Demitriadou, Miguel Navarro, Yu Luo and David Milson, for the many illuminating discussions through which I have a better understanding of Metamaterials.

I am also very grateful to my sponsors, DSO National Laboratories (Singapore), for their more than adequate financial support all these years. I hope this work would be useful in some ways to my sponsors.

Finally, and most importantly I thank God for his manifold wisdom, from whom all things are made.

> *"The heavens declare the glory of God; the skies proclaim the work of his hands. Day after day they pour forth speech; night after night they display knowledge. There is no speech where their voice is not heard. Their voice goes out into all the earth, their words to the ends of the world." Psalms 19:1-4*

Indeed as the Psalmist say and I echo:

> *"O Lord, our Lord, how majestic is your name in all the earth!... When I consider your heavens, the work of your fingers,... what is man that you are mindful of him, the son of man that you care for him? ...O Lord, our Lord, how majestic is your name in all the earth!" Psalms 8*

Abbreviations and acronyms

Abbreviation	Meaning
ϵ	Permittivity
μ	Permeability
ASPP	Antisymmetric Surface Plasmon Polariton
CM	Complementary Media
CPL	Compact Perfect Lens
EM	Electromagnetic
LHM	Left Handed Material
NRIM	Negative Refractive Index Materials
PRIM	Positive Refractive Index Materials
PL	Perfect Lens
PLT	Perfect Lens Theorem
PC	Phase Conjugation
PCL	Phase Conjugate Lens
PCM	Phase Conjugation Mirror
PCS	Phase Conjugation Sheet
PEC	Perfect Electrical Conductor
RR SS	Retro-Reflector Super-Scatterer
SS	Super-Scatterer
SSPP	Symmetric Surface Plasmon Polariton
SPA	Super Phase Array
SRR	Split Ring Resonators
TO	Transformation Optics
WM	Wave Mixing

1. Introduction

1.1 Historical perspective

In 1873, Maxwell wrote down his much acclaimed and famous set of equations [1], which unified both electric and magnetic phenomenon. This intertwined nature of electric and magnetic fields gave rise naturally to electromagnetic waves which Maxwell discovered to be traveling exactly at the speed of light in vacuum. It was then through a brilliant leap of intuition, that Maxwell drew one of the most important conclusions in physics - that light is an electromagnetic wave. The interaction of light with matter, therefore is encoded by the response of matter to electric and magnetic fields; and this response in turn is encapsulated by the constitutive equations, parameterised by ϵ and μ [1]. The speed by which light/EM waves traverse a medium is related to the refractive index, and through Maxwell's equations, the square of the refractive index is equal to the product of ϵ and μ. Since, trajectories of light propagation are paths which minimise the time of traversal (Fermat, 1657) [2], refractive index is an important concept in the design of geometrical optical devices. The choice of optical materials, then boils down to the choice of ϵ and μ.

While matter in general has a naturally strong response to electric fields, the same cannot be said of magnetic fields (except ferromagnets). Landau [3] argued that not only are magnetic response weak, most materials are also generally not magnetically dispersive, hence for all intent, Landau argued that one can safely regard $\mu(\omega) \sim 1$, and focus only on ϵ, in the description of light-matter interaction. Still in 1968, Vesalago [4] posed an interesting question, how will light behave in a material with simultaneously negative ϵ and μ? Vesalago demonstrated that *if* such a material does exist, then the phase front and power flow of light will point

[1] A more general response which includes Magneto-Electric responses, would be parameterised by Chirality and Tellegen parameters.

in opposing directions - essentially all intuitive physics of light propagation, such as Doppler effect, Cerenkov radiation and refraction, will be "reversed". Since such medium could be regarded as exhibiting an effective negative refractive index; they were termed as negative refractive index materials (NRIM) (see section 2.4). While Vesalago's proposed media, is physically interesting, the lack of optical materials which displays magnetic response, much less $\mu < 0$ behaviour, meant NRIM remained only as a philosophical curiousity, until recently.

In 1996, Pendry *et al* first proposed theoretically [5] and later demonstrated experimentally [6], how a composite composed of a periodic wire mesh structure embedded in a dielectric, behaves as an effective plasma, when the wavelength of light is much larger than the periodicity of the wire mesh. What was significant about this material was that by simply altering the geometric structure of the wire mesh, this media behaves as a material with a *controllable*, *effective* $\epsilon(\omega)$. Following this in 1999, Pendry [7] repeated the idea, replacing the wire mesh with an array of split ring resonators (SRR), he demonstrated that such a media display a significant, and similarly controllable magnetic response. Not only was such a media counterposed to Landau's argument, Pendry showed further that at some frequencies, this SRR media even behaves as a $\mu(\omega) < 0$ material. With the possibility of constructing composites which display an effective $\epsilon < 0$ and $\mu < 0$, Smith *et al* combined the wire mesh and the SRR together to experimentally realise the first NRIM [8, 9]. Since then various other micro-structures based on the same principle of homogenisation has been proposed and experimentally studied for NRIM: fishnet structures [10–13], nano-rod pairs [14], polaritonic and plasmonic spheres [15] and a similar approach using plasmonic spheres in a loop [16]; with the goal of pushing NRIM to optical frequencies (see references therein [17]).

The success of the wire mesh and SRR media rely on the general principle of homogenisation (effective medium theory) - when the incident EM wavelength is much longer than the inhomogenity of the media, such media may be regarded as effectively homogeneous. Such utility of homogenisation to obtain "designer" materials, thus gave birth to a new field of material engineering - metamaterials. While metamaterials lifted NRIM up from an abstract concept to a realisable material, it was not until the discovery of another truly remarkable property of NRIM that

arguably led to the explosion of interest in this field. In a seminal paper in 2000, Pendry [18] demonstrated that a slab of NRIM with $\epsilon = \mu = -1$, not only bends light rays to form an image, such a slab also restores the subwavelength optical information - evanescent near-fields, enabling images with unprecedented resolution below the diffraction limit. This slab of material was thus aptly termed as the "perfect lens" (PL). PL's capacity for subwavelength imaging, has since been demonstrated experimentally either partially (poor man's superlens) [19], (using swiss rolls) or fully (using transmission lines) [20–22]. This unusual ability, to manipulate both the propagating far-field and the evanescent near-field, makes the PL a very powerful imaging device. In 2003 Pendry *et al* [23], further generalised this PL effect, and viewed the effect of a PL as an *optical antimatter* which cancels the presence of its surrounding media. This new perspective enabled construction of PL with an additional magnifying effect [24–26], or PL which behaves as some form of remote cloaking device which cancels the scattering footprint of a nearby scattering object [27, 28].

Following the explosion of interest in negative refraction, another seminal paper in 2006, gave birth to a new branch of metamaterial engineering. In 2006 Pendry *et al* [29] made use of the principle of covariance [30] in electromagnetics [31] to propose a novel and systematic way of designing optical devices: given a predetermined coordinate transformation, Pendry *et al* was able prescribe a set of material parameters to bend EM fields at will - a method known as transformation optics. Although the methods used in transformation optics have been known and used in numerical EM problems to simplify calculations [32], the true novelty of the work in 2006 [29], was to regard such coordinate transformations as more than a mathematical perspective, but to regard them as actual *physical materials* which *effect* such coordinate transformations. Such an approach to device design is appealing, as there is now a systematic way to prescribe material parameters in order to obtain the desired control of EM fields. This is further augmented by the recent ability to design materials with the desired parameters *a-priori* via metamaterial engineering. The success of transformation optics has since been demonstrated experimentally in a variety of applications: from devices which renders objects invisible [29, 33, 34], guides plasmons around bends [35], to novel re-design of aberration-free, ultrawide

angle lenses [36, 37] and so on. While the fledgling field of metamaterial engineering has demonstrably much potential, several challenges still remain [38]. Of these, losses due to dissipation in materials remain one of the biggest challenge. Many novel effects from perfect lens for instance, are susceptible to losses. While some means to compensate losses have been suggested [39–45], it remains to be seen if these would be practical.

The field of metamaterial engineering is indeed vast. So far, we have only briefly touched on some of the early (major) elements which gave rise to this field, namely negative refraction, homogenisation (effective medium theory) and transformation optics. To fully explore the entire field would be beyond the scope of this report (see [38] for further overview). The intent rather is to re-visit the concepts of these major elements. The reason for this is two-fold. First, without a doubt, these elements which gave birth to the field, still form an important cornerstone of metamaterials. For the field to persist, it is important to address some of the key challenges. In turn to address these challenges it is important to understand the concepts behind the elements underpinning this field. The second reason, is the concepts of negative refraction and transformation optics are interesting on their own. Beyond the practical, the concepts of negative refraction and transformation optics has indeed revitalised the interest in what had been previously thought complete EM theory. It is under this backdrop, that we present our contribution to this field of metamaterial engineering. In particular, we shall focus on the convergence of negative refraction and transformation optics, the phenomenon which arguably opened the floodgates of interest to the field of metamaterias: perfect lensing.

1.2 Objective of report

This report is broadly divided into 5 parts with the following intent:

- The first part (chapters 2 and 3), is to introduce some background concepts, about *negative refraction* and how we can make materials which exhibit negative refraction through *metamaterials*.

- The second part (chapter 4), is to introduce a prescription: *perfect lens theorem* and *transformation optics*; through which we can systematically design devices.

- The third part (chapters 5 and 6), is to demonstrate applications of some of these devices, namely *perfect lenses*.

- The fourth part (chapter 7), is to introduce a general *analytical framework* whereby we can understand the fundamental *physical* limits to these devices. For instance how do these devices evolve in time, and how are such devices affected by realistic losses.

- And finally (chapter 8), is to revisit the basic concepts, and propose a paradigm shift - introducing an alternative way to make these devices.

The structure and intent of this report then is liken to be a "factory", where we take concepts and we develop them to be devices (fig 1.1). Because of the depth and the breadth of metamaterials research, space do not permit us to present the entire field nor illustrate all the examples of how concepts are translated to devices. While each chapter strives to be independent and cover general concepts in metamaterials research, even beyond the principal intent of this report; the main focus of this report is this: how are concepts like *negative refraction* and *transformation optics* translated to a remarkable type of imaging device - *perfect lenses*.

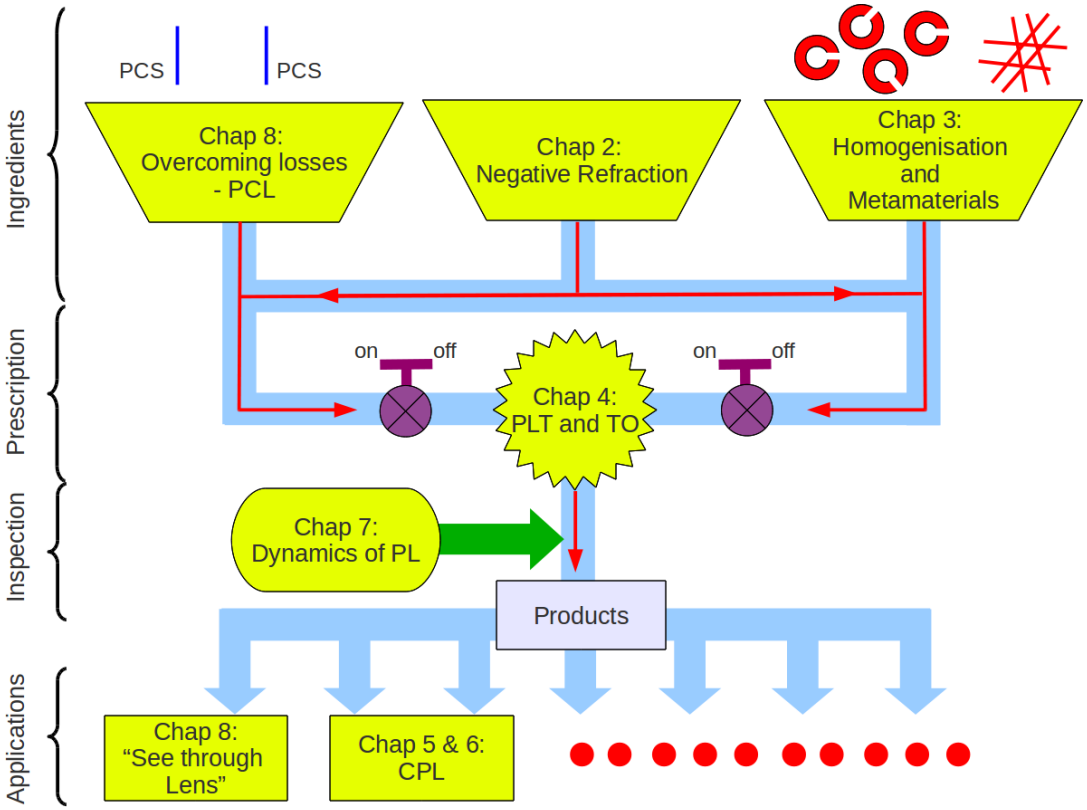


Figure 1.1: Summary of the structure and intent of report. This is liken to be a “metamaterials-factory”, where we take concepts and develop them into applications.

2. Negative refraction

2.1 Negative refractive index

For an isotropic homogeneous transparent material, Maxwell's equations can be reduced to a single Helmholtz equation, $(\nabla^2 + k^2)\mathbf{E} = 0$, which admits wave like solutions, $|\mathbf{E}| \propto \exp(\pm i\mathbf{k}.\mathbf{x} - i\omega t)$ with wave-vector $\mathbf{k}$. The "magnitude"[1] of this wavevector is given by $k = n.\omega/c$, and we can identify a quantity - the (complex) *refractive index* as:

$$n = \pm\sqrt{\epsilon\mu} \tag{2.1}$$

where ϵ is the permittivity and μ is the permeability of the medium. The choice of sign for the square root depends on the sign of $\Re(\epsilon)$, $\Re(\mu)$; and it is determined by causality and radiation condition. As we shall see this choice is not merely a mathematical construct but has physical origins and consequently significant physical implications.

First, we shall demonstrate how to determine a causally sensible sign for n. Usually for most transparent materials, $\Re(\epsilon)$ and $\Re(\mu)$ take positive values, as such n can be taken unambigiously as $+\sqrt{\epsilon\mu}$. However in 1967, when Vesalago [4] considered the case of a media that has both negative $\Re(\epsilon)$ and $\Re(\mu)$, he concluded that such a material would necessarily take a negative value. To prove this point, consider the following. In general ϵ and μ are complex quantities, where $\Im(\epsilon)$ and $\Im(\mu)$ are a measure of losses/gain. For a *passive* material it can be shown that thermodynamics constrain[2] $\Im(\epsilon)$, $\Im(\mu) > 0$. However there are no physical constraints on the sign

[1] Conventional definition of magnitudes are positive definite; though we can relax this constraint and allow negative and even complex magnitudes.

[2] The total amount of electromagnetic energy dissipated a medium is then given by [3] pg 274,

$$\int_{-\infty}^{\infty} Q dt = \int_{-\infty}^{\infty} d\omega \oint_V \mathbf{d^3x}[\omega(\Im(\epsilon)\epsilon_0|\mathbf{E}|^2 + \Im(\mu)\mu_0|\mathbf{H}|^2)]$$

If such a material is passive, hence naturally dissipative then $Q > 0$. This implies that for all passive

of $\Re(\epsilon)$, $\Re(\mu)$. Suppose an electromagnetic plane wave enters at normal incidence to a semi-infinite medium (filling up the half space $z \geq 0$), with $\epsilon = \epsilon' + i\epsilon''$ and $\mu = \mu' + i\mu''$. By causality, a causally sensible solution would be one in which the electromagnetic fields decay to zero as $z \to \infty$. Now consider such a material to have small amount of losses so that $|\epsilon'|, |\mu'| \gg \epsilon'', \mu''$, then from Taylor expansion:

$$\begin{aligned} \sqrt{\epsilon\mu} &= \sqrt{(\epsilon' + i\epsilon'')(\mu' + i\mu'')} \\ &\approx s(\left|\sqrt{\epsilon'\mu'}\right| + \frac{i}{2\left|\sqrt{\epsilon'\mu'}\right|}(\epsilon'\mu'' + \mu'\epsilon'')) \end{aligned} \tag{2.2}$$

where $s = \pm 1$, and the sign of s is determined by causality. For a causally sensible solution the second term in eqn (2.2) has to be greater than zero[3]. This together with the earlier consideration imply the following conditions have to be satisfied for a causally sensible solution

$$\begin{aligned} s(\epsilon'\mu'' + \mu'\epsilon'') &> 0, \\ \epsilon'', \mu'' &> 0 \end{aligned} \tag{2.3}$$

If $\epsilon', \mu' > 0$ then $s = +1$ and this corresponds to the standard positive refractive index[4]. If $\epsilon', \mu' < 0$ then $s = -1$ which corresponds to Vesalago's media which we shall call *negative refractive index material* (NRIM)[5].

So why is the sign of n important? If we disregard dispersion for the moment and solve the Green's function of the Helmholtz equation we would get $G^{\pm}(\mathbf{x}, t; \mathbf{x}', t') = \delta(t' - \left[t \mp \frac{R}{nc}\right]).\frac{1}{R}$, where $R = |\mathbf{x} - \mathbf{x}'|$ is the distance of separation and G^+ is the retarded Green's function (or the causal Green's function for a source at $\mathbf{x}'$) [2]. What this means is that an effect observed at the point $\mathbf{x}$ at time t is caused by the action of a source at a distance R away at an earlier or retarded time $t' = t - R/nc$. Thus for $n > 0$ the disturbance/phase fronts propagate outwards from the source with time. When $n < 0$ the roles of G^+ and G^- are switched, so the disturbance/phase fronts propagate inwards instead. This reversal of phase propagation has profound

isotropic homogenous materials $\Im(\epsilon)$, $\Im(\mu) > 0$. This restriction does not hold for active media.

[3] An incident wave at an interface has to decay away from the interface. This is satisfied only for $\Im(\sqrt{\epsilon\mu}) > 0$.

[4] Such materials are called *positive refractive index material* (PRIM)

[5] Although the above argument for choice of sign, holds true only for passive materials with small $\Im(\epsilon)$ and $\Im(\mu)$, this can be generalised for any complex ϵ and μ (including active media) using similar causality arguments [46].

significance for physical phenomena such as Doppler shifts and Cherenkov radiation (as we shall see later).

An important point to note is this reversal does not violate causality as we shall see later because, firstly NRIM are necessarily dispersive (section 2.3) and therefore take time to be established (chapter 7); secondly the direction of phase fronts are counterposed to the direction of energy propagation. On the second point this means that while phase fronts move inwards, power flow outwards satisfying causality.

2.2 Properties of negative refraction

2.2.1 Backward waves

As briefly hinted at in the previous section, one of the signature property of NRIM is that it supports *backward waves*; waves where the direction of phase propagation (phase velocity $\mathbf{v_p}$) is counterposed to the direction of power flow (group velocity $\mathbf{v_g}$). For an isotropic homogeneous material, Maxwell's equations is given by:

$$\mathbf{k} \times \mathbf{E} = \omega\mu\mu_0\mathbf{H} \tag{2.4}$$

$$\mathbf{k} \times \mathbf{H} = -\omega\epsilon\epsilon_0\mathbf{E} \tag{2.5}$$

we can easily see that a negative ϵ, μ implies that the phase vector $\mathbf{k}$ (collinear with $\mathbf{v_p}$) is in the reverse direction compared to the Poynting vector $\mathbf{S} = \mathbf{E} \times \mathbf{H}$ (collinear with $\mathbf{v_g}$) implying therefore that a NRIM does indeed support such "backward waves" ($\mathbf{v_p}.\mathbf{v_g} < 0$ or equivalently $\Re(\mathbf{k}).\langle\mathbf{S}\rangle < 0$ [6]). In addition we note that for negative ϵ, μ, the vectors $\mathbf{E}, \mathbf{H}, \mathbf{k}$ now forms a left-handed triad compared to a PRIM (see fig 2.1(a)). Hence NRIM are also commonly known as *'left-handed materials'* (LHM).

One of the first immediate consequence of the presence of backward waves is the modification of Snell's law of refraction. By imposing phase matching at the interface[7] (matching tangential $\mathbf{k}$) between a PRIM and a NRIM, one can show that the optical rays obeys the 'reverse' Snell's law

$$n_+ \sin(\theta_+) = -|n_-| \sin(\theta_-) \tag{2.6}$$

[6] The angle brackets $\langle\rangle$ represents time averaging

[7] This is equivalent to the more general boundary condition - field continuity - that is matching the tangential $\mathbf{E}$ and $\mathbf{H}$ fields at boundaries

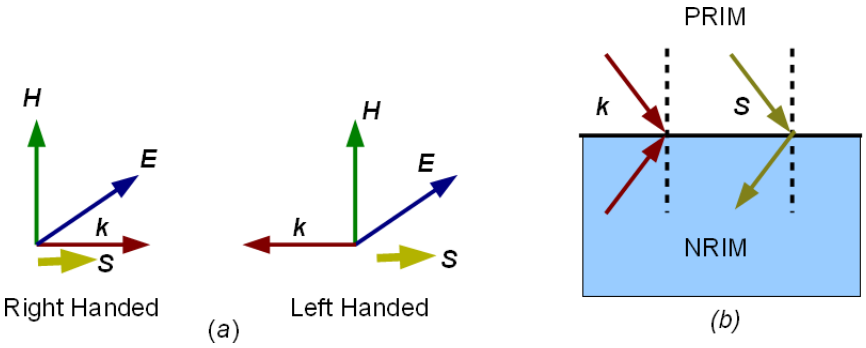


Figure 2.1: Illustration of negative refraction. Fig (a) the $\mathbf{E}, \mathbf{H}, \mathbf{k}$ vector triads forms a right handed set in a PRIM and a left handed set in a NRIM. Fig (b) by matching the wave vector $\mathbf{k}$ at the interface, we can show that light rays bend away from the normal when incident on a PRIM-NRIM interface. The power flow or Pontyning vector, $\mathbf{S}$ is always away from the interface.

with optical rays bending in the opposite direction as compared to a conventional PRIM to PRIM refraction, hence justifying the term negative refraction[8] (see fig 2.1(b)).

2.2.2 Perfect lens

Using the modified Snell's law (eqn (2.6)) and ray tracing, we can easily show that a flat slab of NRIM material with $\epsilon = \mu = -1$ would behave as a lens for imaging (fig 2.2(a)). If that was all there is to it, then such a slab would simply belong to a class of peculiar but pointless lens. Since conventional lenses can only refract propagating light rays, which carries spatial information up to a wavelength λ, of light, this loss of information from the evanescent near fields implies that images from conventional lenses have a resolution limited by λ - a limit typically known as the diffraction limit[9]. The slab NRIM lens, however, was shown not only to refract

[8]Snell's law can also be extended for more general anisotropic materials as well. In general the choice of refraction angle at an interface of any material is determined by imposing phase matching (matching tangential $\mathbf{k}$) and conservation of energy ($\nabla.\mathbf{S} = 0$, i.e. power flow away from interface/power flow points in the same direction away from source)

[9]The E-field at the image plane $E(x', y', z')$, is related to the E-field at the object plane $E(x, y, 0)$ by $E(x', y', z') = \iint_{-\infty}^{\infty} dk_x dk_y \tilde{E}(k_x.k_y) \exp\left(-ik_x x' - ik_y y' - i\sqrt{k_0^2 - k_x^2 - k_y^2}.z'\right)$ where $\tilde{E}(k_x.k_y) = \iint_{-\infty}^{\infty} dxdyE(x, y, 0) \exp(ik_x x + ik_y y)$ is the Fourier transform of $E(x, y, 0)$. It can be seen that spectral information is carried by 2 channels. When $\sqrt{k_0^2 - k_x^2 - k_y^2} \geq 0$ spectral informa-

light rays, but also focus and restore evanescent near fields (fig 2.2(b)), enabling images with unprecedented resolution [18].

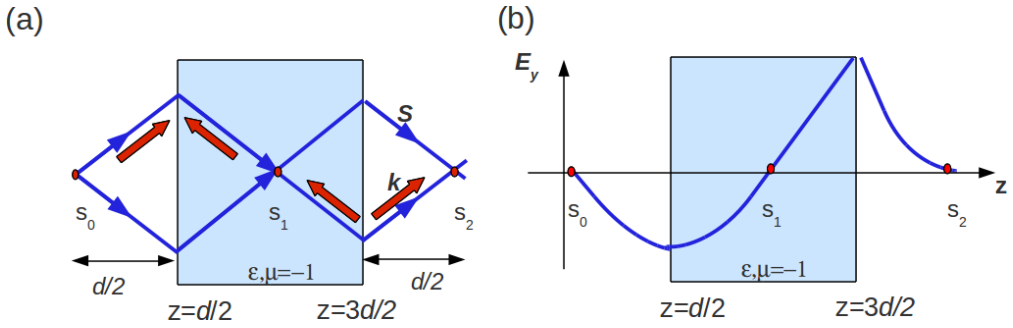


Figure 2.2: The flat perfect lens. Fig (a) ray tracing shows how the flat slab focuses the propagating far fields through negative refraction and phase reversal. Blue arrows denote Poynting vectors while red arrows denote wave vectors. Fig (b) shows the restoration of the near fields. Together the flat perfect lens can form a perfect image of s_0 at $s_1$and s_2.

Because of this remarkable property to break the diffraction limit such a slab was aptly termed and known as the *perfect lens.* As we shall see later, the concept of the perfect lens could be generalised from the simple $\epsilon = \mu = -1$ case to a more generalised perfect lens via the *perfect lens theorem* (section 4.1). We would also see that a perfect lens can be viewed as an *optical antimatter* (or *complementary media*) to the surrounding medium with the ability to cancel out the effects of light propagation in the latter. If the surrounding media is made up of PRIM then the perfect lens would necessarily have to be composed of NRIM. This optical complementarity has also been exploited recently to construct devices which can cancel out the scattering footprint of nearby objects enabling "cloaking at a distance" [27], and optical illusion devices [28].

tion is carried by propagating waves (fig 2.2(a)), conversely when $\sqrt{k_0^2 - k_x^2 - k_y^2} < 0$ by evanescent near fields (fig 2.2(b)). Since only the former can carry information to the far-field and since a spectral component with (k_x, k_y) would carry spatial information corresponding to $\Delta x \sim 2\pi/k_x$, $\Delta y \sim 2\pi/k_y$; therefore only spatial information up to $\Delta x, y \sim 2\pi/k_0$ can be carried to the far-field. This loss of spatial information by the evanescent near fields is known as the diffraction Limit.

2.2.3 Negative Goos-Hanchen shift

Another consequence of the existence of backward waves in NRIM is the negative Goos-Hanchen shift [47].

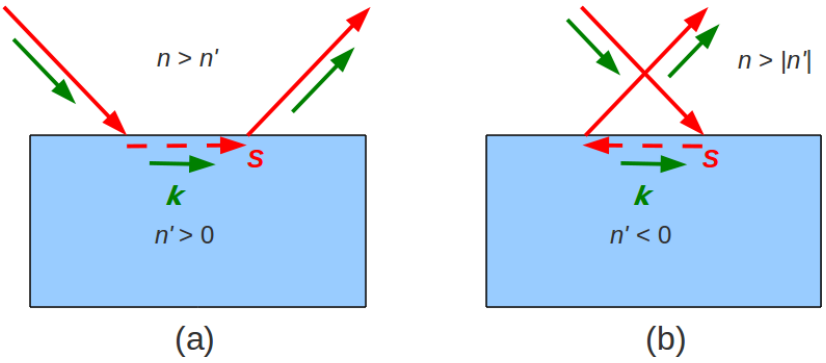


Figure 2.3: Fig (a) a light ray undergoing total internal reflection would acquire a "forward" lateral phase shift known as Goos-Hanchen effect. **S** is the Poynting vector and **k** is the wavevector. Fig (b) a negative Goos-Hanchen effect is observed when the lower index material is a NRIM. The shift is now "backwards".

Normally when light traverses from a medium of higher to lower refractive index ($n > n' > 0$) it would undergo total internal reflection when the incident angle is larger than the critical angle ($\theta_c = \sin^{-1}(\frac{n'}{n})$). In addition to the total internal reflection, the reflected light also aquires an additional phase factor dependent on the angle of incidence. This additional phase factor would cause a lateral spatial displacement of the reflected light ray, an effect commonly known as the Goos-Hanchen shift. This shift can be understood from the following. Firstly the total internal reflection is due to the fact that the lower index half space does not support propagating waves above the critical angle, hence no refracted ray exists. However the lower index half space does support propagating surface waves at the interface. These surface waves would re-emit back into the higher index half space which does support propagating waves, and these re-emitted waves would be the total internally reflected light (fig 2.3(a)). Because the wave vector and the Poynting vector of the surface waves are collinear, the reflected light is shifted in the same direction as the tangential wavevector at the interface. Now if the lower index material is switched to a NRIM (of same magnitude, $n' < 0$; $n > |n'| > 0$), then the presence of backward waves would result in the Goos-Hanchen shift being reversed (fig 2.3(b)).

This "backward" shift due to the negative Goos-Hanchen effect, has been exploited in creating light trapping devices capable in principle of slowing light pulse down to a complete standstill [48]. Such devices in turn can then be exploited as a new type of optical data storage devices.

2.2.4 Negative Doppler shift and Cherenkov effect

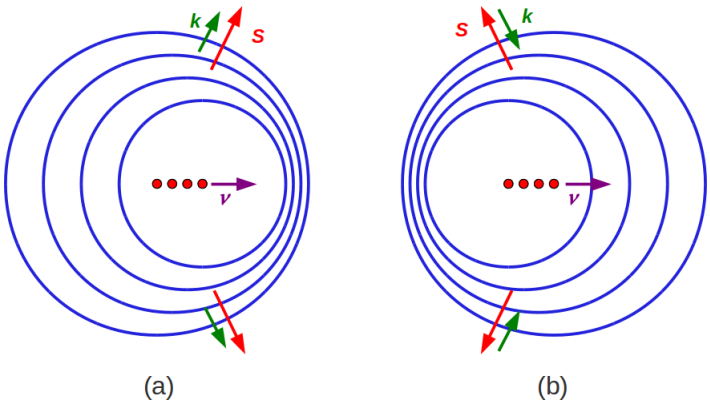


Figure 2.4: Fig (a) normal Doppler shift in a PRIM due to phase fronts propagating outwards. The moving source is denoted by the red spot. Fig (b) negative Doppler shift in a NRIM, due to backward waves, where phase fronts propagates inwards.

When a radiating point source (frequency ω_0) is moving, the frequency of the radiation observed by stationary observers would vary according to the position of the observers. If the source is moving towards the observer the measured frequency ω, would increase ($\omega > \omega_0$). Conversely a retreating source would register a lower frequency ($\omega < \omega_0$). This well known Doppler shift effect can be understood from the following. A source moving in a PRIM would emit spherical phase fronts which propagate outwards, the effect of the motion would result in consecutive phase fronts being compressed in the front of the source and stretched in the rear (see fig 2.4(a)). If the source is moving in a NRIM, then the reverse Doppler shift would be observed since the phase fronts would propagate inwards instead (fig 2.4(b)) [4].

Now when the velocity of the source ν, exceeds the speed of light in the medium that the source is travelling in ($\nu > nc$) we would see the wave fronts interfere constructively to form a cone of light which would point forward in the same direction as ν. This well known effect is known as Cherenkov radiation. If the media that

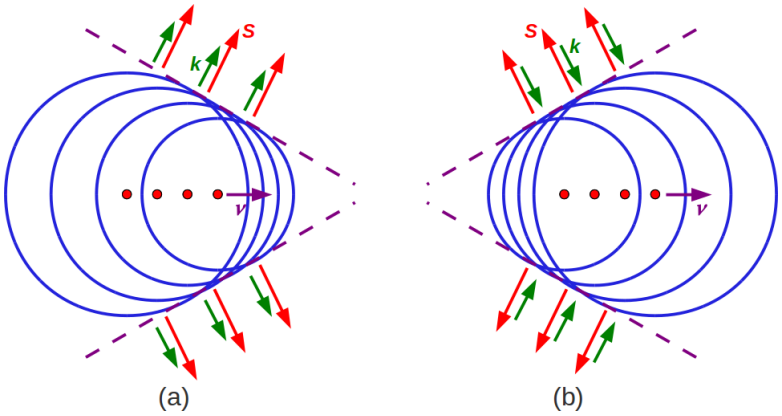


Figure 2.5: Fig (a) the dashed line signifies the wave front of the Cherenkov radiation. For a normal Cherenkov radiation the radiation cone points forward in the same direction as ν. Fig (b) negative Cherenkov radiation. Radiation cone is reversed.

the source is travelling in a NRIM, then again the presence of backward wave fronts would reverse this cone of light resulting in the negative Cherenkov radiation (fig 2.5) [4].

2.3 Thermodynamics and the necessity for dispersion

According to Poynting's theorem $\nabla.\mathbf{S} = \partial_t W$; where the Poynting vector is defined as $\mathbf{S} = \mathbf{E} \times \mathbf{H}$ and the rate of change of "work done by the electromagnetic field" is given by $\partial_t W = \dot{\mathbf{D}}.\mathbf{E} + \dot{\mathbf{B}}.\mathbf{H}$. For a non-dispersive body the electromagnetic internal energy, U, can be easily shown to be $U = W = \frac{1}{2}\left(\epsilon |\mathbf{E}|^2 + \mu |\mathbf{B}|^2\right)$. Since internal energy is positive ($U \geq 0$), this implies that for a non-dispersive body we cannot have $\epsilon < 0$, $\mu < 0$ simulatneously. In another words for NRIM to exist such a material has to be dispersive. This can be quantified more explicitly by the following. For a dispersive body, we can show[10] that $\partial_t W = \partial_t U + Q$; where Q is the rate of heat dissipated (see footnote 2), and the electromagnetic internal energy, U of the body

[10]The rate of work done $\partial_t W$ can be divided into two parts. Q is the rate of heat dissipated and U is the internal energy. This can be easily distinguished since U is a state function this means that U at $t = 0$ is the same as U at $t = T$ where T is the period of an Electromagnetic wave (that is $U(0) = U(T)$), while $\int_0^T Q dt \geq 0$.

is given by[11]:

$$U = \frac{1}{4}\frac{d}{d\omega}\left(\omega\left(\epsilon'(\omega)\left\langle|\mathbf{E}(t)|^2\right\rangle + \mu'(\omega)\left\langle|\mathbf{B}(t)|^2\right\rangle\right)\right) \geq 0 \tag{2.7}$$

where $\epsilon'(\omega) = \Re\left[\epsilon(\omega)\right]$ and $\mu'(\omega) = \Re\left[\mu(\omega)\right]$ and $\langle\rangle$ implies time average over a period $2\pi/\omega$. From eqn (2.7) and the requirement that $U \geq 0$, we can easily see that

$$\frac{d(\omega\epsilon'(\omega))}{d\omega} \geq 0, \quad \frac{d(\omega\mu'(\omega))}{d\omega} \geq 0 \tag{2.8}$$

Eqn (2.8) implies that if $\epsilon'(\omega) < 0$ then $\frac{d\epsilon'(\omega)}{d\omega} \geq -\epsilon'(\omega) > 0$ (similarly for μ'). In another words, based on thermodynamical arguments, for a NRIM to exist, it must be sufficiently dispersive. This necessity for dispersion is a very important result. Firstly dispersion implies that the phenomenon of negative refraction takes a finite time to develop. As we shall see later (chapter 7) the time it takes for negative refraction to be established is roughly inversely proportional to the the rate of dispersion, $\frac{d\epsilon'(\omega)}{d\omega}$ and $\frac{d\mu'(\omega)}{d\omega}$ of the NRIM. It is this understanding that negative refraction takes a finite time to develop, which resolves most of the misunderstanding/controversies (see references therein [49]) about negative refraction. Secondly we can see that, the more negative ϵ', μ' is, the steeper the gradient of ϵ', μ' is as a function of ω. This implies that in/near the frequency region where ϵ', μ' are negative, there exist a resonant frequency ω_r where ϵ', μ' would diverge. Therefore from this heuristic argument, we see that one of the ways to create NRIM with $\epsilon', \mu' < 0$ would be to incorporate resonant structures in the material (see section 3.2). Finally the necessity of dispersion also implies the necessity for losses from Kramers-Kronig relation[12]. The important point to note however, is whilst this is true, it is still possible to construct NRIM with low losses. For instance if there are sufficient losses for some frequency bandwidth far away from the operating frequency, or if we have gain ($\epsilon'' > 0$) for some frequency bandwidth, we can still have NRIM with low losses without violating KK relations.

[11] Derivation from [3] pg 275. This was first derived by Brillouin in 1921.

[12] Kramers-Kronig relation imposes a constraint between the real and imaginary parts of ϵ, based on causality and analyticity of $\epsilon(\omega)$. Causality implies that $\epsilon(\omega)$ must be regular in the upper half complex plane. KK relation is therefore given by $\epsilon'(\omega) - 1 = \frac{2}{\pi}P\int_0^\infty \frac{x\epsilon''(x)}{x^2-\omega^2}dx$.

2.4 Criterion and terminology for negative refraction

We have thus far talked about properties of isotropic materials with simultaneously $\epsilon' < 0$, $\mu' < 0$ and referred to such materials as NRIM. However, are these properties of 'negative refraction', solely unique to media with $\epsilon' < 0$, $\mu' < 0$ or can we broaden the definition of what can be considered as a 'NRIM'? To address this question we need to be more precise with the *criterion* of what can be considered as a NRIM. Following this we shall list some common *terminology* to describe materials which demonstrate 'negative refraction' properties, and list some of the advantages/disadvantages associated with each. Firstly the criterion of a negative angle of refraction at an interface is not a sufficient criterion to imply NRIM, since there are materials which supports negative refraction at an interface but are not NRIM. For instance a uniaxial anisotropic PRIM cut at a certain angle can exhibit 'negative refraction' at an interface [50]. Similarly, photonic crystals which has shrinking iso-frequency contours near symmetry points can exhibit negative refraction as well [51] though they do not exhibit all the properties associated with NRIM.

A much broader and more precise criterion for NRIM is (as we have discussed previously) to consider materials which *supports backward waves*:

$$\Re\left[\mathbf{k}\right].\langle\mathbf{S}\rangle < 0 \tag{2.9}$$

Based on this criterion, there are some constraints/inequalities on the real and imaginary parts of ϵ, μ of a NRIM. For instance, using eq (2.9), and the *ansatz* of wave like solutions in the NRIM, Depine *et al* [52] showed that this criterion [13] implies the following constraint:

$$\Re(\epsilon)\,|\mu| + \Re(\mu)\,|\epsilon| < 0 \tag{2.10}$$

Now before going further, we should consider whether such a criterion of supporting backward waves, is a *necessary and sufficient* condition to imply NRIM. We have shown that a NRIM necessarily supports backward waves, but a material which supports backward waves is not necessarily a NRIM. For instance it can be shown that moving media supports backward waves in *some* directions [54] but it is not a NRIM. Moreover the support of backward waves does not imply that the material would inherit all the properties of a NRIM. For instance a photonic crystal material

[13] See [53] for an overview other citeria and their range of validity

can support backward waves, but does not enhance evanescent fields hence it does not display perfect lensing. Thus, in conclusion, while the support of backward waves is a good criterion it should be noted that it is only a *sufficient condition* for NRIM. Now having define the criterion for NRIM, the following are common terminology for NRIM. Historically the first name given by Vesalago (1968) is a *left handed material* (LHM). Such a nomenclature only makes sense when k, E, H forms a left handed triad, as such fails to include chiral/bianisotropic materials. A second very popular name which we have used thus far is the *negative refractive index material* (NRIM); referring directly to the property of negative refraction at an interface. As stated before, it is important to bear in mind that such a property is not unique to NRIM. In addition it loses meaning whatsoever when a negative refractive index cannot be defined. Despite its' shortcomings, we shall retain the use of this terminology for consistency and its' popularity. Another name proposed by Ziolkowski and Heyman (2001) [55], is the *double negative media*, referring to $\Re(\epsilon) < 0$, $\Re(\mu) < 0$. Again such a name is suitable only for non-bianisotropic material. Consistent with the property of backward waves, Lindell *et al* (2001) [56] proposed the name *backward wave media* (BW). Such a name can now include bianisotropic materials, though as mentioned before, the criterion of backward waves is only sufficient but not necessary to imply NRIM. Finally another name suggested by Pendry *et al* (2003) [23] is the *complementary media* (CM), which refers to one of the most important property of NRIM - to optically reverse/cancel the presence of another material - a property used to design perfect lenses. Such a nomenclature can encompass anisotropic (possibly bianisotropic) and even materials with indefinite signature [14].

In conclusion it should be noted that no perfect name exists which encompasses all or most of the characteristics and properties of 'NRIM' while remaining simple and evocative enough. The nomenclature should be used according to the circumstances, and with care about the assumptions and validity. In principle, the most suitable name to describe perfect lenses should be complementary media. Though we shall use CM and NRIM interchangeably in this thesis.

[14] 'Indefinite' signature means materials where the principal value of ϵ, μ has different signs. Such material may behave like a NRIM in some directions and a PRIM in others.

3. Homogenisation and metamaterials

3.1 Homogenisation

The philosophy of NRIM or indeed most metamaterial engineering begins from the principle of homogenisation (effective medium theory or mean field theory). The key idea homogenisation arises from coarse graining - a procedure where we can average out the field interactions of a complicated array of subsystems (atoms, molecules or metaparticles) and replace them with a single (simpler) effective subsystem. If such coarse graining is repeated enough, over the entire system, then we can regard the entire system as a effective homogeneous medium [57, 58] (fig 3.1).

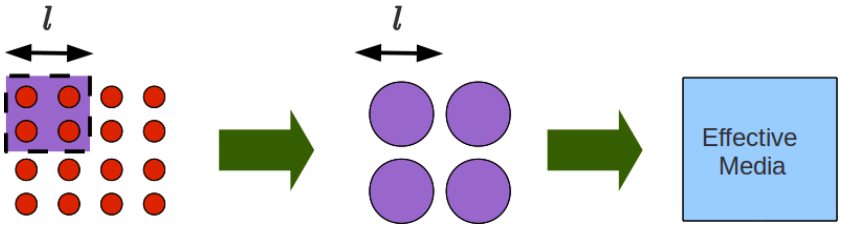


Figure 3.1: Illustration of the process of homogenisation. Each green arrow represents the process of coarse graining - spatially averaging out the finer details. The aim of the coarse graining process is to replace the complicated array of subsystems with a single homogenous effective medium.

In another words, metamaterials composed of inhomogenous structural units are indistinguishable from an *effective homogeneous medium* for fields (EM or acoustics) of *certain lengthscales*. The effective parameters that we can extract from such an effective medium are highly influenced by the type of sub-units (metaparticles) which we can engineer. This means that by meticulously designing the individual sub-units,

we can then create "homogenous" materials with bulk "designer" properties that we want. Now the validity of such coarse graining process to obtain an effective medium is dependent on the length scales of the fields and of the system. As such it is important to know the lengthscales involved, in order to be clear when homogenisation is valid (section 3.1.1). Subsequently we shall describe a systematic procedure by which one may extract effective parameters from the system (section 3.1.2).

3.1.1 Length and time scales

Before we consider the coarse graining process, it is important that we know what are the length scales involved, in order to be clear about our assumptions or range of validity. The description of a metamaterial as a homogeneous effective medium involves spatial averaging over fluctuations of the electromagnetic fields at two levels. First, the size of the metaparticles l, are considered to be large on a molecular/atomic length scale ($\zeta \sim 0.1nm$) so that we can average out the rapidly fluctuating microscopic currents and charge densities, and regard each metaparticle as a homogenous material without reference to its atomistic parts (see fig 3.2(a)). This 1^{st} level of averaging allows us to describe the response of individual metaparticle to EM fields using macroscopic Maxwell's equations, with averaged macroscopic fields and well defined macroscopic permittivities and permeabilities[1].

On a 2^{nd} level, when the wavelength of the EM fields λ is much larger than the (typical) periodicity a of the metaparticles ($\lambda \gtrsim 10 \times a$), the inhomogenity becomes invisible to the EM fields; we can then spatially average out the metaparticle array and consider the metamaterial as a homogenous medium with an effective permittivity and permeability $\boldsymbol{\epsilon}_{eff}$ and $\boldsymbol{\mu}_{eff}$ (fig 3.2(b)). When the assumption ($\lambda \gtrsim 10 \times a$) holds, we can simplify our homogenisation process by considering fields to be quasi-static and ignore retardation effects. Before proceeding to describe in detail, the method to extract these effective parameters, we need to be wary of the

[1] If $\mathbf{e}$ and $\mathbf{b}$ are the microscopic Electric and Magnetic fields that interact directly with electrons and nuclei, then we can define a macroscopic electric and magnetic fields by $\mathbf{E} = \langle \mathbf{e} \rangle$ and $\mathbf{B} = \langle \mathbf{b} \rangle$, where $\langle\rangle$ refers to the spatial averaging over a single or group of atoms/molecules. Similarly we can average out the rapidly fluctuating microscopic currents and charge densities and obtain well defined macroscopic $\boldsymbol{\epsilon}$, $\boldsymbol{\mu}$ and macroscopic free currents and charge densities $\mathbf{j}$ and ρ. (see [2] pg 226)

subtleties involved in the 1^{st} level of averaging.

If the metaparticle is composed of metals, we may describe the response of the metaparticle by a complex permittivity given by the Drude model[2] [2], where the response of the conduction electron to the E field is composed of 2 parts. The first is associated with inertia of the electron and the second with drag due to collisions. This can be written as $\left(m\omega^2 + i\gamma\omega\right)\langle\mathbf{x}\rangle = e\mathbf{E}$; where $\langle\mathbf{x}\rangle$ is the average position of the electron; m_e and e are the electron mass and charge; and $\gamma/m_e = \tau$ is the relaxation time (or mean free time between electronic collisions, typical $\tau \sim 10^{-14}s$ [59]). At low frequencies ($\omega\tau < 1$ or $\omega \lesssim 100THz$) the second term dominates and the electrons in the metal are regarded as being diffusive, thus we can consider the metal as being essentially ohmic. At high frequencies when ($\omega\tau > 1$ or $\omega \gtrsim 100THz$) then the first term dominates and the electrons are basically ballistic, thus the metal is no longer ohmic but inductive due to the finite mass of the electron. This inductance is known as the kinetic/inertial inductance. Other than this extra inductance, another related subtlety, is the additional *losses through finite size effects* for very small metaparticles. When the size of a metaparticle l, is smaller than the mean free path of the electrons ξ (where $l \lesssim \xi \sim (\tau v_F) \sim 10nm$, and $v_F \sim 10^6 ms^{-1}$ is the Fermi velocity, see fig 3.2(a)), even though the electrons are essentially non-collisional in the bulk, the electrons collides with the boundaries of the metaparticle, hence the relaxation time decreases with size ($\tau \sim l/v_F$). This extra loss modifies the Drude model, increasing the damping parameter $\gamma = m_e\tau \sim m_e l/v_F$.

Thus extra care should be taken, to use the correct Drude model, when designing very small metaparticles. These effects are important as we shall discover the properties of the metamaterials depends not only on the geometry but also the size of the metaparticle (see section 3.2.2). If we keep the geometry but scale the size down we can increase the operational frequency of the metamaterial as long as the metals within the metamaterial are considered ohmic. This scaling breaks down when inertial inductance dominates and in turn imposes an upper limit to high (optical) frequency metamaterials [60–63]. The extra losses due to finite size effects also impose another limit, as losses broaden and destroy the resonances crucial for design

[2]The permittivity of a metal particle (disregarding inter and intraband transitions) can be described by the Drude model as $\epsilon = \epsilon_\infty - \frac{\omega_p^2}{\omega^2 - i\gamma\omega}$; where ω_p is the plasma frequency, γ is the damping factor associated with electron collisions.

of NRIM.

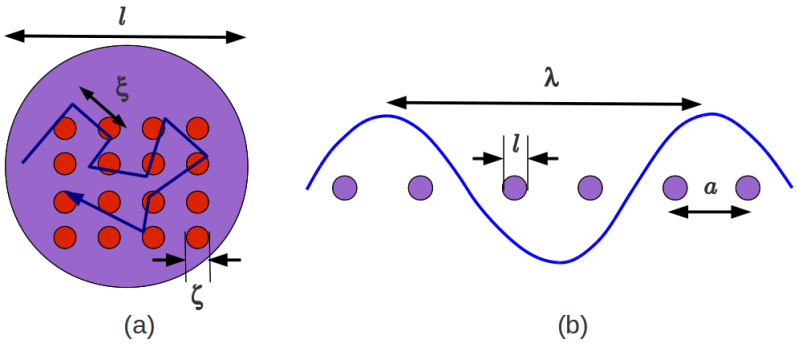


Figure 3.2: Length scales to consider for homogenisation. Fig (a) illustration of the 1^{st} level of homogenisation. The expanded view of the individual metaparticle of size l, composed of atomistic (red spheres) parts of size ζ and electrons (blue line) with mean free path ξ. The 1^{st} level of averaging regards each metaparticle as homogenous described by a macroscopic ϵ, μ. Fig (b) illustration of the 2^{nd} level of homogenisation. Fields with wavelength λ, impinging on a metamaterial with periodicity a, composed of meta particles (magenta spheres) with typical size l, would regard the array as homogeneous with effective $\boldsymbol{\epsilon}_{eff}$, $\boldsymbol{\mu}_{eff}$.

3.1.2 Effective medium parameters

The prescription for an analytical retrieval of effective parameters from this 2^{nd} homogenisation is simple and follows from [7]. The effective permittivity and permeability of the metamaterial can be described by the spatially averaged electromagnetic fields:

$$< \mathbf{D} >= \boldsymbol{\epsilon}_{eff}. < \mathbf{E} >, \qquad < \mathbf{B} >= \boldsymbol{\mu}_{eff}. < \mathbf{H} > \tag{3.1}$$

With these parameters, we can then describe the electromagnetic interactions of a structurally inhomogenous metamaterial with an equivalent homogenous effective medium. For wavelengths $\lambda \gtrsim 10 \times a$, we may assume and employ the simplification of quasi-static approximation[3] in the coarse graining calculation. To calculate the

[3]The quasi-static approximation implies the fields in a unit cell of the metamaterial satisfies the simpler Laplace's equation $\nabla^2\psi = 0$ which can be easily solved to obtain the field distribution in a unit cell.

averaged fields we begin from the integral form of Maxwell's equation:

$$\oint_C \mathbf{H}.d\mathbf{l} = -\oint_S \dot{\mathbf{D}}.d\sigma \tag{3.2}$$

$$\oint_C \mathbf{E}.d\mathbf{l} = -\oint_S \dot{\mathbf{B}}.d\sigma \tag{3.3}$$

where the curve C encloses the surface S. This integral form suggests an averaging procedure since E, H fields are defined along "lines" and B, D fields are defined over "areas"[4]. Now suppose we can divide our material into a periodic lattice, composed of two interlocking *simple cubic unit cell* (see fig 3.3). One of the unit cell will be the lattice of E-fields while the other will be the lattice of H-fields. The averaged electric field, $\langle \mathbf{E} \rangle = \mathbf{E}_{eff}$ is then defined along the edges of one of the unit cell by averaging $\mathbf{E}$ along the edge of that unit cell, while the averaged magnetic field, $\langle \mathbf{H} \rangle = \mathbf{H}_{eff}$, is defined by the average of $\mathbf{H}$ on the other.

$$E_{eff}^{(x)} = \frac{1}{a}\int_{(0,0,0)}^{(a,0,0)} E_x dx,\ E_{eff}^{(y)} = \frac{1}{a}\int_{(0,0,0)}^{(0,a,0)} E_y dy,\ E_{eff}^{(z)} = \frac{1}{a}\int_{(0,0,0)}^{(0,0,a)} E_z dz \tag{3.4}$$

$$H_{eff}^{(x)} = \frac{1}{a}\int_{(0,\frac{a}{2},\frac{a}{2})}^{(a,\frac{a}{2},\frac{a}{2})} H_x dx,\ H_{eff}^{(y)} = \frac{1}{a}\int_{(\frac{a}{2},0,\frac{a}{2})}^{(\frac{a}{2},a,\frac{a}{2})} H_y dy,\ H_{eff}^{(z)} = \frac{1}{a}\int_{(\frac{a}{2},\frac{a}{2},0)}^{(\frac{a}{2},\frac{a}{2},a)} H_z dz \tag{3.5}$$

Similarly, the effective displacement field, $\langle \mathbf{D} \rangle = \mathbf{D}_{eff}$, can be defined by averaging $\mathbf{D}$ field over the faces of the E-field unit cell while the effective magnetic flux density, $\langle \mathbf{B} \rangle = \mathbf{B}_{eff}$ can be defined by the average of the $\mathbf{B}$ field over the faces of the other H-field unit cell:

$$D_{eff}^{(x)} = \frac{1}{a^2}\int_{S_x} D_x d\sigma_x,\ D_{eff}^{(y)} = \frac{1}{a^2}\int_{S_y} D_y d\sigma_y,\ D_{eff}^{(z)} = \frac{1}{a^2}\int_{S_z} D_z d\sigma_z \tag{3.6}$$

$$B_{eff}^{(x)} = \frac{1}{a^2}\int_{S_x} B_x d\sigma_x,\ B_{eff}^{(y)} = \frac{1}{a^2}\int_{S_y} B_y d\sigma_y,\ B_{eff}^{(z)} = \frac{1}{a^2}\int_{S_z} B_z d\sigma_z \tag{3.7}$$

where $S_{x,y,z}$ refers to directed areas of the unit cell. The directions of $\mathbf{D}_{eff}$ and $\mathbf{B}_{eff}$, lie in the normal of the surfaces.

With the averaged fields we can then make use of eqn (3.1) to determine the effective permittivity and permeability, $\boldsymbol{\epsilon}_{eff}$, $\boldsymbol{\mu}_{eff}$, component-wise. This procedure is unique and independent of the choice and position of unit cells. The only restriction is that such unit cell boundaries must not intersect with any of microstructures contained within, to ensure the continuity of the parallel components of $\mathbf{E}_{eff}$ and $\mathbf{H}_{eff}$ across the boundaries.

[4] In differential geometry E, H are 1 forms (oriented lines) and D, B are 2 forms (oriented areas) [64, 65]

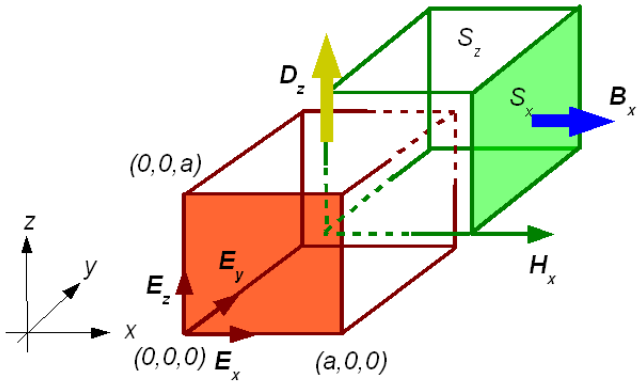


Figure 3.3: Pendry's averaging procedure. Figure shows two interlocking simple cubic lattice. The edges of the red lattice are the E vectors while the edges of the green lattice are the H vectors. The B field (the blue arrow, B_x) is the normal to the H lattice surface, (the shaded green surface, S_x). The E, H vectors are averaged over the lines along the edges, while the B, D vectors are averaged over the surfaces.

3.2 Metaparticles

So far we have demonstrated how we can obtain effective parameters for metamaterials via the coarse graining scheme described in the previous section. These effective parameters are highly dependent on the structure and arrangement of the metaparticles, which we can engineer. Thus the beauty of metamaterial engineering is it presents a systematic 'forward' approach to designer materials - that is given a requisite application, we can now *engineer a material* to fit the bill. While this approach to material engineering is general, in the following discussion we shall only focus on metaparticles which gives negative ϵ, μ. Now, it is neither possible nor illuminating, given the present space, to present an exhaustive list of metaparticles available in literature. As such in this section, we shall only present two archetypal metaparticles and show how to obtain explicitly the effective parameters of metamaterials derived from them. As mentioned previously (section 2.3), the necessity for dispersion in NRIM indicates the necessity for resonance. Another way of seeing this is the following. If the displacement field $\mathbf{D}$, is the material response to an electric field $\mathbf{E}$, then $\epsilon(\omega)$ is the linear response function detailing this response - in much the same way as the mass of a body is the linear response function detailing how a

body accelerates under a force. Understood in these terms then for some ω, where $\epsilon'(\omega) < 0$, would indicate that $\mathbf{D}(\omega)$ (the response) is anti-phase to $\mathbf{E}(\omega)$ (the force). Such an anti-phase response is a signature of resonant linear systems driven at frequencies ω, beyond some resonant frequency, ω_r (post-resonance; $\omega > \omega_r$). Thus this post-resonant approach is one of the ways by which we can engineer $\epsilon' \leq 0$, $\mu' \leq 0$ metamaterials.

3.2.1 Electric metaparticles ($\epsilon < 0$)

As briefly seen, to have a negative permittivity, we need to have post-resonant metaparticles with electric response. In fact such a resonant behavior is found naturally in plasmonic systems (metals or a gaseous plasma), where free electrons oscillate collectively in the presence of an E field, against a background of positive ions. For photon energies well below inter and intra-band transitions we can describe permittivity of plasmonic systems using the simple Drude model [2]:

$$\epsilon = \epsilon_\infty - \frac{\omega_p^2}{\omega^2 + i\gamma\omega} \tag{3.8}$$

where ϵ_∞ (typically $1 \leq \epsilon_\infty \lesssim 10$) is due to the residual polarisation of the background, γ is the damping factor associated with free electron collision, and ω_p is the plasma frequency given by:

$$\omega_p^2 = \frac{n_e e^2}{\epsilon_0 m} \tag{3.9}$$

where n_e is the free electron density, e and m are the electronic charge and mass respectively. At higher photon energies (for noble metals $\geq$ 1eV), when interband transitions are taken into account, the Drude model is modified to the Lorentz model given by [2]:

$$\epsilon = \epsilon_\infty - \omega_p^2 \sum_j \frac{f_j}{\omega^2 - \omega_j^2 + i\gamma_j\omega} \tag{3.10}$$

where f_j is the oscillator strength, a measure of the transition rates between bands of energy $\hbar\omega_j$. For the Drude model, the resonant frequency of the system is $\omega_r = 0$, while for the Lorentz model $\omega_r = \omega_j$, and we can easily see for both models that $\epsilon(\omega) < 0$ for some $\omega_p > \omega > \omega_j$ [5].

[5] More precisely $\omega \gtrsim \sqrt{\omega_j^2 - \omega_p^2/\epsilon_\infty}$

All this is nice and well except short of changing the chemical composition of the plasmonic system, we can't really do much to modify the range of ω which displays negative permittivity. For the Drude model that amounts to changing plasma frequency ω_p and this is precisely what Pendry *et al* [5] did when they introduced the wire mesh structure (fig 3.4). The idea was simple - by confining electrons in a

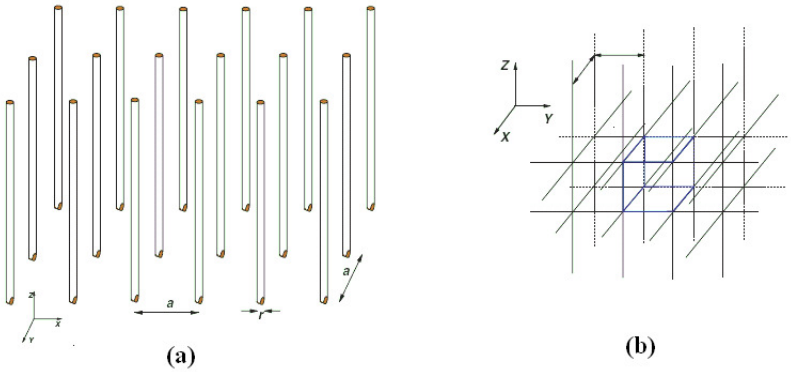


Figure 3.4: Fig (a) a wire mesh array of thin metal wires with radius r and a lattice period of a embedded in a dielectric, behaves as a low frequency plasma for the E field oriented along the wires. Fig (b) a 3-dimensional lattice behaves like an isotropic low frequency plasma.

dilute array of conducting wires and changing the size and periodicity of these wires, one can change the effective electron density and mass of electrons, hence tune the plasma frequency ω_p (see eqn 3.9). Consider an array of infinitely long, parallel and thin metal wires of radius r, with periodicity a where $a \gg r$ (see fig 3.4(a)). The electric field is considered to be applied parallel to the wires (along the z axis) and we assume that the wavelength of the applied field $\lambda \gg a \gg r$. In this arrangement, the electrons are confined to move only within the wires which has, first the effect of diluting the effective electron density as the E-field cannot probe the individual wire structure but only the average charge density. The effective electron density then becomes

$$n_{eff} = \frac{\pi r^2}{a^2} n_e \tag{3.11}$$

Secondly the thin wires also have the effect of 'modifying' the electronic mass. The electrons moving in the wires generate a magnetic field, and this in turn creates a self-inductance which resist the electronic motion, effectively increasing the "mass"

of the electrons. This effective mass is given by [5]:

$$m_{eff} = \frac{\mu_0 r^2 n_e e^2}{2} \ln\left(\frac{a}{r}\right) \tag{3.12}$$

Using Eqn (3.11,3.12) in Eqn (3.9), we can then work out the new effective plasma frequency:

$$\omega_p^2 = \frac{n_{eff} e^2}{\epsilon_0 m_{eff}} = \frac{2\pi c^2}{a^2 \ln(a/r)} \tag{3.13}$$

The combined effect of reducing the electron density and increasing the electronic mass implies that the wire mesh structure has a much lower plasma frequency than a solid block of metal. For instance using aluminium wires ($n_e = 10^{29} m^{-3}$) with $r = 1\mu m$, $a = 10mm$, gives us a plasma frequency of about $2GHz$ which is 10^9 times smaller than the plasma frequency of aluminium itself, thus allowing us to create a negative dielectric material at microwave frequencies.

Note that the effective plasma frequency obtained in eqn (3.13) is independent of the microscopic properties such as electron density and drift velocity of the wires used. It only depends on the radius and periodicity of the wires indicating that the entire problem could be recast in terms of capacitances and inductances [66, 67]. Using this approach (see appendix A.1), we can also account for finite conductivity σ, in the wires and show that the effective permitivity ϵ_{eff}, of the mesh structure would obey essentially the same Drude model (eqn (3.8)), except with plasma frequency given by eqn (3.13) and damping factor given by $\gamma = (\epsilon_0 a^2 \omega_p^2 / \pi r^2 \sigma)$. We can see that the better the conductivity of the wires, the smaller the damping so for aluminium ($\sigma = 3.65 \times 10^7 \Omega^{-1} \mathrm{m}^{-1}$), that yields values of $\gamma = 0.1\omega_p$ which is not very large. This means that the low (microwave) frequency plasmons are sufficiently stable against losses for a negative effective permittivity, ϵ_{eff} to be observable.

3.2.2 Magnetic metaparticles ($\mu < 0$)

3.2.2.1 Why are magnetic metaparticles necessary?

Again, by adopting the same general principle of using post-resonant metaparticles, we can create negative μ metamaterials. Before we outline how this can be done it is important to note the following. Unlike the electric response, the magnetic response of most natural materials are very weak, hence magnetic permeability of

most (non-ferromagnetic) materials $\mu \sim 1$. For instance typical values[6] of diamagnetic suscetibilities are $\sim 10^{-5}$ and paramagnetic suscetibilities are $\sim 10^{-2}$ to 10^{-3}. This difference arises mainly because the magnetisation of a (non-ferromagnetic) body is a relativistic effect, of order v^2/c^2, where v is the velocity of the electrons in the atoms[7]. Moreover Landau [3] argues that effects of dispersion for the magnetic permeability at low frequencies (up to optical frequencies) of most natural materials are negligible[8] hence $\mu(\omega) \sim 1$.

All this implies that unlike permittivity, the only route to negative permeability (or more generally materials with significant magnetic susceptibility) is through metamaterials. While Landau's argument for weak magnetic response holds true for most natural materials, Merlin [68] showed that this argument breaks down for composites made of substances with large permittivity[9] (metals or high permittivity dielectrics).

The necessity for metallic inclusions [7] or high permittivity dielectrics [69][10] was thus an essential route to design of most magnetic metamaterials. It is the former that we shall focus on in this section.

---

[6]Typical Magnetic Susceptibilities estimates based on quantum mechanical calculations, [59] Pg 656

[7]The ratio v/c appears with $\mathbf{H}$ vector in the Hamiltonian of the interaction of the body with the magnetic field, and another factor of v/c in the magnetic moments of the atoms or molecules ([3] page 106).

[8]Essentially Landau ([3] Pg 268) argues that the physical meaning of the Magnetisation $\mathbf{M}$, as being the magnetic moment per unit volume, requires that the magnetization-induced current be significantly larger than that due to the time-varying (induced electric) polarization ($|\nabla \times M| \gg |\partial_t \mathbf{P}|$). For diamagnets at optical frequency, Landau showed that $|\nabla \times M| / |\partial_t \mathbf{P}| \sim (\zeta/l)^2$ where ζ is the atomic dimension and l is the size of the body. Since the macroscopic size of the body is larger than its atomic dimension ($l \gg \zeta$) this implies $|\nabla \times M| \ll |\partial_t \mathbf{P}|$ instead - thus we can essentially ignore $\mathbf{M}$ and set $\mu(\omega) \sim 1$.

[9]Merlin [68] showed through general physical arguments, that Landau's argument for $\mu(\omega) \sim 1$ breaks down for composites made of substances with $\Im(\sqrt{\epsilon_s}) \gg \lambda/l$ or $\Re(\sqrt{\epsilon_s}) \sim \lambda/l$ (ϵ_s and l are the complex permittivity and the characteristic length of the particles, and $\lambda \gg l$ is the vacuum wavelength)

[10]Although magnetic activity via Mie scattering resonances [70] in systems of small scattering particles has been realised as early as 1986 [71], it was only in 2002 that O'Brien *et al* proposed and demonstrated the use of these magnetic Mie scattering resonances as an alternative route to negative μ materials.

3.2.2.2 Split-ring resonators

As we have seen before, to create a negative μ metamaterial we need to incorporate post-resonant magnetic metaparticles. And one of the most straightforward recipe to make such metaparticles, is to construct a resonant L-C circuit which has a natural resonant frequency ω_r less than the frequency ω of the driving H field. The inductive element of the metaparticle will capture the H field, and the induced current behaves like a 'mass', while the capacitative element stores charges and behaves like a 'spring'. Together, the L-C elements in the metaparticle, in the presence of an applied H field, will thus behave like a driven simple harmonic oscillator with a resonant frequency, $\omega_r \sim \frac{1}{\sqrt{LC}}$. Hence by tuning the capacitances and inductances of the metaparticle we can design the required metamaterial. Such was the strategy adopted by Pendry

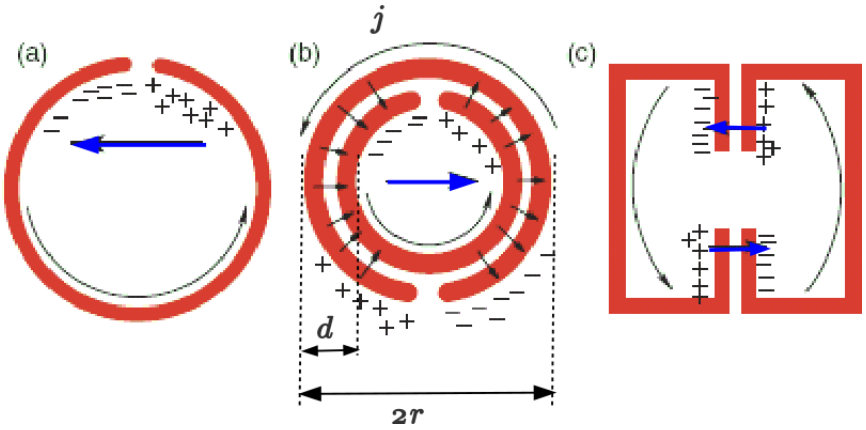


Figure 3.5: Cross sectional view of split-ring resonators (SRR). Fig (a) a single-split SRR. Fig (b) SRR structure used by Pendry in 1999 [7] to demonstrate the first negative μ metamaterial. Fig (c) a double-split SRR. The applied time-varying H field, perpendicular to the SRR, would induce a current j around the rings, which is interrupted by the split. The charges accumulated at the split result in an induced electric dipole moment (blue arrow).

[7] when he proposed the split-ring resonator (SRR) (see fig 3.5 (b)) as a design for such metaparticle. Consider a periodic array (periodicity a, see fig 3.4(a)) of cylinders (radius r) with such a cross-sectional profile. When a time-varying H field, is applied perpendicular to the SRRs (along the axial direction of the cylinders), it would induce a current j around the rings. The large gap in each ring prevents the current, j from forming a closed loop and acts as the capacitative element. As

before we can extract the effective parameters of such a metamaterial using the method outline in section 3.1.2. Using the quasi-static approximation and Maxwell's equations (Faraday's law) we can calculate j , and determine the local H field in each unit cell. With this local H field we can determine H_{eff} using eqn (3.5) and B_{eff} using eqn (3.7). With these effective fields we can then determine the effective permeability (see appendix A.2) using eqn (3.1):

$$\mu_{eff} = \frac{B_{eff}}{\mu_0 H_{eff}} = 1 + \frac{f\omega^2}{\omega_r^2 - \omega^2 - \mathrm{i}\Gamma\omega} \tag{3.14}$$

which has a Lorentz type dispersion. Here $f = \pi r^2/a^2$ is the filling fraction of the cylinder compared to the host medium, $\Gamma = (2\rho/\mu_0 r)$ is the damping parameter and:

$$\omega_r = \left(\frac{3d}{\mu_0\epsilon_0\epsilon\pi^2 r^3}\right)^{1/2} \tag{3.15}$$

is the resonant frequency. In addition if we define

$$\omega_m = \left(\frac{3d}{(1-f)\mu_0\epsilon_0\epsilon\pi^2 r^3)}\right)^{1/2} \tag{3.16}$$

as the 'magnetic plasma' frequency, we easily see from eqn (3.14) that for frequency $\omega_r < \omega < \omega_m$, we would obtain a $\mu_{eff} < 0$ effective medium as required.

3.2.2.3 Scaling to higher frequencies and limitations

The characteristics of SRR metamaterial is prototypical of most magnetic metamaterial based on L-C resonances. First we note that as before, both the resonant (ω_r) and plasma frequency (ω_m), depend only on the geometric properties of the SRR. Hence by appropriate geometric design we can tune the operational frequency of the SRR. For instance we can easily see that by scaling down the size of the SRR we can increase the resonant frequency, and this turns out to be generic of magnetic metamaterial. Similarly, for a general magnetic metamaterial based on L-C resonances, we can similarly alter its characteristics by careful design of its inductances and capacitances, which depends strongly on the shape and size of the metaparticle. Since the resonant frequency $\omega_r \simeq 1/\sqrt{LC}$; by reducing L and C one can in principle raise the resonant frequency, hence operating frequency of the metamaterial.

Firstly to reduce the inductance we can do so by reducing the area of the inductive loop. Typically, for a metaparticle with a characteristic size l, this geometrical

inductance is given by $L_g \sim l^2$. Similarly since capacitance is given by $C \sim A_c/d_c$, where A_c is the area and d_c is the gap of the capacitance, thus capacitance of the metaparticle scales as $C \sim l$. Together then, the resonant frequency typically scales as $\omega_r \sim l^{-3/2}$, which implies that as the metaparticle scales down in size we should expect the resonant frequency to increase reciprocally. This scaling relation broadly holds true for lower frequencies ($\omega_r \lesssim 100THz$), as long as the metals in the metaparticle behave ohmically [61, 63]. As discussed in section 3.1.1, when $\omega_r \gtrsim 100THz$, electrons in metals behave ballistically, therefore there is an additional kinetic inductance to account for, which even dominates over the geometrical inductance. Since this kinetic inductance is given by[11] $L_i = V/\dot{I} \propto l/A$ (where A is the cross-sectional area of the conductor), thus at high frequencies inductance scales as $L_i \sim 1/l$ instead; which implies that $\omega_r \sim$ const. Thus the magnetic response of magnetic metaparticles saturates at optical frequencies due to the plasmonic nature of metals, presenting a natural upper limit to high frequency metamaterials [60–63].

One may think that we can overcome this limit due to kinetic inductance, by reducing capacitances instead. A systematic approach to reduce capacitances while not altering the geometry, is by adding capacitances in series. For instance a metaparticle of a single ring with a single gap has twice the capacitance compared to one with two symmetric gaps. Hence by increasing the number of gaps one can reduce the capacitances hence increase ω_r. Indeed this was the approach taken, when O'Brien *et al* showed numerically that a medium of SRR with two split can have a negative μ up to the infrared region ($\sim$ 60THz) [60] while a SRR with four splits can go up to telecommunications frequency ($\sim$ 200THz) [72]. However even with such an approach, there is still another fundamental limitation preventing the scaling of optical frequency metamaterial - that is the additional losses through finite size effects (see section 3.1.1). This extra loss results in an increase in the damping parameter Γ, in the dispersion of $\mu_{eff}(\omega)$ (see eqn (3.14)) and the net effect is the broadening or even destruction of the resonance of $\mu_{eff}(\omega)$. Thus even if we can bypass the limit imposed by kinetic inductance, by adding more slits in the SRR, the effect of dividing

[11] At frequencies above the relaxation rate, electrons are ballistic, hence the dynamics of the electron is given by $m_e\dot{v} = eE$. Since currents in conductors are given by $I = en_eAv$, and Electric field is related to the potential drop by $E = V/l$. We can show that the "kinetic" inductance due to the inertia of the electrons is given by $L_i = V/\dot{I} = m_el/n_eAe^2$

the SRR would reduce the size of the metals in the metaparticle, until the losses from finite size effects overwhelm and destroy the resonance which we are seeking in the first place. All in all it has been shown both qualitatively and quantitatively that the presence of both kinetic inductance and losses from finite size effects, imposes an upper frequency limit ($\sim 100 - 1000THz$) on optical magnetic metamaterial.

3.2.2.4 Magneto-electric coupling

As we can see, the crucial components of a magnetic metaparticle, are the inductive and capacitative elements. The presence of capacitances indicates charge separation within the metaparticle, and such charge separation implies an applied magnetic field can induce an electric dipole. Such a magneto-electric coupling in a metamaterial is known as bianisotropy[12]. Sometimes such magneto-electric coupling can be useful, for instance it was demonstrated that bianisotropic metamaterials can exhibit extremely strong optical activity [74], and the combination of bianisotropy and magnetic resonance can be used to create singly resonant NRIM [75]. However sometimes for certain applications, such as perfect lensing, one would like to avoid bianisotropy, hence it would be preferable if there was some way to "manage" the degree of bianisotropy. The way to do this, is through meticulous design of the metaparticle. If bianisotropy is desired then one should design the metaparticle with a large induced electric dipole moment. Conversely if bianisotropy is to be avoided then the net dipole moments in the metaparticle should cancel each other. Take the example of the SRR. It can be easily seen that a single-split SRR (fig 3.5 (a)) has a net electric dipole moment hence it ought to have a magneto-electric coupling. Conversely a symmetric double-split SRR (fig 3.5 (c)) has counterposing dipole moments hence no net magneto-electric coupling. The design of the metaparticle is only the first step in bianisotropy engineering. The net degree of bianisotropy in a metamaterial is also dependent on the arrangement and orientation of these metaparticles. For instance, even if individual magnetic metaparticles have a strong induced electric dipole moment, these dipole moments could be canceled out collectively by their

[12] A bianisotropic material obeys the following following constutive relations: $\mathbf{D} = \boldsymbol{\epsilon}.\mathbf{E} + \boldsymbol{\xi}.\mathbf{H}$ and $\mathbf{B} = \boldsymbol{\mu}.\mathbf{H} + \boldsymbol{\zeta}.\mathbf{E}$, where $\boldsymbol{\xi}$ and $\boldsymbol{\zeta}$ are magneto-electric coupling tensors. If $\boldsymbol{\epsilon} = \boldsymbol{\epsilon}^{*\top}$, $\boldsymbol{\mu} = \boldsymbol{\mu}^{*\top}$ and $\boldsymbol{\xi} = \boldsymbol{\zeta}^{*\top}$ the bianisotropic material is lossless. In addition if $\boldsymbol{\xi} = -\boldsymbol{\zeta}^{\top}$ then the bianisotropic material is reciprocal, further if $\Im(\boldsymbol{\xi}) = -\Im(\boldsymbol{\zeta}^{\top}) \neq 0$ then the material is optically active [73].

neighbors in a unit cell. This design of metamaterials with or without bianisotropy can be made systematic through group theoretical considerations [76] (see appendix A.3).

3.2.3 Negative refractive index materials

So far we have seen how to construct and "tune" metamaterials with $Re(\epsilon) < 0$ (section 3.2.1) and $Re(\mu) < 0$ (section 3.2.2), which involves arrays of post-resonant metaparticles. Now to go one step further, to construct a NRIM, we would need a medium with both $Re(\epsilon) < 0$ and $Re(\mu) < 0$ simultaneously. Intuitively one might guess how this could be done. If we combine negative ϵ metaparticles with negative μ metaparticles within the *same unit cell*, in such a way that, the resultant unit cell is much less than the variation of the applied fields ($a \ll \lambda$), then effective medium theory (section 3.1) tells us that such an inhomogeneous media can be treated as an effective homogenous NRIM. This was the approach adopted by Smith *et. al.* [8], who proposed combining the wire-mesh media ($\epsilon < 0$), with the SRR medium ($\mu < 0$) to obtain a NRIM (see fig 3.6). This procedure can be done so long as the band gap

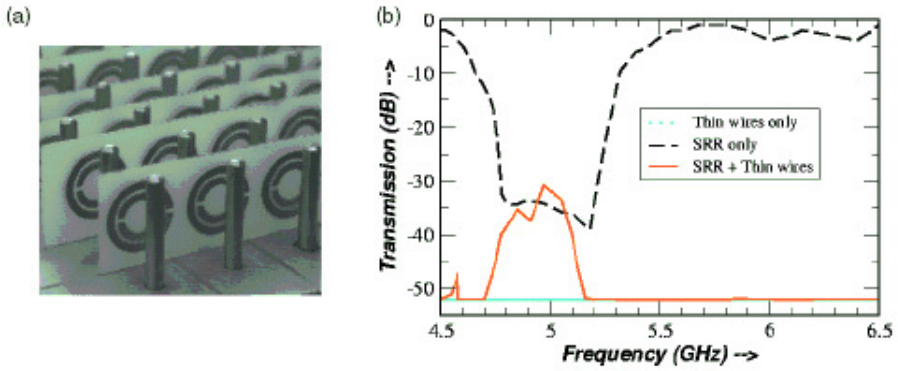


Figure 3.6: Fig (a) the SRR wire mesh array which displays negative refractive index. Fig (b) shows the transmission across a sample of thin wire arrays ($\cdots$), SRRs (- - -) and a composite of thin wire arrays and SRR(_ _ _) as measured by the San Diego group [9]. The enhanced transmission in the latter case within the negative μ band is interpreted as evidence of a negative refractive index.

of the negative ϵ medium overlaps with the band gap of the negative μ medium.

Combining the dispersions for a Drude-like $\epsilon(\omega)$ (eqn (A.4)) and a Lorentz-like $\mu(\omega)$ (eqn A.8) , we get the overall dispersion relation of the NRIM as:

$$k^2 = \frac{\epsilon\mu\omega^2}{c^2} = \frac{(\omega^2 - \omega_p^2)(\omega^2 - \omega_m^2)}{c^2(\omega^2 - \omega_r^2)} \tag{3.17}$$

where ω_p and ω_m are the electric and magnetic plasma frequencies, respectively, and ω_r is the magnetic resonance frequency ($\omega_m = \omega_r/\sqrt{(1-f)}$). If ω_p is the largest of them, then we obtain a pass-band in the region $\omega_r < \omega < \omega_m$ where we would have negative refractive index behavior. Other than the wire-mesh+SRR structure for NRIM proposed by Smith *et al,* there are many other alternative structures largely based on similar principles of combining a $\epsilon < 0$ system with a $\mu < 0$ one. For instance the fish-net structures [13, 77], and nano rod pairs [14]. If NRIM is defined by its support of backward waves (eqn (2.9)) then Pendry has also shown that a single dipole resonance in a bianisotropic chiral medium, such as a chiral swiss roll structure, can also display negative refractive index for one polarisation, albeit up to a finite wavevector [75].

4. Perfect lens theorem and transformation optics

4.1 Perfect lens theorem

As we have seen (section 2.2.2), a flat slab of $\epsilon = \mu = -1$ material behaves as a perfect lens. The action of perfect lensing on electromagnetic fields can be recasted as *complementarity* of medium - where a $\epsilon = \mu = -1$ slab behaves as an optical complementary to a $\epsilon = \mu = 1$ slab of vacuum, such that the effects of light propagating in vacuum can be optically reversed/canceled by its complementary. The net effect of this reversal becomes as if both slabs of material do not exist and the optical information from the object plane is then *translocated* to the image plane, and this is regarded as imaging. Since this optical reversal is effective for both propagating and evanescent near fields, the image quality obtained is far better than that of conventional lens and the combined action of *optical reversal* followed by *translocation* is what we call *perfect lensing*. This concept of complementarity can be further generalised to include a general *spatially inhomogenous*, *anisotropic*, but *flat*, slab of material. And pairs of such medium, which optically reverses/cancels the presence of each other are referred to as *complementary medium* (CM). The method prescribing the constitutive parameters of CM, is known as the *perfect lens theorem* (PLT), and will be the focus in this section.

4.1.1 Statement of theorem

The perfect lens theorem (PLT) [23] can be stated as follows:

Given a slab of material $(-d < z < 0)$ *with constitutive parameters* $\boldsymbol{\epsilon(x), \mu(x)}$*; then a second slab* $(0 < z < d)$ *with* $\tilde{\boldsymbol{\epsilon}}(\bar{\boldsymbol{x}}) = -\bar{\boldsymbol{\epsilon}}(\bar{\boldsymbol{x}}), \tilde{\boldsymbol{\mu}}(\bar{\boldsymbol{x}}) = -\bar{\boldsymbol{\mu}}(\bar{\boldsymbol{x}})$,

which is a mirror copy of the first with all eigenvalues reversed in sign, would be an optical complementary to the first (where all 'barred' quantities are reflections of the 'un-barred' ones; that is $\bar{\boldsymbol{x}} = \mathbf{R}\boldsymbol{x}$, $\bar{\boldsymbol{\epsilon}} = \mathbf{R}\boldsymbol{\epsilon}\mathbf{R}^{-1}$ etc, with $\mathbf{R} = \mathrm{Diag}\,[1, 1, -1]$ being the reflection operator about $z = 0$).

The consequence of the PLT is that:

The net optical effect of propagation through both complementary slabs would "cancel out", so that electromagnetic field information at the object plane ($z = -d$) appears to be "translocated" to the image plane ($z = d$).

4.1.2 Proof of theorem

In essence the perfect lens theorem (PLT) is a consequence of the reflection symmetry [2] in Maxwell's equations. Firstly the time-harmonic Maxwell's equations in the *absence of free charges and currents* are given by

$$\begin{aligned} \nabla \times E &= -i\omega B \qquad \nabla.D = 0 \\ \nabla \times H &= i\omega D \qquad \nabla.B = 0 \end{aligned} \tag{4.1}$$

We can clearly see that under spatial reflections (about $z = 0$ plane), $\{E, H\}$ transform as vectors whilst $\{D, B\}$ transform as pseudo-vectors - that is under reflection $\Re : \{\mathbf{E}_\perp, E_z\} \to \{\mathbf{E}_\perp, -E_z\}$, while $\Re : \{\mathbf{D}_\perp, D_z\} \to \{-\mathbf{D}_\perp, D_z\}$ [1]. From the constitutive equation (assuming linearity)

$$\begin{aligned} D &= \boldsymbol{\epsilon}.E \\ B &= \boldsymbol{\mu}.H \end{aligned} \tag{4.2}$$

we can therefore see that in order to map the vectors on the right side of the equation to pseudo-vectors on the left, the permitivity (permeability) tensor must transform under reflection as $\Re : \boldsymbol{\epsilon} \to \tilde{\boldsymbol{\epsilon}}$

$$\boldsymbol{\epsilon} = \begin{pmatrix} \epsilon_{xx} & \epsilon_{xy} & \epsilon_{xz} \\ \epsilon_{yx} & \epsilon_{yy} & \epsilon_{yz} \\ \epsilon_{zx} & \epsilon_{zy} & \epsilon_{zz} \end{pmatrix} \quad \tilde{\boldsymbol{\epsilon}} = \begin{pmatrix} -\epsilon_{xx} & -\epsilon_{xy} & \epsilon_{xz} \\ -\epsilon_{yx} & -\epsilon_{yy} & \epsilon_{yz} \\ \epsilon_{zx} & \epsilon_{zy} & -\epsilon_{zz} \end{pmatrix} \tag{4.3}$$

[1] This can be proven readily for Cartesian coordinates. Since from Maxwell's curl equations, expressed in Cartesian coordinates (and setting $i\omega = 1$), we have $D_i = \varepsilon_{ijk}\partial_j H_k$, and from linear algebra $\varepsilon_{\bar{i}\bar{j}\bar{k}} R_{i\bar{i}} R_{j\bar{j}} R_{k\bar{k}} = \varepsilon_{ijk} \det(\mathbf{R})$, this implies that under reflection ($\bar{x}_{\bar{i}} = R_{i\bar{i}} x_i$ where $\mathbf{R}$ is the reflection operator, and $\mathbf{x}$ and $\bar{\mathbf{x}}$ are the vector and its reflected copy) $\bar{D}_{\bar{i}} = \varepsilon_{\bar{i}\bar{j}\bar{k}}\partial_{\bar{j}}\bar{H}_{\bar{k}} = \det(\mathbf{R}) R_{i\bar{i}}\varepsilon_{ijk}\partial_j H_k = \det(\mathbf{R}) R_{i\bar{i}} D_i$. Since $\det(\mathbf{R}) = -1$, therefore $\mathbf{D}$ transforms as a pseudo-vector.

in order for the Maxwell's equation to be covariant. This can also be simply written as $\tilde{\boldsymbol{\epsilon}} = -\bar{\boldsymbol{\epsilon}}$ where $\bar{\boldsymbol{\epsilon}} = \mathbf{R}\boldsymbol{\epsilon}\mathbf{R}^{-1}$ where $\mathbf{R} = \text{Diag}\,[1, 1, -1]$ is the reflection operator. Geometrically the eigenvectors of $\bar{\boldsymbol{\epsilon}}$ are reflected copies of $\boldsymbol{\epsilon}$ while the eigenvalues of $\bar{\boldsymbol{\epsilon}}$ are the same as $\boldsymbol{\epsilon}$. Physically we interpret a material with $\bar{\boldsymbol{\epsilon}}$, as one which is a spatially reflected copy of a material with $\boldsymbol{\epsilon}$. Following from this then, a material with $\tilde{\boldsymbol{\epsilon}}$ is interpreted as a *spatially reflected copy* followed by an *inversion* of its eigenvalues.

Now if we were to reverse the argument and ask the question - given a half space ($z < 0$) filled with a material $\boldsymbol{\epsilon}(\boldsymbol{x}), \boldsymbol{\mu}(\boldsymbol{x})$, what material must we fill the other half space ($z > 0$) with so that the field solutions in this other half space is the reflected copy of the first, then the answer is simply $\tilde{\boldsymbol{\epsilon}}(\bar{\boldsymbol{x}}), \tilde{\boldsymbol{\mu}}(\bar{\boldsymbol{x}})$. So then the perfect lens theorem tells us that *given a slab of material* $\boldsymbol{\epsilon}(\boldsymbol{x}), \boldsymbol{\mu}(\boldsymbol{x})$, *we can always find it's optical complementary* $\tilde{\boldsymbol{\epsilon}}(\bar{\boldsymbol{x}}), \tilde{\boldsymbol{\mu}}(\bar{\boldsymbol{x}})$, *such that the net effect of propagation through these two materials are canceled out.* (see fig 4.1)

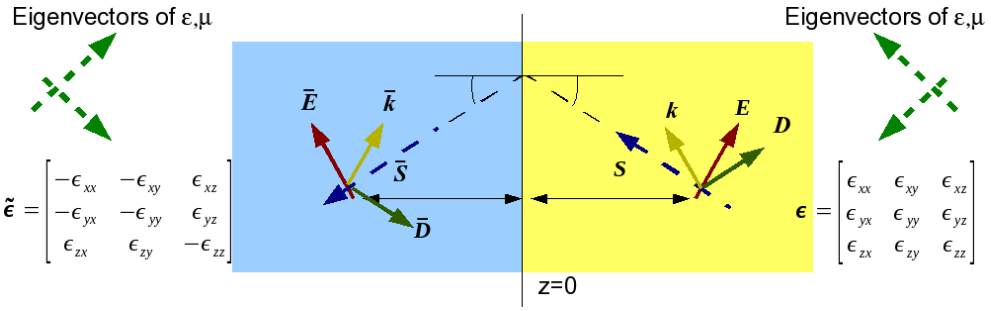


Figure 4.1: Illustration of the perfect lens theorem. The H and B fields, not drawn, are assumed to be out of plane. In essence PLT is a consequence of reflection symmetry in Maxwell's equations. It provides a prescription of what parameters a pair of complementary media must take in order for the overall electromagnetic effects to cancel out.

4.1.3 Consequence of Theorem

The connection between reflection symmetry of the *source-free* Maxwell's equations and PLT has a number of important implications. First, we note that since the Poynting vector defined by $\mathbf{S} = \mathbf{E} \times \mathbf{H}$, it is a pseudovector, like $\mathbf{D}$ and $\mathbf{B}$ fields. Similarly the wavevector $\mathbf{k}$ is a vector, and would transform like $\mathbf{E}$ and $\mathbf{H}$ fields

under reflection (see fig (4.1)). Now the symmetries of the $\{\mathbf{E}, \mathbf{H}, \mathbf{k}\}$ as vectors and $\{\mathbf{D}, \mathbf{B}, \mathbf{S}\}$ as pseudo-vectors, implies the following: First, boundary conditions are always satisfied. For instance, the reflection symmetry of vectors implies, the tangential components of $\mathbf{E}$ and $\mathbf{H}$ fields are continuous across the interface (at $z = 0$). Similarly for the wavevector $\mathbf{k}$, hence electromagnetic waves are always phase-matched. Second, it is comforting to know that the reflection symmetry of pseudo-vectors implies power flux or energy conservation at the interface, $\nabla.\mathbf{S} = 0$. The third major implication, the symmetries of both $\mathbf{k}$ and $\mathbf{S}$ implies that if one media supports forward waves ($\mathbf{k}.\mathbf{S} > 0$) , then it's optical complementary would always support backward waves ($\bar{\mathbf{k}}.\bar{\mathbf{S}} < 0$) (see fig (4.1)). This in turn implies that the phases ($\phi = \int_l \mathbf{k}.d\mathbf{l}$, where l is the path taken, and $d\mathbf{l} = \mathbf{S}/|\mathbf{S}|$) accumulated as a light ray traverses in a medium is exactly canceled out by the phases accumulated in the CM so that the net phase gain is zero. Further, because the reflection symmetry

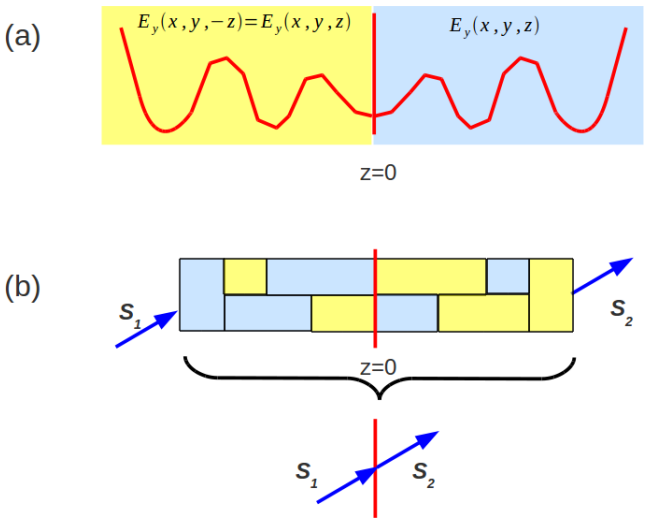


Figure 4.2: A complementary media behaves like an optical antimatter. If the yellow region is PRIM, the blue would be NRIM. Fig (a) illustrates the spatial reversal of fields which pass from a PRIM to a NRIM. Fig (b) a light ray S_1 traveling through a pair of complementary medium emerges as ray S_2, as if it does not see the intervening space. It appears as if the ray S_1 is translocated to S_2.

of $\mathbf{E}, \mathbf{H}$ fields holds for both propagating waves *and* evanescent near fields, decaying fields that approach the interface in a media would appear to be amplified in the CM (fig 4.2(a)). Thus the net effect of phase and amplitude reversal of the CM enables

one to view a CM as an *optical anti-matter* which nullifies the presence of a media (fig 4.2(b)). The design of a perfect lens can thus be viewed as selecting a suitable optical complementary/antimatter to annihilate the presence of the medium that one would like to see through. The fourth implication is the fact that if the surrounding media is a PRIM then its optical complementary would have to be a NRIM. We note from PLT, that the constitutive parameters of the complementary media, $\tilde{\boldsymbol{\epsilon}}(\bar{\boldsymbol{x}}), \tilde{\boldsymbol{\mu}}(\bar{\boldsymbol{x}})$ (eqn (4.3)), can be interpreted as being a *mirror copy* of the media except all its eigenvalues are *inverted* in sign (see fig 4.1). Thus if the medium we want to see through is made of PRIM (with positive eignenvalues for $\boldsymbol{\epsilon}, \boldsymbol{\mu}$) then the ideal lens which can see through such a medium, would *necessarily* have to be made of NRIM (with negative eigenvalues for $\tilde{\boldsymbol{\epsilon}}, \tilde{\boldsymbol{\mu}}$).Besides these implications of the PLT, about the nature of the perfect lens, there is still one very important caveat about the PLT that we should take note - the symmetry of fields only applies in the absence of sources (currents and charges). This means that as long as there are no sources between the object and image, then reflection symmetry would hold in between. The validity of the PLT can be extended by "mathematically" moving these sources and charges as we shall see later in section 6.3.1 to create a sourceless region.

4.2 Transformation optics

Transformation optics (TO) is a powerful and systematic tool based on the concept of *general covariance* [30, 31], which enables one to relate 2 geometrically different yet intrinsically equivalent electromagnetic configurations. This equivalence of electromagnetic configurations has 2 significant implications.

First, from a *passive*[2] point of view, TO presents a unifying approach to EM problems [32] - solving the fields in one configuration solves many at the same time - sometimes even complicated EM configurations can be re-expressed as simpler ones. For instance surface plasmon propagation on a simple slab can be related to surface plasmon propagation near/at complicated singular structures (kissing cylinders and

[2]The passive/active point of view is refers to the passive/active point of coordinate transformations. In the passive view, the object (vectors/physical quantities) remains unchanged while the coordinate frame of reference changes. In the active view, the frame of reference remains unchanged while the object changes.

sharp wedges) [78, 79]. Another example: a single EM algorithm can be adapted for either cylindrical or Cartesian coordinates by a simple modification of constitutive parameters [32] and so on.

Second, from an *active* point of view, transformations between two EM configurations can be viewed as being *effected* by a physical medium - a *transformation-media* [29]. Thus TO can be used as a systematic tool to design EM materials, which can distort fields in a controlled prescribed manner. For instance, in the design of EM cloaks [29, 33, 34], flatten Luneburg lens [36, 37], surface plasmon waveguides [35]; and as we shall see later, in the design of *compact perfect lenses* [23, 25, 26].

4.2.1 General covariance begets transformation optics

The principle of *general covariance* [30] is an immensely powerful concept, which states that *physical laws* (objective reality) should be invariant in *form* under arbitrary *coordinate transformation*s (descriptive perspective). It is precisely this concept which gives birth to the field of transformation optics.

The language best used to understand this comes from *differential geometry* [64]. In this section unless otherwise stated, p-forms are described by *italics*, while $\mathbf{p}$-vectors are described by **bold**-faced letters. First, from the integral form of Maxwell's equations (Eqn (3.2), (3.3)), we saw that E, H-fields are 1-forms ($E = E_i dx^i$ etc) while B, D-fields are 2-forms ($B = \frac{1}{2} B_{ij} dx^i \wedge dx^j$ etc). We can redefine the B, D 2-forms as the more familiar vector fields, $\mathbf{B} = B \rfloor \mathbf{e_3}$ where $\mathbf{B} = B^i \partial_i$ is now a 1-*vector density* (we shall see in a minute) and $\mathbf{e_3} = \frac{1}{3!} \varepsilon^{ijk} \partial_i \wedge \partial_j \wedge \partial_k$ is the spatial 3-*vector density* where ε^{ijk} is the Levi-Civita symbol. In addition to the fields we can also define a current 2-form j and charge 3-form ρ. Using the language of differential geometry, Maxwell's equations can now be rewritten in a compact, coordinate-free form [31, 65] as:

$$d_{(4)} F = 0, \qquad d_{(4)} G = \gamma \tag{4.4}$$

where $F = B + E \wedge dt$ and $G = D - H \wedge dt$ are the Faraday 2-form and Source field 2-form respectively. The space-time differential operator is: $d_{(4)} = d + \partial_t dt$, where d is the spatial differential operator. Assuming linearity, the Faraday 2-form F is related to the source field G by the *constitutive relations*

$$G = \chi | F \tag{4.5}$$

where χ is the constitutive parameter dyadic[3]. Disregarding magneto-electric coupling, then the constitutive relations can be simply written in the familiar form:

$$\mathbf{D} = D\rfloor\mathbf{e_3} = \boldsymbol{\epsilon}|E, \qquad \mathbf{B} = B\rfloor\mathbf{e_3} = \boldsymbol{\mu}|H \tag{4.6}$$

where $\epsilon = \epsilon^{ij}\partial_i \otimes \partial_j$ and $\mu = \mu^{ij}\partial_i \otimes \partial_j$ are the permittivity and permeability *tensor densities*.

Now covariance implies that the form of physical laws are unchanged, that is eqn (4.4)-(4.6) are invariant under coordinate transformations. To discuss transformations we need more notations. Quantities which are transformed shall be denoted by over-bars $Q \to \bar{Q}$ thus coordinates are transformed as $\mathbf{x} \to \bar{\mathbf{x}}$. The demand for covariance for eqn (4.4) implies covariance of the differential forms, E, H, D, B, where

$$E = \bar{E}, \quad H = \bar{H}, \quad D = \bar{D}, \quad B = \bar{B} \tag{4.7}$$

Thus $E = E_i dx^i = \bar{E} = \bar{E}_{\bar{i}} d\bar{x}^{\bar{i}}$ and so on, and since we know how the differential basis transforms under chain rule as $dx^i = \frac{\partial x^i}{\partial \bar{x}^{\bar{i}}} d\bar{x}^{\bar{i}}$, the components of 1-forms will transform as

$$\bar{E}_i = E_i \underline{\Lambda}^i_{\bar{i}}, \qquad \bar{H}_i = H_i \underline{\Lambda}^i_{\bar{i}} \tag{4.8}$$

where $\underline{\Lambda}^i_{\bar{i}} = \frac{\partial x^i}{\partial \bar{x}^{\bar{i}}}$, (the inverse of $\underline{\Lambda}$ is $\overline{\Lambda}^{\bar{i}}_i = \frac{\partial \bar{x}^{\bar{j}}}{\partial x^i}$). Similarly the 2-forms transform as

$$\bar{D}_{\bar{i}\bar{j}} = D_{ij} \underline{\Lambda}^i_{\bar{i}} \underline{\Lambda}^j_{\bar{j}}, \qquad \bar{B}_{\bar{i}\bar{j}} = B_{ij} \underline{\Lambda}^i_{\bar{i}} \underline{\Lambda}^j_{\bar{j}} \tag{4.9}$$

To see that $\mathbf{B}, \mathbf{D}$ transforms as vector densities we note that $\mathbf{e_3}$ transforms as a *3-vector density*:

$$\begin{aligned}
\mathbf{e_3} &= \frac{1}{3!}\varepsilon^{ijk}\partial_i \wedge \partial_j \wedge \partial_k \\
&= \frac{1}{3!}\varepsilon^{ijk}\overline{\Lambda}^{\bar{i}}_i \overline{\Lambda}^{\bar{j}}_j \overline{\Lambda}^{\bar{k}}_k \partial_{\bar{i}} \wedge \partial_{\bar{j}} \wedge \partial_{\bar{k}} \\
&= \det(\overline{\Lambda}).\frac{1}{3!}\varepsilon^{\bar{i}\bar{j}\bar{k}}\partial_{\bar{i}} \wedge \partial_{\bar{j}} \wedge \partial_{\bar{k}} \\
&= \det(\overline{\Lambda})\bar{\mathbf{e}}_{\mathbf{3}}
\end{aligned} \tag{4.10}$$

where we used the properties of determinants.

Now the demand for covariance for fields E, H, B, D (eqn (4.7)) and for the constitutive relations (eqn (4.6)) implies that, since L.H.S of eqn (4.6) transforms as

[3] A Hodge star operator

vector densities the ϵ, μ should transform as *tensor densities*. That is

$$\epsilon|E = D\rfloor\mathbf{e_3} = \det(\overline{\Lambda})\bar{D}\rfloor\bar{\mathbf{e}}_\mathbf{3} = \det(\overline{\Lambda})\bar{\epsilon}|\bar{E}$$

therefore $\epsilon = \det(\overline{\Lambda})\bar{\epsilon}$ transforms as a *tensor density*. This when written in component form would give us [80]:

$$\bar{\epsilon}^{\bar{i}\bar{j}} = \epsilon^{ij}\frac{\overline{\Lambda}_i^{\bar{i}}\overline{\Lambda}_j^{\bar{j}}}{\det(\overline{\Lambda})}, \qquad \bar{\mu}^{\bar{i}\bar{j}} = \mu^{ij}\frac{\overline{\Lambda}_i^{\bar{i}}\overline{\Lambda}_j^{\bar{j}}}{\det(\overline{\Lambda})} \tag{4.11}$$

Thus, through the principle of covariance, when given a particular diffeomorphism, we have a prescription to describe the *same field configuration* with *different coordinate frames* (perspectives). The formulation that is presented in this section has two caveats. First, the simplified constitutive relations (eqn (4.6)) and spatial transformation $\underline{\Lambda}$ that were used, are not Lorentz invariant, thus only applies to diffeomorphisms between local rest frames. Though this can be easily extended if we use the more general constitutive relations (eqn (4.5)) and include the full Lorentz transformations (boosts) [81, 82]. The second caveat is the spatial transformation $\underline{\Lambda}$ only applies to *proper* transformations (rotations, dilations and shears)[4] in order to keep charges invariant under transformations [31, 83]. This caveat can therefore be bypassed only in regions of space where charges and currents are absent.

4.2.2 Transformation media

We have seen how fields and constitutive parameters transforms under diffeomorphisms; in this section we shall consider how this concept of covariance can be translated into a physical media - *transformation media* [29, 84] - which effects such transformations. The derivation of transformation media from transformation optics is a two step process. The first step is to find a suitable *diffeomorphism* to distort coordinate surfaces to the desired geometry. The second step is to *re-interpret* this diffeomorphism as being effected by a physical medium (fig 4.3(a)) [81, 82]. First we begin from a space where field configurations are simple, and we shall call this space the *electromagnetic space* (fig 4.3(b)). For discussion purposes, in this section,

[4]That is because the charge 3-form ρ, hence the source field G are really a *twisted-forms*. Thus in the transformations of H and D (eqn (4.8), (4.9)) and consequently the constitutive relations eqn(4.11) should be pre-multiplied by a factor of $\mathrm{sgn}(\det(\overline{\Lambda}))$. The reason for the introduction of *twisted-forms* is to keep charges invariant under *improper* transformations.

we shall assume that the electromagnetic space is vacuum ($\boldsymbol{\epsilon(x)}, \boldsymbol{\mu(x)} = 1$), and the fields can be represented by simple, straight ray trajectories.

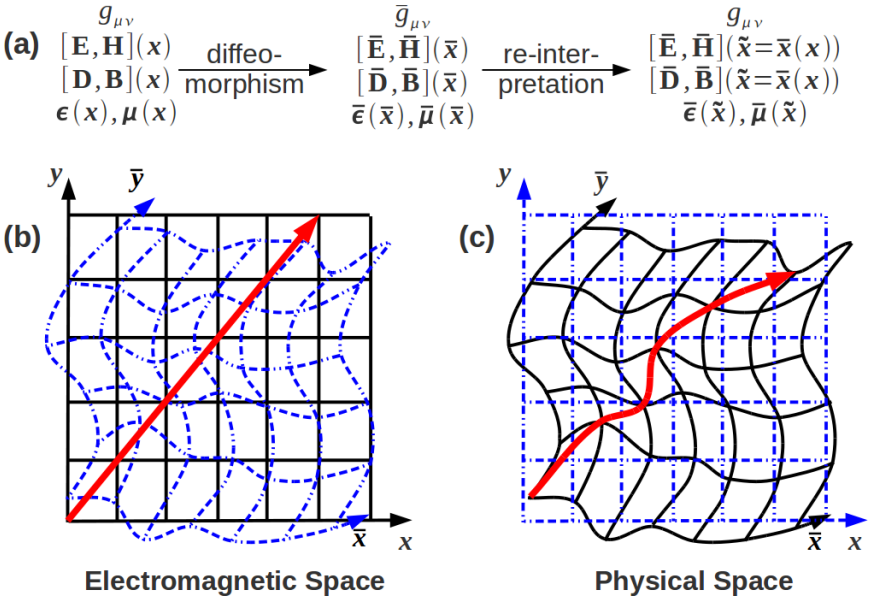


Figure 4.3: Illustration of transformation optics. Fig (a) transformation optics is a 2 step process - first a diffeomorphism from $\boldsymbol{x} \rightarrow \bar{\boldsymbol{x}}$ followed by re-interpretation of this transformation as an effective medium [81, 82, 84] (figure adopted from [82]). Fig (b) we begin from an electromagnetic space $(\boldsymbol{\epsilon(x)}, \boldsymbol{\mu(x)})$ with a simple configuration of fields (red arrows), then we perform a diffeomorphism (from black grids to blue-dashed grids). Fig (c) the fields (curved-red arrows) are carried along by the diffeomorphism to a new configuration (black grids). We now re-interpret this new configuration using physical coordinates (blue-dashed grids). The re-interpretation process, sees the physical space as being effectively filled with a physical *transformation-media* $(\bar{\boldsymbol{\epsilon}}(\tilde{\boldsymbol{x}}), \bar{\boldsymbol{\mu}}(\tilde{\boldsymbol{x}}))$, where fields would distort in the same way as the diffeomorphism - in other words, the transformation-media implements the coordinate transformation. Although the field configurations between the electromagnetic and physical spaces appears *geometrically different* they are *covariantly equivalent*.

Let us suppose that the electromagnetic space can be described by either Cartesian ($\{\mathbf{x}\}$), or some arbitrary curvilinear coordinates ($\{\bar{\mathbf{x}}\}$), and let $f : \mathbf{x} \rightarrow \bar{\mathbf{x}}$ be the desired map between these coordinate systems. We have already seen in the previous section, this coordinate transformation in space will also result in a transformation of the field *components* (eqn (4.8),(4.9)). However from the principle of general co-

variance, which coordinate system to use is irrelevant, the fields remains unchanged since they are still embedded in vacuum. In Cartesian coordinates, light rays are straight, while for some curvilinear coordinates, curvilinear rays are also "straight" from the perspective of curvilinear basis.

The next step then is to *re-interpret* this diffeomorphism *not* in the new curvillinear $\bar{\mathbf{x}}$-coordinates, but using the old Cartesian $\mathbf{x}$-coordinates, in a *new space* - the *physical Space* - where light rays are now "bent" in the way we desire (fig 4.3(c)). In this new physical space, the vacuum is now replaced with a physical medium defined by $\bar{\boldsymbol{\epsilon}}, \bar{\boldsymbol{\mu}}$ which is prescribed by eqn (4.11). Now one may view such a physical media, as a *transformation media* which implements the coordinate transformation $f : \mathbf{x} \to \bar{\mathbf{x}}$. Using this method, we can now design materials which can distort EM fields in a controlled way. Such transformation media has already been demonstrated in applications: cloaks, where light was made to bend around objects rendering them invisible [29, 33, 34]; surface plasmon waveguides, where surface plasmons are similarly guided as light wave in optic fibers [35]; redesign of curved image planes, as in the flattened Luneburg lens [36, 37] and so on. Other than these light guiding applications, transformation media can also be used for design of perfect lenses with arbitrary geometry, which we shall study in the next chapter.

4.2.3 Anisotropy in transformation

One common property of transformation-media is the material constitutive parameters are usually *anisotropic*. The presence of anisotropy in transformation-media is not inevitable [33], nor is it always detrimental [85]. However sometimes anisotropy can be a problem, especially anisotropy in the permeability implies the need for magnetic metamaterials, which are more difficult to engineer and have more losses, than materials with anisotropy in permittivity. In this section we shall understand the origins of anisotropy in transformation-media, and in the next section we shall briefly discuss how one might minimise this.

First we begin with a simple example with a simple transformation (fig 4.4). We begin from an electromagnetic space which is vacuum (fig 4.4(a)) and stretch some region of this space by a factor of a in the x-direction (fig 4.4(b)). From eqn (4.11), we can easily obtain the permittivity and permeability of the transformation-media as

$\text{diag}(\bar{\epsilon}_x, \bar{\epsilon}_y, \bar{\epsilon}_z) = \text{diag}(\bar{\mu}_x, \bar{\mu}_y, \bar{\mu}_z)$, where $\bar{\epsilon}_x = \bar{\mu}_x = a$, $\bar{\epsilon}_y = \bar{\mu}_y = 1/a$, $\bar{\epsilon}_z = \bar{\mu}_z = 1/a$. Note the resulting anisotropy. We can work out the wave-vector of light in the various directions within the transformation-media, namely $k_x = \sqrt{\epsilon_y \mu_z} k_0 = \sqrt{\epsilon_z \mu_y} k_0 = k_0/a$, $k_y = \sqrt{\epsilon_x \mu_z} k_0 = \sqrt{\epsilon_z \mu_x} k_0 = k_0$ and $k_z = \sqrt{\epsilon_x \mu_y} k_0 = \sqrt{\epsilon_y \mu_x} k_0 = k_0$. From this we can easily work out how the transformation-media bends light. If an incident light ray makes an angle θ_i with the x-axis, it is refracted by the transformation-media by an angle of θ_r, where $\tan(\theta_r) = a^{-1} \tan(\theta_i)$ (fig 4.3(b)), just as we had designed it to. Note the act of stretching solely in the x-direction resulted in the anisotropy in the $x - y$ or $x - z$ plane. Similarly preserving the aspect ratio of the $y - z$ plane results in isotropy in the $y - z$ plane. Thus from this simple example, we can conclude that the degree of *anisotropy* is dependent on the *asymmetry* of a unit cube due to the diffeomorphism.

To see this more quantitatively, we can consider a more general case of dilations in all x, y, z-directions. Suppose we have a diffeomorphism is such that, for each unit cube ($\{dx, dy, dz\}$) in free space ($\boldsymbol{\epsilon} = \boldsymbol{\mu} = \mathbf{1}$), undergoes a dilation such that $d\bar{x} = a.dx$, $d\bar{y} = b.dy$, $d\bar{z} = c.dz$. Then using eqn (4.11), the constitutive parameters for the transformation-media is given by $\text{diag}(\bar{\epsilon}_x, \bar{\epsilon}_y, \bar{\epsilon}_z) = \text{diag}(\bar{\mu}_x, \bar{\mu}_y, \bar{\mu}_z)$, where $\bar{\epsilon}_x = \bar{\mu}_x = a/(bc)$, $\bar{\epsilon}_y = \bar{\mu}_y = b/(ac)$, $\bar{\epsilon}_z = \bar{\mu}_z = c/(ab)$. Thus if we maintained the aspect ratio $b = c \neq a$, then we would arrive at the same results as before - isotropy only in the $y - z$ plane. The result we have obtained also holds for more general proper transformations, such as rotations and shearing, where a, b, c would now correspond to the dilations along the principal axes.

4.2.4 Minimising anisotropy - beyond the quasi-conformal transformation

We have seen that the degree of anisotropy is dependent on the diffeomorphism used. Given certain boundary conditions (say the final shape of the transformed media), the transformation we use, hence the transformation-media we obtain, is *non-unique* - there are more than one diffeomorphisms between electromagnetic and physical spaces. Here we will examine how to derive a class of diffeomorphisms which *minimises* the degree of anisotropy.

The class of diffeomorphisms which *maintains* isotropy in 2-d (planes mapped to

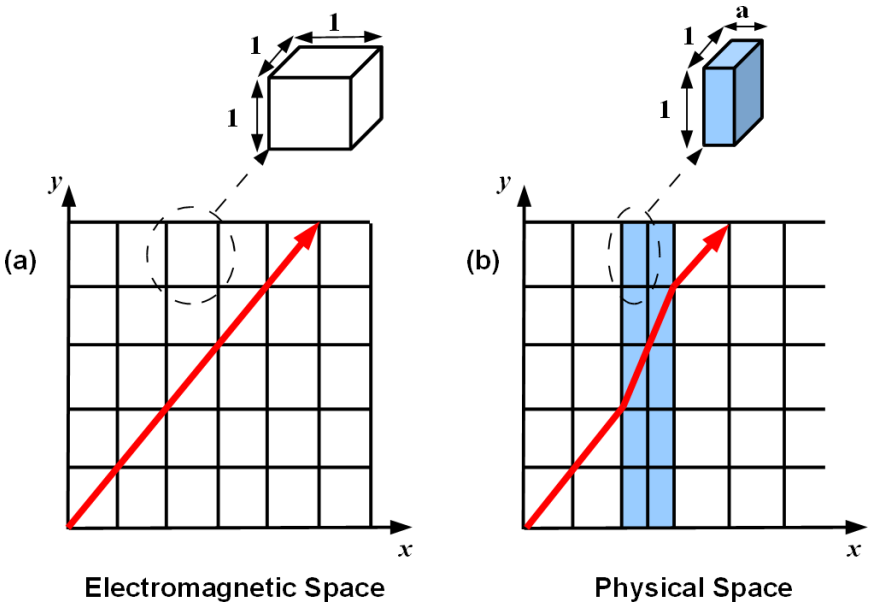


Figure 4.4: Degree of anisotropy depends on asymmetry/aspect ratio of transformed unit cells. Fig (a) the electromagnetic space is vacuum, and the ray trajectories (red arrow) are straight rays. Fig (b) in the physical space, a transformed-media (shaded blue) has permittivity and permeability, $\mathrm{diag}(\bar{\epsilon}_x, \bar{\epsilon}_y, \bar{\epsilon}_z) = \mathrm{diag}(\bar{\mu}_x, \bar{\mu}_y, \bar{\mu}_z)$, where $\bar{\epsilon}_x = \bar{\mu}_x = a, \bar{\epsilon}_y = \bar{\mu}_y = 1/a, \bar{\epsilon}_z = \bar{\mu}_z = 1/a$, which would bend light (bent-red arrow) as shown in the figure. Note the degree of anisotropy is a function of a.

planes) are the *conformal* maps. If we are given a finite space with fixed boundaries to perform the transformation, we may not be able to find a suitable conformal transformation. We can relax this restriction by allowing some (but minimal) anisotropy, and such transformations are known as the *quasi-conformal* maps. Because transformation media obtained from quasi-conformal maps are nearly isotropic for a 2-d plane, such material can be further approximated to be non-magnetic ($\mu = 1$), without much deviation from the ideal as long as the incident EM wave is confined to a 2-d plane. Being non-magnetic, these "approximate" quasi-conformal transformation media are obviously easier to fabricate, and has been successfully demonstrated in a number of applications: such as 2-d carpet cloaks [33, 34], and flatten Luneburg lens [37] with zero-aberration and ultrawide field of vision. While conformal and quasi-conformal maps have obvious advantages these maps are valid only for 2-d maps from planes to planes. Although higher dimensional conformal maps do exist,

they are extremely restrictive[5].

Therefore there is great value and, we shall briefly explore how one might extend the idea of quasi-conformality beyond 2-d. To do so, first we would need a reasonable measure of anisotropy. Since the metric (g_{ij}) is a measure of distance ($ds^2 = g_{ij}dx^i dx^j$), a measure of anisotropy based on the metric would be a good starting point. Let's suppose that the electromagnetic space has a Euclidean metric $g_{ij} = \delta_{ij}$, then the metric of the transformed space would be $\bar{g}_{\bar{i}\bar{j}} = \underline{\Lambda}^i_{\bar{i}} g_{ij} \underline{\Lambda}^j_{\bar{j}}$, where $\underline{\Lambda}^i_{\bar{i}} = \frac{\partial x^i}{\partial \bar{x}^{\bar{i}}}$ (written in matrix form this gives $\bar{\mathbf{g}} = \underline{\mathbf{\Lambda}}^\top \underline{\mathbf{\Lambda}}$). Suppose that the j^{th} eigenvalues of the metric $\bar{\mathbf{g}}$ at position $\mathbf{x} = \mathbf{x}_i$ is given by $\{\lambda_i^{(j)}\}$. Then a suitable measure for anisotropy would be

$$\beta_N \propto \sum_{i=-\infty}^{\infty} \sum_{j=1}^{N} \left(\lambda_i^{(j)} - \frac{\mathrm{Tr}(\bar{\mathbf{g}}_i)}{N} \right)^2 \tag{4.12}$$

where $\mathrm{Tr}(\bar{\mathbf{g}}_i)$ is the trace of the metric at $\mathbf{x} = \mathbf{x}_i$, and N is the dimension of the space. Physically the terms in the rounded brackets is a measure of the deviation of the eigenvalues from an average value defined by the trace. We can rewrite the summation terms in eqn (4.12) in a *manifestly covariant* form by using $\mathrm{Tr}(\bar{\mathbf{g}}_i) = \sum_{j=1}^{N} \lambda_i^{(j)}$ and $\mathrm{Tr}(\bar{\mathbf{g}}_i^2) = \sum_{j=1}^{N} \lambda_i^{(j)2}$. The measure of anisotropy we obtained then is given by:

$$\beta_N = \int_\Omega \frac{d\mathbf{x}^3}{\sqrt{\bar{g}}} W(\mathbf{x}) \left(\mathrm{Tr}(\bar{\mathbf{g}}^2(\mathbf{x})) - \frac{1}{N} \mathrm{Tr}(\bar{\mathbf{g}}(\mathbf{x}))^2 \right) \tag{4.13}$$

where we replaced the summation with integrals over a volume Ω; $\bar{g}$ is the determinant of the metric and $W(\mathbf{x})$ is an arbitrary weighting function which we can set to make the integrand dimensionless. The weight to use should also be manifestly covariant, thus we can use $W(\mathbf{x}) = \bar{g}^{2/N}$.

We can easily see that for $N = 2$ dimensions, from eqn (4.13), β_N reduces to

$$\beta_2 = \int_\Omega \frac{d\mathbf{x}^3}{\sqrt{\bar{g}}} \left(\frac{1}{2} \frac{\mathrm{Tr}(\bar{\mathbf{g}}(\mathbf{x}))^2}{\bar{g}} - 2 \right) \tag{4.14}$$

which is precisely the modified-Liao functional used by Li and Pendry [33] as a measure of anisotropy. By minimising eqn (4.14), subject to slipping boundary conditions, we can therefore obtain the 2-D quasi-conformal maps.

Thus by minimising β_N (eqn (4.13)), we have a method for deriving classes of diffeomorphisms which minimises anisotropy for $N > 2$ dimensions. One can

[5]The only higher dimensional conformal maps are stereographic projections or inversions.

either solve the minimisation of β_N, using calculus of variations from which we would obtain the Euler-Lagrange equations[6]; or we can solve the minimisation by numerical methods. At this point we should also note that β_N as defined in eqn (4.13) is dependent on the weighting function which is non-unique. Instead of using determinants we could have used say $W(\mathbf{x}) = \mathrm{Tr}(\bar{\mathbf{g}}(\mathbf{x}))^2$ which maybe simpler to evaluate[7].

4.3 Generalised PLT

In section 4.1 we have introduced the concept of perfect lens theorem (PLT) through which we can extend the concept of the simple $\epsilon = \mu = -1$ flat perfect lens to a more general *anisotropic*, *inhomogeneous*, but *flat* perfect lens. In section 4.2, we demonstrated how we can relate electromagnetic configurations with different *geometry*, through the concept of transformation optics. Moreover, such a mathematical relation can be made physical and implemented through transformation-media. Combining the concept of PLT with transformation optics, we can therefore further generalise and extend the perfect lens from a flat lens to a lens with an *arbitrary geometry*. The procedure is simple, first we choose an appropriate diffeomorphism which flattens coordinate surfaces, then we can apply PLT in this flatten cartesian coordinates, following which we would transform back to the original curvillinear coordinates, to obtain a curved perfect lens. The details of this procedure will be deferred to section 5.2. Now to the astute reader, one may already realise that transformation optics is the more general framework, and within this framework PLT is only one particular type of transformation optics. If we include *improper* transformations such as reflections (or according to Ulf [81], *folding transformations*) we would obtain PLT as a specific example. However regardless of PLT or improper-transformation optics, both methods have an important caveat, that is the region of validity must be *source-free* (no charges or currents), in order for fields in CM to be mirror images of each other. Care must therefore be taken when applying improper transformations, for spaces with sources [83], as the physical implications can

[6] We may have to solve a $\frac{N^2+N}{2}$ coupled PDE.

[7] For instance, using such weight, for $N = 2$, we get $\beta_2 = \int_\Omega \frac{d\mathbf{x}^3}{\sqrt{\bar{g}}} \left(2.\frac{\bar{g}}{\mathrm{Tr}(\bar{\mathbf{g}}(\mathbf{x}))^2}\right)$ which has an integrand that is inverse of the modified-Liao functional.

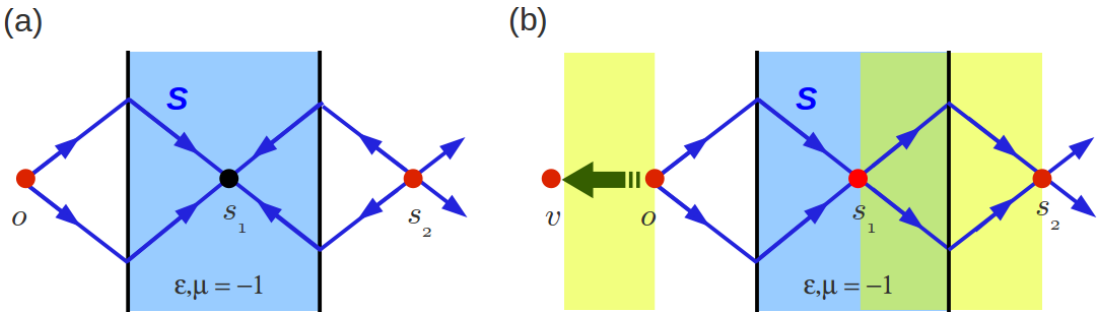


Figure 4.5: Fig (a) when improper-transformations are applied indiscriminately, to maintain covariance, we would need to artificially place a sink (black dot) and source (red dot) at the image points s_1 and s_2. Note the power flow S (blue arrows). Fig (b) an alternative approach, is to first mathematically "move" the point source o backwards to a virtual source v, whereby the space is now source-free and symmetries of fields from PLT/improper transformations can be applied. The yellow region is now source-free though it has become *anomalously* divergent [86, 87]. See section 6.3.1 and 6.3.3 for further details.

be drastically different (fig 4.5 illustrates this). If we impose the symmetries from improper-transformations indiscrimnately over regions with sources, then in order to maintain covariance, we would need to artificially add physical sinks/sources at the image points (fig 4.5(a)). A more causally feasible procedure, is to first mathematically "move" the point source backwards to create a source-free region of space, before applyling the field symmetries from PLT/transformation optics (fig 4.5(b)). This way we would not need to add artificial sinks/sources at the image points s_1 and s_2; though in exchange we would create an *anomalously* divergent region of fields [8]. The procedure to mathematically "move" the points sources and how to resolve this seemingly unphysical divergent region of fields shall be further discussed in chapter 6 (section 6.3.1 and 6.3.3).

[8] Milton *et al* [86, 87] refers to this divergent region as anomalous divergent

5. Applications of the compact perfect lens I

As we have seen (section 4.1), a perfect lens can be regarded as a complementary media to its surrounding environment. The optical cancellation of the surrounding media with its complementary, followed by the *translocation* of the optical fields from the object to image plane, is what we regard as imaging. And the entire process of optical cancellation and translocation is then what we regard as *perfect lensing.*

In the flat geometry this translocation is merely a translation from one plane to another. Optical information is faithfully transferred, though subwavelength features remains subwavelength, hence invisible in the far-field. For a class of perfect lenses, with compact geometry - the *compact perfect lens* (CPL) - this translocation is both a translation and *magnification* of the object plane [23]. If such magnification is large enough, this opens up a possibility of magnifying subwavelength objects to become images visible in the far-field. In other words we have a means to transform evanescent near-fields in the object plane to propagating far-fields (a type of hyper-lens [88–90]). In this and the following chapter, we shall focus on the properties and applications of such CPL. The applications hence the chapters are broadly divided into two. For this chapter, we shall explore the *scattering* properties of CPL, and show how a conventional scatterer when combined with the CPL will lead to a class of *super-scatterers.* Following this, in the next chapter, we shall explore the *transmission* properties of CPL, and show how when combined with a phase array, we would obtain the *super phase arrays.* For both chapters we shall see how CPL can enhance the properties of objects embedded within over and beyond what can be achieved conventionally.

This chapter is broadly divided into 3 parts. First we shall examine what are

super-scatterers and how we can construct them (section 5.1 and 5.2). Following this we shall present the numerical models we use to study them (section 5.3). Finally we shall examine three specific examples of such super-scatterers, and see how the presence of CPL enhances the scattering properties of these scatterers (section 5.4), and conclude this chapter with some remarks about applications (section 5.5).

5.1 What are super-scatterers?

The combination of a CPL with a scatterer is a super-scatterer (SS) [24, 25]. It is "super" because such a scatterer has an enhanced scattering cross section much larger than its physical size. While, it has been known that, normal, conventional, *resonant scatterers* interact with the *waves* of incident radiation in such a manner that their scattering cross sections can be much larger than their physical sizes [2, 70], however, for large *non-resonant scatterers* these interactions are mainly with *rays* in the regime of geometrical optics. Hence the scattering cross sections of such normal scatterers are only of the order of the physical cross section - for instance, a big object would cast a sharp shadow that has the same size as the object.

For such a normal conventional scatterer, one might enlarge scattering cross section by using conventional lens to capture light rays which impact on the lens. However such an endeavor can never generate an image bigger than the physical dimension of the scatterer (that is the lens). In contrast a super-scatterer can do much better, by capturing light rays which do not impact the lens, to form an image larger than the physical size of the lens (fig 5.1). The role of the CPL then, is akin to "converting" a non-resonant scatterer to a composite, resonant, *super* scatterer. To see this significance, in this chapter, the scatterers which we shall "convert", are mainly non-resonant and electromagnetically large, hence in the domain of geometrical optics. We shall see how the presence of the CPL can enhance these *geometrical* scattering properties by blurring the lines between ray and wave optics. To this end we shall examine three specific types of Super-Scatterers - the *transparent SS* [24], the *absorber SS* and the *retro-reflector SS* [25]. First, through the transparent SS, we will show how a super-scatterer can map an internal space to an external space much larger than itself. Second, we will show how an absorber SS can cast a larger shadow than its physical size and finally we will demonstrate the use of SS to create

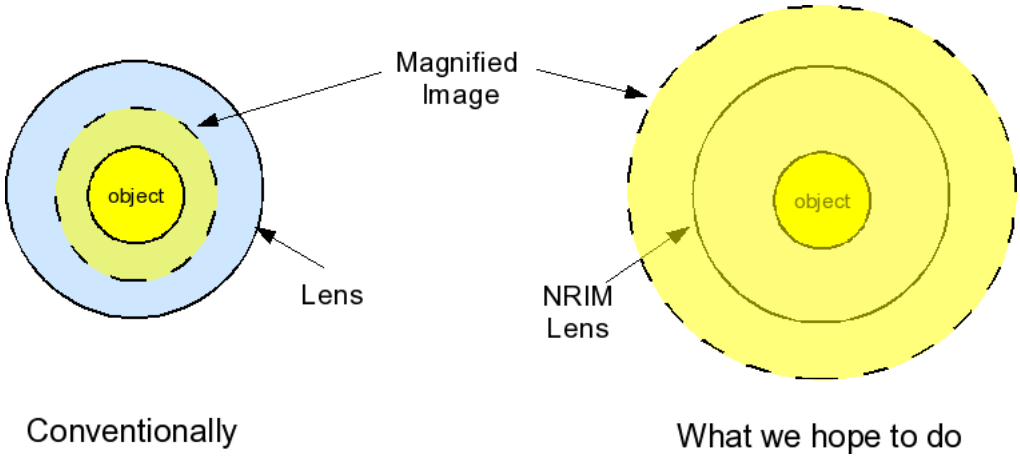


Figure 5.1: The scattering cross section of a super-scatterer contrasted with a normal conventional scatterer.

a *super all-angle retro-reflector*.

5.2 Constructing the super-scatterer

As briefly described in section 4.3, using the tools of transformation optics (TO) and PLT we have a systemative strategy of creating a CPL, which can be combined with a normal scatterer to form a super-scatterer. Fig 5.2 shows a brief schematic of our strategy. First we divide space into 3 compact regions, labeled 1, 2 and 3, with region 3 surrounded by 2 and so forth. Let the permittivity and permeability of the 3 regions be denoted by tensors $\boldsymbol{\epsilon_I}$ and $\boldsymbol{\mu_I}$, where the subscript $I = 1, 2, 3$ denotes the respective regions. Without loss of generality, we can suppose that region 1 is filled with $\boldsymbol{\epsilon_1} = \boldsymbol{\mu_1} = 1$ (or vacuum), and region 3 is where we place our object that we want to magnify. Now we begin by asking the question, what material must we fill region 2 with so that $\boldsymbol{\epsilon_2}, \boldsymbol{\mu_2}$ in region 2 would be complementary to $\boldsymbol{\epsilon_1}, \boldsymbol{\mu_1}$ in region 1. In other words what material property must the CPL in region 2 have.

To accomplish this we need to use a suitable map f that can map the compact regions 1,2,3 (with coordinates $\{x, y, z\}$ in fig 5.2) to a planar slabs which we denote as regions $1', 2', 3'$ (with coordinates $\{u, v, w\}$). If such a map exist, we can use the concepts of transformation optics, to transform $\boldsymbol{\epsilon_1}, \boldsymbol{\mu_1}$ of region 1 (using eqn (4.11)) to $\bar{\boldsymbol{\epsilon}}_{\mathbf{1}}, \bar{\boldsymbol{\mu}}_{\mathbf{1}}$ of region $1'$. Next, we can apply the concepts of PLT (using eqn (4.3)) to determine $\bar{\boldsymbol{\epsilon}}_{\mathbf{2}}, \bar{\boldsymbol{\mu}}_{\mathbf{2}}$ so that region $2'$ can be complementary to Region $1'$. Finally we

can apply transformation optics in reverse to determine the required $\boldsymbol{\epsilon_2}, \boldsymbol{\mu_2}$. The composite structure of the object (with $\boldsymbol{\epsilon_3}, \boldsymbol{\mu_3}$) together with the CPL (with $\boldsymbol{\epsilon_2}, \boldsymbol{\mu_2}$) is therefore our required SS. As mentioned previously, the presence of the CPL not

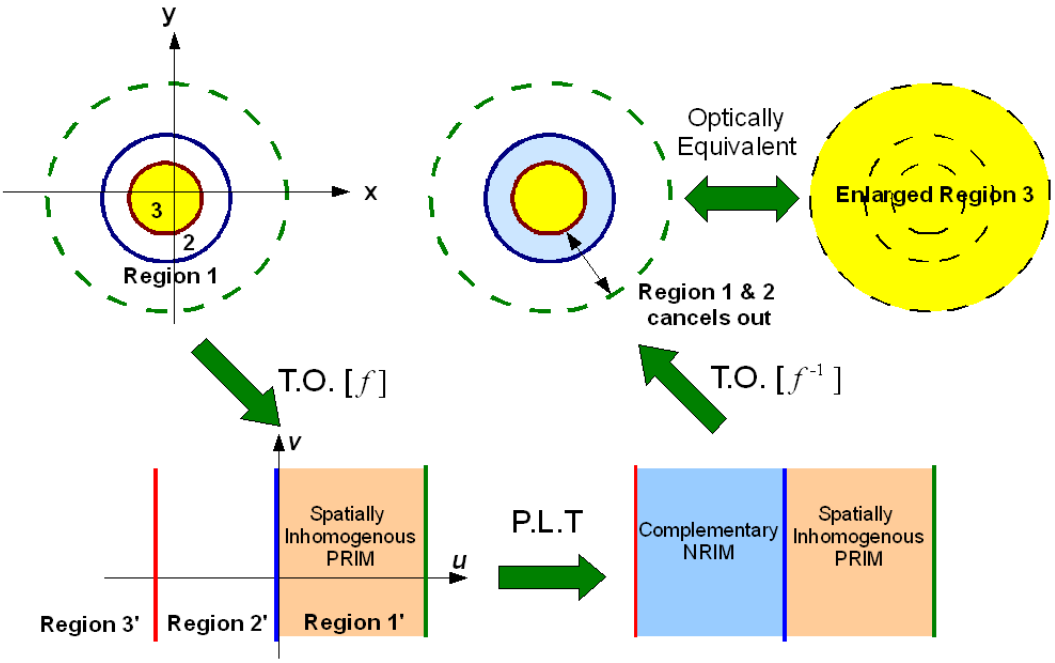


Figure 5.2: Illustration of the creation of super scatterers. A map f is used to map regions 1,2,3 to regions $1', 2', 3'$. Transformation optics (TO) is used to determine the permittivity and permeability, $\bar{\boldsymbol{\epsilon}}_{\boldsymbol{I}}, \bar{\boldsymbol{\mu}}_{\boldsymbol{I}}$ in regions $1', 2', 3'$, from $\boldsymbol{\epsilon_I}, \boldsymbol{\mu_I}$ in regions 1,2,3, (where $\boldsymbol{I} = 1, 2, 3$ is the index for the respective regions). Perfect lens theorem (PLT) is used to determine the complementary medium

only optically cancels the surrounding space, it also *translocates* the interior (region 3) to the exterior (region 1). This stretching of space modifies the properties of the embedded scatterer therefore need to be accounted for.

Now, suppose if the permittivity and permeability of region 3 is given by $\boldsymbol{\epsilon_3}(\boldsymbol{x})$ and $\boldsymbol{\mu_3}(\boldsymbol{x})$. And if Γ is a map which enlarges region 3 to fill up the optically canceled region (Region 1+2) [1]. Then the effective permittivity and permeability, $\boldsymbol{\epsilon}_{\text{eff}}, \boldsymbol{\mu}_{\text{eff}}$, of the super scatterer we have obtained in the procedure above, would (from eqn

[1] If $\partial\Omega_3$ and $\partial\Omega_1$ are the outer boundaries of Region 3 and 1 respectively, then $\Gamma : \partial\Omega_3 \rightarrow \partial\Omega_1$

(4.11)) be given by:

$$\boldsymbol{\epsilon}_{\text{eff}}(\Gamma(\boldsymbol{x})) = \frac{\Gamma'\boldsymbol{\epsilon_3}(\boldsymbol{x})\Gamma'^{\top}}{|\Gamma'|},\ \boldsymbol{\mu}_{\text{eff}}(\Gamma(\boldsymbol{x})) = \frac{\Gamma'\boldsymbol{\mu_3}(\boldsymbol{x})\Gamma'^{\top}}{|\Gamma'|} \tag{5.1}$$

where $\Gamma' = \frac{\partial \Gamma}{\partial \boldsymbol{x}}$ and $|\Gamma'|$ is the determinant of Γ' . If this scaling is isotropic (that is $\Gamma(\boldsymbol{x}) = \gamma\boldsymbol{x}$, where γ is the scaling factor to enlarge region 3) then eqn (5.1) can be reduced to

$$\boldsymbol{\epsilon}_{\text{eff}}(\gamma\boldsymbol{x}) = \frac{\boldsymbol{\epsilon_3}(\boldsymbol{x})}{\gamma},\ \boldsymbol{\mu}_{\text{eff}}(\gamma\boldsymbol{x}) = \frac{\boldsymbol{\mu_3}(\boldsymbol{x})}{\gamma} \tag{5.2}$$

Now suppose if on the other hand, we want to design a super-scatterer with an effective size of $\gamma\Omega_3$ (where Ω_3 is the volume of region 3) with an effective permittivity and permeability, $\boldsymbol{\epsilon}_{\text{eff}}, \boldsymbol{\mu}_{\text{eff}}$, we can reverse eqn (5.2) to determine what permittivity and permeability, $\boldsymbol{\epsilon_3}, \boldsymbol{\mu_3}$ we should fill region 3 with.

5.2.1 Example - a cylindrical SS

Now that we have seen the general principles of how to create a SS, we will show an explicit example of how to create a cylindrical super-scatterer [91] using these principles. Let $\{x^i\} = (x, y, z)$ be the Cartesian coordinates to describe a set of

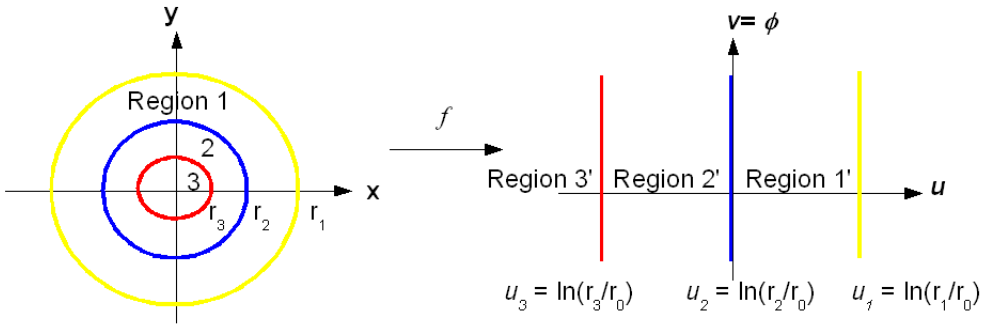


Figure 5.3: Coordinate transformation used to transform an annulus in the Cartesian coordinates (x, y, z) to planes in the new (u, v, w)coordinate system. The planes are located at $u_I = \ln(r_I/r_0)$.

annular region, where region $I = 1, 2, 3$ is defined by $r_{I-1} < r \leq r_I$. Let $\{\bar{x}^i\} = (u, v, w)$ be the curvilinear coordinates describing a set of planar region $I' = 1', 2', 3'$ defined by $u_{I'-1} < u \leq u_{I'}$. If we choose a map $f : \boldsymbol{x} \to \bar{\boldsymbol{x}}$ such that

$$x = r_0 \exp(u)\cos(v), \quad y = r_0 \exp(u)\cos(v), \quad z = w \tag{5.3}$$

we can map annular regions I to planar regions I' as shown in fig 5.3.

Let the optical material parameters in region I be denoted by $\boldsymbol{\epsilon}_I, \boldsymbol{\mu}_I$, and the electric and magnetic fields be $\mathbf{E}^I, \mathbf{H}^I$ (where the index $I = 1, 2, 3$ denotes the region). Similarly in the new coordinates let $\bar{\boldsymbol{\epsilon}}_I, \bar{\boldsymbol{\mu}}_I$, and $\bar{\mathbf{E}}^I, \bar{\mathbf{H}}^I$ correspond to the optical material parameters and fields in the equivalent region I'.

Using eqn (4.8) from transformation optics, and the map f, defined by eqn (5.3), we can map the electric and magnetic fields $\mathbf{E}^I, \mathbf{H}^I$, in region I to the equivalent electric and magnetic fields $\bar{\mathbf{E}}^I, \bar{\mathbf{H}}^I$, in region I'. If the components of $\mathbf{E}^I$ are given by $\left\{E^I_j\right\} = (E^I_x, E^I_y, E^I_z)$ and $\bar{\mathbf{E}}^I$ by $\left\{\bar{E_i}^I\right\} = (\bar{E}^I_u, \bar{E}^I_v, \bar{E}^I_w)$ (where the index i, j denotes the field orientation) then:

$$\bar{E}^I_u = x.E^I_x + y.E^I_y, \quad \bar{E}^I_v = -y.E^I_x + x.E^I_y, \quad \bar{E}^I_w = E^I_z, \tag{5.4}$$

Similarly if the permittivity and permeability in Cartesian coordinates are given by

$$\boldsymbol{\epsilon}_I = \boldsymbol{\mu}_I = \text{diag}\left[\epsilon^{(I)}_x, \epsilon^{(I)}_y, \epsilon^{(I)}_z\right] \qquad r_{I-1} < r \leq r_I \tag{5.5}$$

then using the strategy from before (section 5.2), we get the material parameters for the cylindrical SS (with physical size r_2) as:

$$\begin{array}{llll} \epsilon^{(1)}_x = +1 & \epsilon^{(1)}_y = +1 & \epsilon^{(1)}_z = +1 & r_2 \leq r \\ \epsilon^{(2)}_x = -1 & \epsilon^{(2)}_y = -1 & \epsilon^{(2)}_z = -\frac{r_2^4}{r^4} & r_3 \leq r \leq r_2 \\ \epsilon^{(3)}_x = +1 & \epsilon^{(3)}_y = +1 & \epsilon^{(3)}_z = +\frac{r_2^4}{r_3^4}\epsilon_{\text{eff}} & r \leq r_3 \end{array} \tag{5.6}$$

The effective permittivity (permeability) of the SS as seen by an incident field would be given by:

$$\boldsymbol{\epsilon}_{\text{eff}} = \text{diag}\left[1, 1, \epsilon_{\text{eff}}\right] = \text{diag}\left[1, 1, \frac{\epsilon^{(3)}_z}{\gamma^2}\right], \qquad r \leq r_1 \tag{5.7}$$

(where $\gamma = r_2^2/r_3^2$) with an apparent effective size given by r_1 - whence in the new coordinates, region $1'$ is designed to optically cancel region $2'$, this means that the width of region $1'$ is equal to the width of region $2'$ (or $u_2 - u_3 = u_1 - u_2$) so that in Cartesian coordinates this implies that

$$r_1 = \frac{r_2^2}{r_3} \tag{5.8}$$

Hence depending on what type of SS we want to design (that is what ϵ_{eff}) and what effective size of the SS we want (that is what r_1), we can use (5.6) above to design such a SS.

Now for the discussion of the later parts, we will examine the scattering of light from 3 particular types of cylindrical SS, given by 3 different ϵ_{eff}, namely the i) *transparent SS* (with $\epsilon_{\text{eff}} = 1$) ii) *absorber SS* (with $\epsilon_x^{(3)} = \epsilon_y^{(3)} = \epsilon_{\text{eff}} = 1 + i\alpha$, where $\alpha > 0$ is a measure of loss) and iii) *retro-reflector SS* (with $\epsilon_{\text{eff}} = 4$).

5.3 Methods of analyzing scattering

In this section we shall examine how electromagnetic waves interact with our cylindrical SS we have derived from section 5.2.1. We would firstly examine how the super-scatterer increases the scattering cross section by using the simple ray-optics. Following this we will show how a full wave solution can be obtained using cylindrical wave expansion.

5.3.1 Ray optics

In this section we will use a simple ray tracing technique to find out how a set of rays coming in from infinity will interact with a *transparent SS*. Again the labeling of the various regions in this discussion follows from fig 5.3.

The trajectory of a ray in free space (region 1) is given by

$$r = \frac{b}{\sin(\phi)}, \quad r \geq r_2 \tag{5.9}$$

where b is the impact parameter (r, ϕ are the usual cylindrical polar coordinates). Now since region $1'$ and $2'$ are complementary, according to PLT (fig 4.1), the symmetry of the Poynting vector implies ray trajectories in region $1'$ is a mirror reflection to that in region $2'$. Transforming the ray trajectory in region 1 (from eqn (5.9) into the new coordinates we have the following trajectory in region $1'$:

$$r_0 \exp(u) = \frac{b}{\sin(v)}, \quad u \geq u_2 \tag{5.10}$$

Invoking the reflection symmetry about the interface of region $1'$ and $2'$, this implies that the ray trajectory in region $2'$ in the new coordinate system would be:

$$r_0 \exp(2u_2 - u) = \frac{b}{\sin(v)}, \quad u_3 \leq u \leq u_2 \tag{5.11}$$

which we can then transform back to the Cartesian coordinates as:

$$\frac{r_2^2}{r} = \frac{b}{\sin(\phi)}, \quad r_3 \leq r \leq r_2 \tag{5.12}$$

the trajectories of rays in region 2.

Similarly for the inner most region, we make use of PLT again to determine the trajectories. Since following the optical cancelation, the rays from the boundaries of region $1'$ are *translated* (by $(u_1 - u_3)$) to region $3'$ (see fig 4.2(b)), we should get:

$$r_0 \exp(u_1 - u_3 + u) = \frac{b}{\sin(v)}, \quad u \leq u_3 \tag{5.13}$$

which we can then transform back to the old Cartesian coordinates as:

$$r = \frac{r_3}{r_1}.\frac{b}{\sin(\phi)} = \frac{r_3^2}{r_2^2}.\frac{b}{\sin(\phi)}, \quad r \leq r_3 \tag{5.14}$$

where we used eqn (5.8) to express the trajectory as a function of the inner and outer radii of the NRIM annulus. Now with eqn (5.9), (5.12), (5.14), we can completely describe the ray trajectories for our structure which we plot in fig 5.4(a).

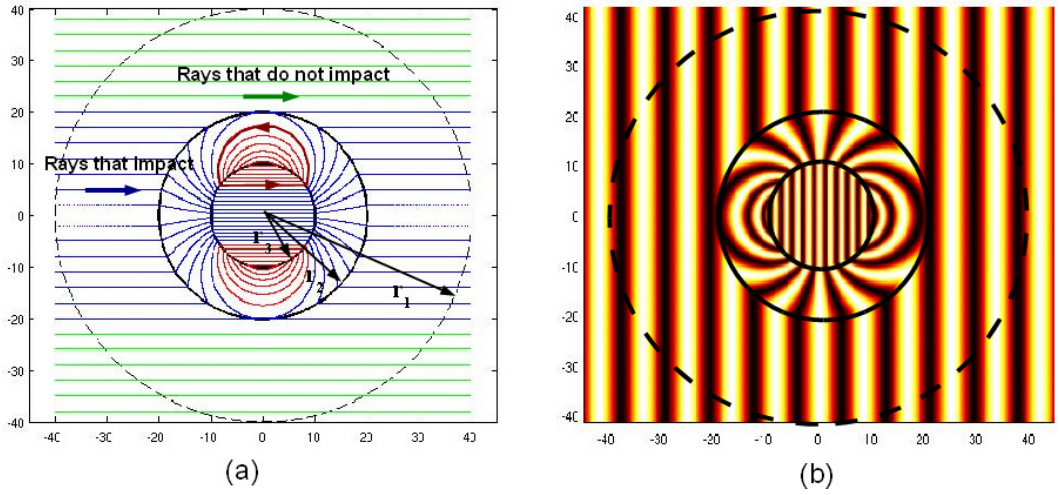


Figure 5.4: Fig (a) ray trajectories for the *transparent SS*. The black solid lines are the boundaries of the NRIM lens, while the black dashed line is the annular region of vacuum which is optically canceled by the lens. The blue lines are the set of incident rays which impacts the lens while the green lines are rays that don't. The red lines are self closed loops which are localized optical modes evanescently coupled to the green lines. Fig (b) full wave solution of the same transparent SS. Plot shows the color contour plot of field magnitude $|E_z|$ in the x, y plane.

We note from these equations, that the trajectories in all the regions are connected (or continuous) as long as $b \leq r_2$ (fig 5.4(a)) . This forms the first set of trajectories which on impact with the NRIM lens, are refracted and channeled within to the

inner core. We also note that the trajectories within the inner core are compressed by a factor of r_1/r_3 just as expected.

The second set of trajectories in region 1, are those that do not impact the NRIM and appear to escape (the green lines in fig 5.4). These trajectories belong to the same set as trajectories in region 2 and 3 which forms self closed loops (the red lines in fig 5.4). These self closed loops are localized optical modes which are evanescently coupled to the trajectories in region 1 which seems to escape. In other words this set of self closed loops are an exact replica of the second set of trajectories in region 1. This implies that if we place an object in region 3, which interacts with these self closed loops, the information of this interaction is transmitted to the rays outside in region 1 effecting a change. Conversely any changes to the ray paths in these parts of region 1 would be reflected by changes to these self closed loops. It is this unique feature which gives the SS it's 'edge' over conventional scatterers.

Now we note that the self closed loops which are larger are coupled to trajectories in region 1 which are nearer to the NRIM lens. These trajectories are more strongly coupled as they are physically nearer compared to smaller self closed loops which are coupled to trajectories further away. As such we would expect, any losses present in the NRIM to kill off these smaller self closed loops first. Eventually with sufficient amount of losses one would expect all the self closed loops to be killed off and the cylindrical perfect lens can only then capture only rays which impact on the lens itself (the blue lines in fig 5.4(a)).

We also note that this evanescent coupling is due to surface plasmon resonances on the NRIM, so it is entirely a resonance phenomenon - that is to say such a coupling takes a finite amount of time; the same amount of time as it takes to build up the resonance [92, 93]. This implies that any time varying interactions with the light rays in region 3 will take a finite amount of time to be effected in region 1, so fluctuations which are faster than the time it takes to build up the resonance is not captured by this coupling. The time it takes to establish such a resonance shall be more fully explored later in chapter 7.

5.3.2 Full wave solution

The analysis in the previous section using rays is simple enough for us to understand the reason behind why SS can have a larger scattering cross sectional area than conventional scatterers. However we cannot determine precisely how losses will affect the performance of such a scatterer. In addition we need a more general model which works not only for the transparent SS but a general class of SS. With this in mind, in order to be more precise and rigorous in our examination of electromagnetic interaction with our SS structure, we need to move beyond the ray analysis to the full wave solution of Maxwell's equations. Here we will solve the full wave problem using a method known as *transfer matrices* [94]. In the same way that we have derive the trajectories in the ray model, we need to first work out what the wave solutions are in the various regions, then match them by enforcing boundary conditions.

Now suppose an incident plane wave (in polar coordinates) of the following form impacts the SS

$$\begin{aligned} E_z^{\text{inc}} &= E_{z0}\exp(\mathrm{i}k_1 r\cos\phi - \mathrm{i}\omega t) \\ &= E_{z0}\textstyle\sum_{m=-\infty}^{m=\infty} J_m(k_1 r)\mathrm{i}^m \exp(\mathrm{i}m\phi - \mathrm{i}\omega t) \end{aligned} \tag{5.15}$$

where we assume that the electric field vector is parallel to the cylinder axis (or z-axis), and the wave vector of magnitude k_1 lies along the x-axis, and is given by

$$k_1 = \omega/c \tag{5.16}$$

In the second line of the eqn (5.15), the incident plane wave is decomposed to a sum of cylindrical waves using the Jacobi-Anger expansion [95] where J_m is a cylindrical Bessel function of order m.

Now solving for Maxwell's equations, given the above initial conditions, it can be shown that the field solutions for region 1 is given by

$$\begin{aligned} E_z^{(1)} &= E_z^{\text{inc}} + E_z^{\text{scatt}} \\ &= E_{z0}\sum_{m=-\infty}^{m=\infty}\left[J_m(k_1 r) + a_m H_m^{(1)}(k_1 r)\right]\mathrm{i}^m e^{(\mathrm{i}m\phi - \mathrm{i}\omega t)},\ r \geq r_2 \end{aligned} \tag{5.17}$$

where the first term is the incident, the second is the outgoing cylindrical waves, and $H_m^{(1)}$ is the Hankel functions of the 1st kind. Here a_m is the amplitude of

the scattered cylindrical wave. Now to determine the field solution for region 2, we can either solve Maxwell's equations in cylindrical coordinates again with the permittivity and permeability given by eqn (5.6) or a much simpler way, is to make use of the symmetries in PLT. Using the symmetries of fields (that is $\bar{\mathbf{E}}^{(2)}$ is a mirror image of $\bar{\mathbf{E}}^{(1)}$), the fields in region $2'$ is related to that in region $1'$ by

$$\bar{E}_z^{(2)}(u,v) = \bar{E}_z^{(1)}(2u_2 - u, v),\ u \leq u_2 \tag{5.18}$$

Therefore the fields in region 2 would then be given by

$$E_z^{(2)} = E_{z0} \sum_{m=-\infty}^{m=\infty} \left[b_m J_m(k_2 \left[\frac{r_2^2}{r}\right]) + c_m H_m^{(1)}(k_2 \left[\frac{r_2^2}{r}\right]) \right] \mathrm{i}^m e^{(\mathrm{i}m\phi - \mathrm{i}\omega t)},\ r_3 \leq r \leq r_2 \tag{5.19}$$

where $k_2 = k_1$, $b_m = 1$, $c_m = a_m$, in the lossless case.

To generalize to the lossy NRIM case we see that a lossy region 2 is no longer complementary to region 1 (vacuum), but is complementary to a pseudo-region 1 - that is a region 1 that has gain, where $\boldsymbol{\epsilon}^{(1)} = \boldsymbol{\mu}^{(1)} = (1 - \mathrm{i}\delta)$, $\forall r > r_2$ and $\delta > 0$ is a measure of *gain* of the PRIM in this pseudo-region 1. This implies that for a lossy NRIM the material properties becomes

$$\begin{array}{rcl} \boldsymbol{\epsilon}^{(2)}(r) & = & (1 - \mathrm{i}\delta)\boldsymbol{\epsilon}^{(2)}_{\text{ideal}}(r) \\ \boldsymbol{\mu}^{(2)}(r) & = & (1 - \mathrm{i}\delta)\boldsymbol{\mu}^{(2)}_{\text{ideal}}(r) \end{array},\ r_3 \leq r \leq r_2 \tag{5.20}$$

where $\boldsymbol{\epsilon}^{(2)}_{\text{ideal}}, \boldsymbol{\mu}^{(2)}_{\text{ideal}}$, are the ideal lossless material parameters given by eqn (5.6), and $\delta > 0$ is now a measure of *losses* in the NRIM. Using eqn (5.20), the wave-vector in Region 2 would then be given by

$$k_2 = (1 - \mathrm{i}\delta)k_1 \tag{5.21}$$

Consequently, $b_m \neq 1$, $c_m \neq a_m$ in the general lossy case.

Finally for region 3 with $\epsilon_x^{(3)} = \epsilon_y^{(3)} = 1$, $\epsilon_z^{(3)} = \frac{r_2^4}{r_3^4}\epsilon_{\text{eff}}$, ($\forall r \leq r_3$, and $\boldsymbol{\epsilon}^{(3)} = \boldsymbol{\mu}^{(3)}$)

$$E_z^{(3)} = E_{z0} \sum_{m=-\infty}^{m=\infty} [d_m J_m(k_3 r)]\, \mathrm{i}^m \exp(\mathrm{i}m\phi - \mathrm{i}wt), \quad r \leq r_3 \tag{5.22}$$

where

$$k_3 = \left(\frac{r_2}{r_3}\right)^2 \sqrt{\epsilon_x^{(3)}\epsilon_{\text{eff}}}.k_1 \tag{5.23}$$

(Note for the case of an *absorber SS* we have $\epsilon_x^{(3)} = \epsilon_y^{(3)} = \epsilon_{\text{eff}} = 1 + i\alpha$ and $\alpha > 0$ is a measure of loss). Physically d_m is the amplitude of the transmitted wave of order m.

Now with eqn (5.17), (5.19), (5.22), we have determined the general solutions of the fields in each of the regions. To have a consistent overall solution, we still need to determine the unknown scattering coefficients a_m, b_m, c_m, d_m, subjected to boundary conditions at the interfaces of the various regions. That is the tangential E and H fields must be matched and continuous across each interface:

$$\mathbf{E}_{\|}^{I}(\mathbf{r}) = \mathbf{E}_{\|}^{I+1}(\mathbf{r}), \quad I = 1, 2 \tag{5.24}$$

$$\mathbf{H}_{\|}^{I}(\mathbf{r}) = \mathbf{H}_{\|}^{I+1}(\mathbf{r}) \quad I = 1, 2 \tag{5.25}$$

where $\mathbf{E}_{\|}^{I}, \mathbf{H}_{\|}^{I}$, are the respective E and H field vectors projected onto the surface of the interface and the superscript again represents the regions that the fields are in. Using the E-field solution given by eqn (5.17), (5.19), (5.22), we can easily determine the H field vectors using Maxwell equation:

$$\nabla \times \mathbf{E} = -\boldsymbol{\mu}.\dot{\mathbf{H}} \tag{5.26}$$

Since $\mathbf{E}_{\|} = E_z\hat{\mathbf{z}}$, using eqn (5.26), we get:

$$\mathbf{E}_{\|}^{I} = E_z^I\hat{\mathbf{z}}, \tag{5.27}$$

$$\mathbf{H}_{\|}^{I} = H_\phi = \frac{-\mathrm{i}}{\mu_\phi\mu_0 w}.\frac{\partial}{\partial r}E_z^I \tag{5.28}$$

which can then be used in eqn (5.24), (5.25) to determine the scattering coefficients.

Now with the scattering coefficients a_m, b_m, c_m, d_m, and eqn (5.17), (5.19), (5.22), we can fully determine the electric field and intensity distribution of a SS in the presence of an incident plane wave. Moreover with, these scattering coefficients we can determine how each cylindrical wave component (of order m) individually would be affected by the presence of different scatterers. Of particular importance is the scattering coefficients a_m and d_m, which are linked to the reflection and transmission coefficients of the cylindrical wave mode (of order m). So when a wave of order m scatters from a scatterer, it will have $a_m \neq 0$. Similarly $|d_m|^2$ gives us a measure of the power transmitted into region 3 (for the ideal transparent SS, $|d_m|^2 = 1$).

Now if we know a_m, we can also determine the scattered field distribution at large distances away. So if we take the asymptotic limits ($r \to \infty$) of the Hankel functions in eqn (5.17), this would give us:

$$E_z^{\text{scatt}}(r \to \infty, \phi) = \left(\sqrt{\frac{2}{\pi k_1 r}}\mathrm{e}^{i(kr-\pi/4)}\right)\mathrm{g}(\phi) \tag{5.29}$$

where g(ϕ) is the angular distribution of scattered field amplitude at infinity, otherwise known as the scattering amplitude

$$\mathrm{g}(\phi) = \left[a_0 + 2 \sum_{m=1}^{\infty} a_m \cos(m\phi) \right] \tag{5.30}$$

Eqn (5.30) will be useful later when we determine the back-scattered intensity distribution ($\sim |\mathrm{g}(\pi)|^2$) of a retro-reflecting SS in section 5.4.3.

5.3.3 The localization principle

Before we make use of the tools from the previous sections to analyze the scattering of a SS, it is instructive to note that the full wave analysis from section 5.3.2 is related to the ray analysis in section 5.3.1. This connection is given by the *localization principle* [96] which states that a term of order m in the cylindrical wave expansion is related to a ray with an impact parameter $b = m/k_1$.

This can be understood when we examine the Bessel function $J_m(k_1 r)$ of the cylindrical wave expansion of a plane wave (from eqn (5.15)). We see that because

$$|J_m(k_1 r)| \approx \begin{cases} 1 & k_1 r \geq m \\ 0 & k_1 r < m \end{cases} \tag{5.31}$$

it implies that a cylindrical wave of order m, will not (normally) interact with the scatterer with dimensions d, when $d < m/k_1$, in the exact same way that a ray will not interact with a scatterer when it's impact parameter $b > d$. Another way to understand this correspondence between rays and waves is the analogy with quantum (wave) mechanics. A light ray with momentum $\hbar k_1$ and impact parameter b has an angular momentum $\hbar k_1 b$. Correspondingly a cylindrical wave of order m has an angular momentum $i\hbar\partial_\phi \psi = \hbar m$, so this means that a ray corresponds to a cylindrical wave mode $m = k_1 b$.

Now we can apply the localization principle to relate the discussion we have in ray modeling of SS with the wave model. Previously we have seen from section 5.3.1 (fig 5.4(a)) that there are two sets of rays , firstly a set of (green) rays in region 1 ($r_2 < r < r_1$), which do not impact the SS, and a second set of (blue) rays which does. The set of (green) non-impact rays, we claimed to be evanescently coupled to the internal optical modes (red rays); and we claim it is this coupling what gives the SS a scattering cross section enhancement over conventional scatterer. If

such a coupling exist, then according to the localization principle, when we examine the corresponding cylindrical wave modes of order $m_2 < m < m_1$ ($m_1 = k_1 r_1$, $m_2 = k_1 r_2$), we would find that $a_m, d_m \neq 0$ ($d_m = 1$, for an ideal lossless transparent SS). In addition, we also claim previously that increasing material losses will kill the coupling for non-impact rays which are further away (with a larger impact parameter b). Correspondingly, we would then expect that increasing losses would extinguish these cylindrical wave modes (that is scattering coefficients $a_m, d_m \to 0$), starting from modes with larger m.

5.4 Scattering of a super-scatterer

Using the machinery from the previous sections, we can now study the full wave interaction of an electromagnetic wave with our SS. In this section we will examine the electromagnetic interaction with 3 different super-scatterers - the *transparent SS*, the *absorber SS* and the *retro-reflector SS* - and through this we will demonstrate the capability of NRIM lens to enhance the scattering cross section beyond conventional optical means.

5.4.1 Transparent super-scatterer

The cylindrical *transparent SS* that we will be studying here is defined by a scatterer with material parameters given by eqn (5.6) with $\epsilon_{\text{eff}} = 1$. Such a transparent SS has an effective permittivity and permeability, $\boldsymbol{\epsilon}_{\text{eff}} = \boldsymbol{\mu}_{\text{eff}} = 1$, with an effective size $r_1 = r_2^2/r_3$ (r_2 and r_3 refers to the outer and inner radii of the NRIM annulus). Hence ideally in the absence of losses such a SS would be completely transparent to incoming electromagnetic waves. By examining how losses in the NRIM layer would affect the transparency of such a SS, we can understand the mechanism behind super-enhancement and how material losses can affect the performances of a general super-scatterer.

Using the results from the previous section, fig 5.4(b) shows a contour plot of $\Re(E_z)$ as a function of x, y, of an incident electromagnetic plane wave in the presence of an ideal lossless transparent SS. Comparing the full wave analysis in fig 5.4(b) with the ray traced results in fig 5.4(a), we can see that the rays in fig 5.4(a) are normal to the wave or phase fronts of fig 5.4(b) just as expected. We can also see that

the magnitude of the electric fields are uniform for all the regions so there is no distinction between the set of rays which impact the NRIM and the set which don't. In particular the self closed loops have the same intensity as rays which are guided in by refraction. In addition we note that the number of wave lengths in the effective volume of the SS (that is region 1, delineated by the dashed line in fig 5.4(b)) is the same as the number of wavelengths in region 3, demonstrating that region 3 is an optical equivalent of this effective volume albeit a compressed one.

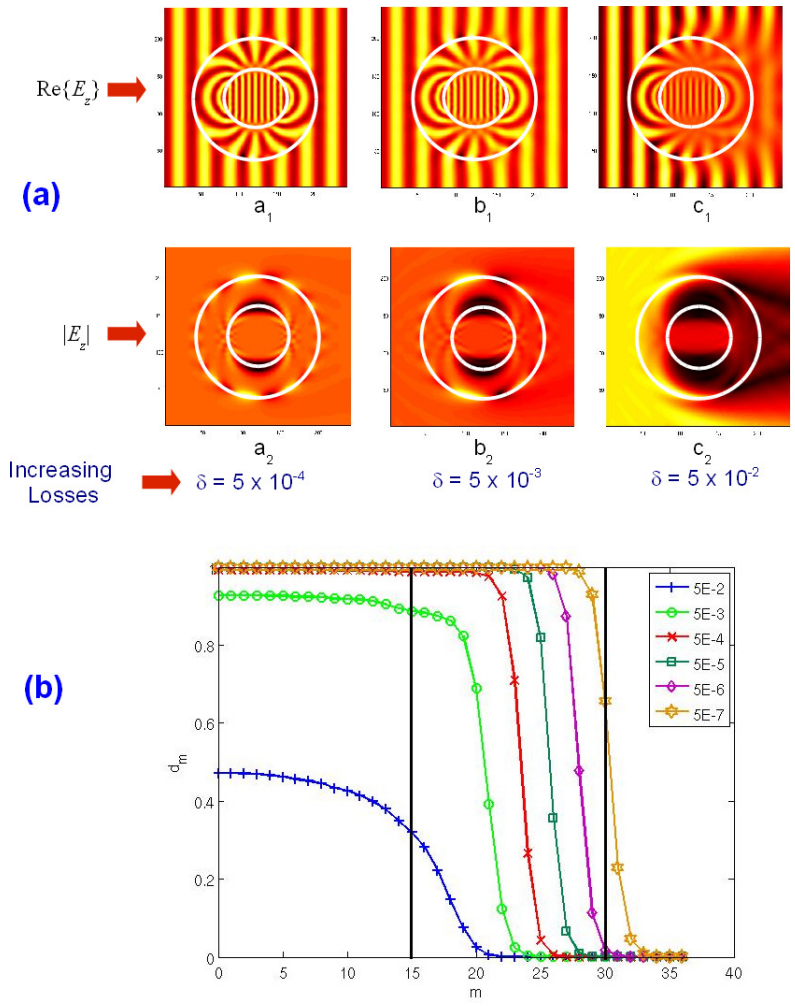


Figure 5.5: Fig (a) contour plots of E field strength $\Re(E_z)$ (a_1 to c_1), and Intensity ($|E_z|$) (a_2 to c_2) showing effects of increasing losses, for $\delta = 5\times10^{-4}, 5\times10^{-3}, 5\times10^{-2}$ respectively. Fig (b) plot of the transmitted scattering coefficient d_m as a function of the angular order m, for various loss δ in the NRIM lens ($r_2 = 20, r_3 = 10$). The two solid black lines are defines the boundaries of region 1 with $m_2 = k_1 r_2 = 15$, $m_1 = k_1 r_1 = 30$.

Fig 5.5 shows a contour plot of $\Re(E_z)$ and $|E_z|$ for various magnitude of losses in the NRIM of the transparent SS. Further to our discussion in section 5.3.1, we can see in fig 5.5(a), as we increase the amount of losses in the NRIM δ from $\delta = 5\times10^{-4}$ to $\delta = 5 \times 10^{-2}$, the E field strength in the core region decreases in extent. This effect is most acute at the edges near $y = r_3$, which as explained in section 5.3.1, is due to the killing of the coupling between the propagating modes (the green lines) in vacuum with the localized optical modes (the red lines) in the NRIM (see fig 5.4(a)).

Now applying the localization principle from section 5.3.3, we can discuss more quantitatively the effects of losses on each cylindrical wave mode (of order m), by examining the effects of losses on the scattering coefficient d_m (the transmitted field amplitude). In fig 5.5(b), we plot a graph of the transmitted field amplitude d_m in region 3 for the various orders of m. As we have seen, optical modes with $m_2 \leq m \leq m_1$ ($m_1 = k_1 r_1$ and $m_2 = k_1 r_2$) corresponds to the rays in region 1 which does not impact the SS. Now $d_m(m) = 1$ indicates that the SS can *perfectly capture* light rays with impact parameter m/k_1, while conversely $d_m(m) = 0$ indicates that the SS does not interact with the non-impact light rays at all. The effective size of the transparent SS, can thus be defined by the value of $m = m_{0.5}$ where $d_m(m_{0.5}) = 0.5$, and the effective size is $\sim m_{0.5}/k_1$. So from fig 5.5(b), for loss $\delta = 5 \times 10^{-4}$ the effective size of the SS is $r_{\text{eff}} \approx 31$ (as compared to the physical size of the entire SS which is $r = 20$). As expected we can see that increasing losses in the SS, reduce the number non-zero d_m or number of optical modes captured, thus for $\delta \lesssim 5\times10^{-2}$ only rays which impact the SS are captured.

5.4.2 Absorber SS

When region 3 of the transparent SS is lossy - that is $\epsilon_{eff} = \mu_{eff} = (1 + i\alpha)$ in eqn (5.6) (where $\alpha > 0$ is a measure of losses) - we have an *absorber SS*. Such a SS (in the absence of losses in the NRIM layer) also has an effective size $r_1 = r_2^2/r_3$ (r_2 and r_3 refers to the outer and inner radii of the NRIM annulus). Because the absorber SS is impedance matched to vacuum (since $\sqrt{\epsilon_z^{(\text{eff})}/\mu_\phi^{(\text{eff})}} = 1$), this means that such a SS has minimal reflections and maximum absorption of the incident electromagnetic waves. Ideally in the absence of losses in the NRIM, such a SS would behave like a perfect cylindrical absorber. In this section we will study the ability of this absorber

SS to cast an enhanced shadow. To avoid confusion, the losses in the core region 3 is denoted by α ($\alpha = 0.23$ in this study), while the losses in the NRIM lens is denoted by $\delta > 0$. An *ideal* absorber SS is given by a SS which has a lossless NRIM layer ($\delta = 0$).

Now from fig 5.6(A and B), we can see that an ideal absorber SS (NRIM layer with $r_3 = 10$, $r_2 = 20$) is completely electromagnetically equivalent (for $r \geq r_1$) to a larger lossy cylinder ($\alpha = 0.23$) with radius $r_1 = 40 = r_2^2/r_3$. We can see in the figure that the shadow cast by the smaller absorber SS has the same extent as the larger dielectric cylinder. Now we can examine the effect of losses in the NRIM layer of the SS, by increasing δ. As we can see from fig 5.6(B and C) as we increase δ from $\delta = 0$ to $\delta = 5 \times 10^{-3}$, the extent of the shadow cast by the NRIM structure decreases as expected.

Again we can be more precise in examining the how losses in the NRIM by looking at the relative scattering coefficient $a_m^{(r)}$ which is defined as:

$$a_m^{(r)} = \frac{a_m^{(\mathrm{SS})}}{a_m^{(\mathrm{cylinder})}} \tag{5.32}$$

where $a_m^{(\mathrm{SS})}$ is the scattering coefficient of the SS with a lossy NRIM lens (with inner and outer radius defined as r_3 and r_2 respectively), and $a_m^{(\mathrm{cylinder})}$ is the reflected scattering coefficient of the equivalent normal lossy dielectric cylinder of radius $r_1 = r_2^2/r_3$. Fig 5.7(a) is the graph of $a_m^{(r)}$ as a function of the order m, for a NRIM lens with $r_3 = 10$ and $r_2 = 20$. The relative scattering coefficient is plotted for various amount of losses in the NRIM given by loss tangent δ, ranging from $\delta = 0$ to $\delta = 5 \times 10^{-2}$. In the similar manner as the previous section, $a_m^{(r)} = 1$ indicates that the SS scatters an optical mode of order m in the same way as a normal lossy cylinder. Conversely when $a_m^{(r)} = 0$ it indicates that the optical mode of order m does not interact with the SS. Unlike the previous section $a_m^{(r)}$ can be greater than 1, and that just implies that the SS does not scatter the optical mode m in the same way as a lossy cylinder does. Similar to the previous section the effective size of the SS (or size of shadow cast), is approximately determined by the value of $m = m_{0.5}$ where $a_m^{(r)}(m_{0.5}) = 0.5$, so the effective extent of shadow cast is $\sim m_{0.5}/k_1$. So for loss $\delta = 5 \times 10^{-4}$ the effective size of the SS is $r_{\mathrm{eff}} \approx 28.7$ (whilst the physical size of the SS is $r_2 = 20$). A complete electromagnetic equivalence between an ideal

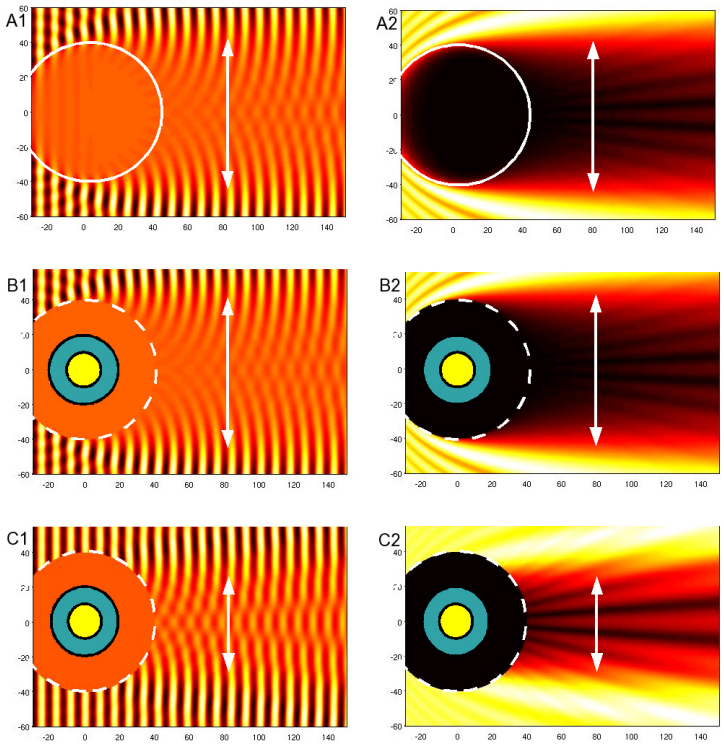


Figure 5.6: Contour plot of field strength $\Re[E_z]$ (fig A_1 to C_1) and field magnitude $|E_z|$ (fig A_2 to C_2). The solid lines denotes the physical boundaries, while the dashed line denotes the effective size of the ideal lossless SS ($r_1 = 40$). Fig (A_1 and A_2) are the contour plots for a normal lossy cylinder ($\alpha = 0.23$), of radius $r_1 = 40$. Fig (B_1 and B_2) shows the extent of shadow cast by the ideal absorber SS and fig (C_1 and C_2) for a lossy absorber SS ($\delta = 5 \times 10^{-3}$). For fig (B to C) the field for $r \leq r_1$ have been filtered out, as the field in this region diverges very rapidly which would saturate the color plots.

absorber SS as compared to the lossy cylinder can be seen by $a_m^{(r)} = 1, \forall m$ which can be seen in the $\delta = 0$ curve. With increased amount of losses the number of non-zero $a_m^{(r)}$ terms for $m_2 \leq m \leq m_1$ decreases, showing once again that the losses in the NRIM layer diminishes the ability of the SS to cast an bigger shadow. Again we can see from fig 5.7(a) that for $\delta = \delta_c \gtrsim 5 \times 10^{-2}$ the lossy Absorber SS will only cast a shadow as big as the physical dimension of the SS ($r = r_2$), which is expected. Note once again that this critical loss δ_c, is consistent with the results from the previous section.

Now we can also intuitively guess that as the amount of lossy NRIM material

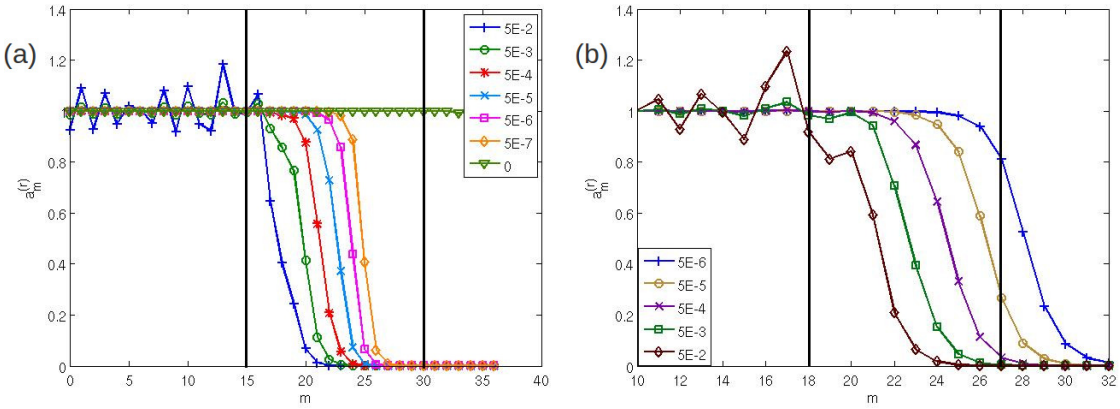


Figure 5.7: Figure of the relative reflected scattering coefficient $a_m^{(r)}$ as a function of the order m of the Bessel functions, for increasing amount of loss tangent δ in the NRIM lens. The two solid black lines define the boundaries of region 1. Fig (a) is the scattering results, for a SS with outer and inner radii $r_2 = 20$, $r_3 = 10$ and fig (b) is for a SS with $r_2 = 15$, and $r_3 = 10$.

decreases, the absorber SS would also be less sensitive to losses. This is seen in fig 5.7(b) where the outer radius of the NRIM is now reduced to $r_2 = 15$. We can see that even when we have losses at $\delta_c = 5 \times 10^{-1}$ the lens can still capture light rays which does not impact the lens.

5.4.3 Retro-reflector SS

5.4.3.1 Principles of retro-reflection

A retro-reflector is a scatterer which has a strong directed back-scatter (backward reflection) so that a significant portion of the incident plane wave is reflected backwards in the exact opposite direction. The quality of a retro-reflector is measured by the magnitude of the back-scattered intensity and the how angularly divergent the back-scattered radiation is. The higher the back-scattered intensity and the narrower the back-scattered beam, the better the retro-reflector is. Now a mirror for instance can be considered as a retro-reflector, but only when the incident plane wave is normal to the mirror. All retro-reflectors have an angle of acceptance - that is a range of incident angles such that the incident plane wave can be retro-reflected backwards. So in the case of a mirror the angle of acceptance is zero, while a corner cube (2 perpendicular mirrors) has an angle of incidence $\approx \pm 45^0$. An *all-angle retro-reflector*

is a retro-reflector which has a full 360^0 (or $\pm 180^0$) angle of acceptance.

Now it can be shown that a cylinder with refractive index $n = 2$[2] behaves like such an all angle retro-reflector [97]. The principle of operation is based on that of a backward (primary) rainbow. It can be shown from geometrical optics (ray tracing) [70] that when the refractive index of the cylinder $n = 2$, the position of the rainbow caustics lies directly in the opposite direction to that of the incident light rays. That is a bundle of incident rays with (close to) zero impact parameters, are reflected backwards from the back surface of the cylinder.

Such a retro-reflector has a number of properties which is useful for our discussion later. Firstly the back-scattered field magnitude $|E|_\infty$ (at $r \to \infty$, $\phi = \pi$) should increase monotonically with the radius, d, of the retro-reflecting cylinder, so larger retro-reflectors have better retro-reflection. If geometrical optics applies (for sufficiently large d), we would expect the back-scattered field magnitude , $|E|_\infty$ (at $r \to \infty$, $\phi = \pi$), to be approximately linearly proportional to d. This is because the incident flux (of rays that will be back-scattered) is linearly proportional to d, and the angle of divergence of the retro-reflected rays is inversely proportional to d (for sufficiently large d). So the combined effect is that the intensity of the back-scattered wave I_∞ (at $r \to \infty$, $\phi = \pi$) is proportional to d^2. For the range of d in this report, more accurate numerical result shows $I_\infty \propto d^{1.5}$ and $|E|_\infty \propto d^{0.73}$.

Secondly the magnitude of the of the back-scattered field $|E|_\infty$ is also dependent on the interference effects between the light rays reflected from the front and the back of the cylinder. This means that when we plot $|E|_\infty$ as a function of d , other than the overall monotonic dependence on d, we will also get oscillations (with spatial frequency $2k_1$) due to the constructive and destructive interference of these rays (see fig 5.8(a)) Here $\langle |E|_\infty \rangle$ refers to the *average* back-scattered field magnitude with oscillations due to interference effect averaged out.

Finally because only the bundle of rays with (close to) zero impact parameters are eventually retro-reflected, this implies from the localization principle only cylindrical wave modes with low orders of $m \sim 0$ are important in retro-reflection.

[2]It is also important that the cylinder is impedance mismatched to allow for reflections

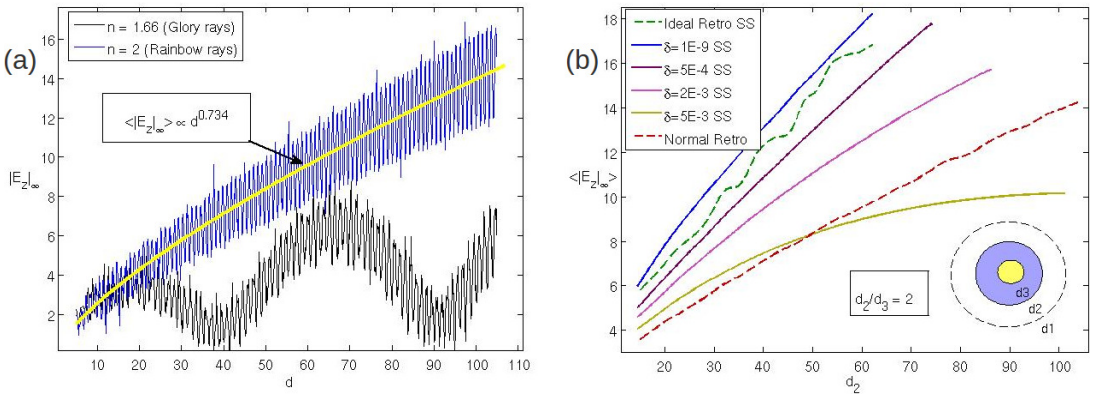


Figure 5.8: Fig (a) is a plot of the back-scattered field magnitude at infinity $|E|_\infty$, as a function of the radius d of a dielectric cylinder with refractive index $n = 2$ (blue curve) and $n = 1.6$ (black curve) respectively. The cylinder with $n = 2$ behaves like a retro-reflector and $\langle |E|_\infty \rangle \propto d^{0.73}$. Fig (b) is a plot of $\langle |E|_\infty \rangle$ as a function of the radius d_2 of the various scattering cylinder where the oscillations due to interference is filtered out. The green dashed curve is the scattering due to an ideal lossless retro-reflecting SS, while the red dashed curve is due to an ordinary retro-reflecting cylinder of the same physical size. All other curves are for the lossy SS. Figure inset shows the structure of the SS.

5.4.3.2 Results

When region 3 of the SS with radius d_2, has material parameters given by eqn (5.6) with $\epsilon_{\text{eff}} = 4$, $\mu_{\text{eff}} = 1$, then the SS has an effective refractive index of $n_{eff} = 2$. Such a SS will become a retro-reflecting cylinder with a physical radius d_2 but an effective size $d_1 = d_2^2/d_3$ (d_2 and d_3 are the outer and inner radius of the NRIM annulus), and this we will refer to as a *retro-reflector SS* (RR SS) (fig 5.9)

Now since we know from section 5.4.3.1, that any retro-reflecting cylinder has an averaged back-scattered field magnitude, that scales monotonically with the radius of the cylinder ($\langle |E|_\infty \rangle \propto d^{0.73}$), an ideal lossless RR SS, would give an averaged back-scattered intensity $\langle I_\infty \rangle$ that is approximately $(d_2/d_3)^{1.5}$ larger than a normal retro-reflecting cylinder of the same radius.

Using the results from section 5.3.2 (or eqn (5.29)) we can plot a graph of $\langle |E|_\infty \rangle$ as a function of d_2 (fig 5.8(b)) for the ideal loss-less RR SS (with $d_2/d_3 = 2$) and show it's superiority as compared to an ordinary retro-reflecting cylinder of the same

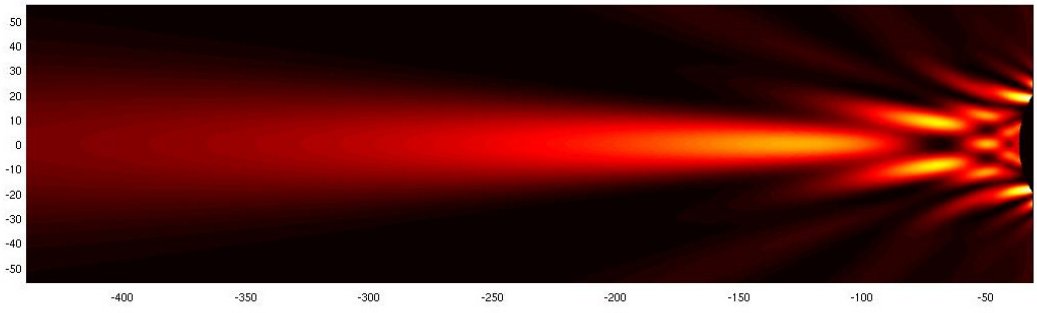


Figure 5.9: Contour plot of $|E_z(r,\phi)|$ showing the retro-reflection of a retro-reflecting SS (with $d_3 = 12.35$, $d_2 = 21.525$) which has an effective size of $d_1 = d_2^2/d_3 = 37.5$. This scattering pattern is exactly equivalent to a normal retro-reflector with a radius 37.5.

physical size. The effective size of the (ideal/lossy) RR SS is defined as the size of a normal retro-reflecting cylinder which would give the same field magnitude $\langle |E|_\infty \rangle$ as that of the (ideal/lossy) RR SS. As can be seen from fig 5.8(b), an ideal RR SS has an effective size $d_1 = d_2^2/d_3$ (for all values of d_2). Intuitively we would expect losses in the NRIM layer to degrade the performance of the RR SS, so for a lossy RR SS with $\delta = 5 \times 10^{-4}$ the effective size of the RR SS (with $d_2 = 20$, and an effective radius $d_1 = 40$) is reduced to $d_1 = 35$. Indeed we would expect further losses would eventually degrade the performance of the RR SS. However this is not always the case that losses would degrade performance. As shown in fig 5.8(b), small amount of losses in the NRIM (loss tangent $\delta = 10^{-9}$) actually *enhances* the retro-reflection instead! So for a lossy RR SS with $\delta = 1 \times 10^{-9}$ the effective size of the RR SS (with $d_2 = 20$) is approximately $d_1 = 47$, which is even larger than the effective size of an ideal RR SS ($d_1 = 40$)!

Now we can see this more explicitly by considering the *gain,* $G(\phi)$, of a scatterer - defined to be the ratio of the scattered intensity of a scatterer as compared to an isotropic scatterer (at $r \to \infty$). Using eqn (5.30) and this definition of gain, we can plot a graph of $G(\phi)$ as shown in fig 5.10. We can see that a PEC cylinder has a gain $G_{PEC} \approx 1$ while a normal retro-reflecting cylinder which has gain that scales monotonically as d_2 outperforms a PEC. In turn, it can be seen that the ideal RR SS has a gain $(d_2/d_3)^{1.5}$ times better than a normal retro-reflecting cylinder of the

same size. Once again it is remarkable and counter-intuitive to note that when we have a small amount of loss, the lossy RR SS, has a gain that scales even better than the ideal case. Of course there is no magic and as expected further increase in losses would eventually degrade the performance of the RR SS, as can be seen in the reduction in gain in fig 5.10. Now we can be more quantitative about the effects of

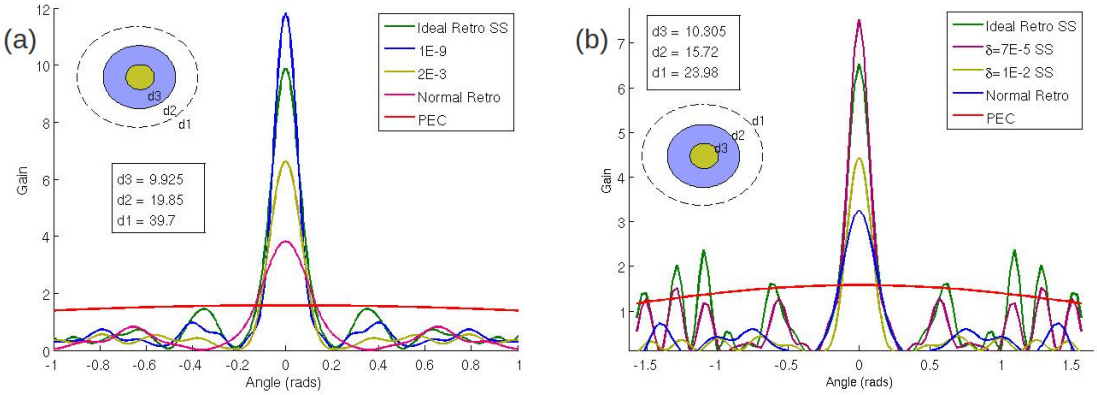


Figure 5.10: Gain as a function of back-scattered angle where 0 rads is the exact opposite direction to the incoming plane wave for various scatterers. Fig (a) shows the gain for a RR SS with $d_2/d_3 = 2$, where a loss $\delta = 1 \times 10^{-9}$ RR SS has the best gain. Similarly fig (b) is for a RR SS with $d_2/d_3 = 1.5$, where a loss $\delta = 7 \times 10^{-5}$ RR SS has the best gain.

losses when we plot a graph of the back-scattered Intensity $I_\infty(r \to \infty, \phi = \pi)$ (or equivalently gain) as a function of loss δ in the NRIM (fig 5.11). We can clearly see that for loss $\delta \lesssim 10^{-4}$ a lossy RR SS has an I_∞ equal to or *greater than* the ideal RR SS. As losses increases beyond $\delta \gtrsim 10^{-4}$, the gain of the lossy RR SS falls below the ideal RR SS, and for loss $\delta \gtrsim 10^{-2}$, the lossy RR SS would eventually lose it's enhanced retro-reflection completely.

As can be seen from these results, the RR SS is more robust to loss than the absorber SS in section 5.4.2, where the extent of shadow cast for the latter is always decreasing with increasing losses. In addition, if we compare the performance of an absorber SS with a RR SS with approximately the same structure (d_2 and d_3) and loss $\delta = 5 \times 10^{-4}$, a lossy Absorber SS has a reduced effective radius $\approx 1.4 d_2$ while a lossy RR SS has a larger effective radius $\approx 1.7 d_2$ (an ideal SS has an effective radius $2d_2$). This robustness to loss for a RR SS can be partially understood in the following way. Firstly retro-reflection relys only on rays with low impact parameters (or optical

modes with small m). Secondly from geometrical optics, the retro-reflection is strictly a result of reflection of these rays from the back surface of the retro-reflecting cylinder. This means that only paraxial or $m \approx 0$ modes are involved, higher order m modes are transmitted through the cylinder. As we can see from fig 5.5(b) and fig 5.7 and discussion from the previous sections, losses in the NRIM layer would kill off rays/modes with higher order m first leaving the lower order m modes otherwise unaffected, so this explains why the RR SS is more robust to loss. In addition losses in the NRIM layer improves this back reflection, by making the back surface of the retro-reflecting cylinder more reflective, hence a slightly lossy RR SS can capture more slightly higher order m modes that would otherwise be transmitted through. This explains why for losses less than some critical value, a lossy RR SS retro-reflects better than an ideal RR SS.

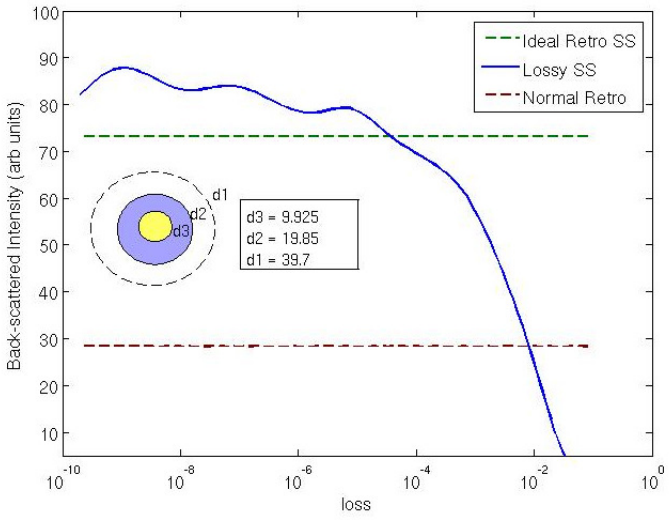


Figure 5.11: Graph of back-scattered intensity $I_\infty(r \to \infty, \phi = \pi)$ as a function of loss δ in the NRIM. The structure of the RR SS is given inset with $d_2/d_3 = 2$. The green dashed line is I_∞ for the ideal RR SS while the red dashed line is I_∞ for an ordinary retro-reflecting cylinder of the same radius.

5.5 Concluding remarks

Using PLT and transformation optics, we have shown how we can design and construct CPL, through which we can enhance the scattering properties of normal scat-

terers beyond conventional (geometrical) optics. This combination of the CPL and the embedded scatterer is what we call the *super-scatterer* (SS). In particular, we examine 3 types of SS, and show the scattering enhancement in comparison to their conventional counterparts - small objects can cast big shadows and so on.

Although these 3 particular types of SS are not exhaustive, they illustrate the potential of SS. Namely that we have a means to create compact devices much smaller than their physical sizes, *without* altering the scattering properties of the devices which we want to compactify. Further, when this compactification is of sufficient degree, can form a bridge between geometrical and wave optics. Thus we are now free to imagine subwavelength objects/devices which operate in the regime of geometrical optics - a type of *sub-wavelength* hyperlens [3].

Apart from illustrative purposes, these 3 simple types of SS, also serve as protoypes of more complicated devices. The transparent SS, can map an internal space, including objects embedded within, to a much larger external space - essentially acting as a compact magnifying glass. This we shall see in the next chapter can be used to create *super phase arrays*. The absorber SS is the simplest model of a measuring/absorbing device, where we hope to maximise the capture of light with little scattering. This for instance is a prototype of solar absorbers and so on. Finally the retro-reflector SS, is the peculiar class of scatterers where *most* incident radiation is sent backwards. This for instance may have applications in remote sensing/detection.

As a final note, while the potential for such SS are many, the challenges are not small as well. In particular, we note that losses play a crucial (detrimental) role in the performances of these SS. While we have demonstrated that a small level of loss do not destroy the SS effect, they do diminish and eventually destroy it. The challenge then is how to manage and reduce losses in the CPL. This we shall further explore in chapter 8.

[3] Note hyper-lenses are based on hyperbolic dispersion [88–90], though they too form a bridge between subwavelength objects *embedded within*, the lenses themselves are still many wavelengths in size. In contrast, a superlens of *sufficient* magnification power, can form a bridge, while maintaining subwavelength in size - an overall *sub-wavelength* type of Hyperlens.

6. Applications of the compact perfect lens II

In the previous chapter we have seen how a CPL combined with a scatterer enhances the scattering property of the scatterer, giving us a *super*-scatterer. Here in this chapter we shall consider a related problem. What happens when we combine a CPL with transmitters, in particular with a phase array, to get a *super phase array* (SPA).

At first sight, this seems to be a trivial extension of the prior chapter. However we shall see that there are some subtle but serious mathematical/physical difficulties that we need to address. Namely that the symmetries of fields due to PLT, crucial in the analysis of the previous chapter, only holds in the absence of transmitting sources. Here we shall illustrate how we can get around this mathematically and think about the implications physically.

Similar to the previous chapter, this chapter shall be broadly divided into 3 parts. First we shall discuss what are super phase arrays, how they are constructed and what can they be used for (section 6.1 and 6.2). Next we will discuss the analytical methods to study them, in particular we shall discuss about the problem and resolution of sources in PLT (section 6.3). Finally we shall examine see how the presence of CPL enhances the transmission properties of these SPA (section 6.4), and conclude this chapter with some remarks about applications (section 6.5).

6.1 What are super phase arrays?

A phase array is a group of transmitters in which the relative phases of the respective signals feeding the transmitters are varied in such a way that the effective radiation

pattern of the array is reinforced in a desired direction and suppressed in other undesired directions. The phase array has a long history, and was first developed by Karl Ferdinand Braun in 1905, when he demonstrated that a phase array has an enhanced transmission of radio waves in one direction. By varying the relative phases of the phase array antennas, one can also electronically steer (without any mechanical moving parts) a radiating beam rapidly in a desired direction. This was exploited by Luis Alvarez, during the world war II, when he used a phase array antenna to create a rapidly-steerable radar system to aid landing of airplanes in England. Due to its versatility and simplicity, even now, the phase array has a diverse variety of modern millitary, commercial, and research applications.

The principle of the phase array antenna comes from the Huygens principle [2], where an advancing wave front can be regarded as a sum of contributions from an infinite set of radiating points preceding the wavefront. This means that if we have an infinite extent of transmitters spaced at sub-wavelength intervals and if we can adjust the phase and amplitude of each transmitter, we can in principle recreate any wavefront. In practice we can relax the condition of an infinite extent of radiating transmitters, but the cost of having a finite extent of transmitters is the loss of directivity. In general, the larger the extent (aperture size) of the transmitters, the greater the directivity, hence a compromise between the physical extent and the directivity of a phase array.

In the previous chapter, we have demonstrated how super-scatterers (SS) have a scattering cross section much larger than the physical dimension of the scatterer. Here we hope to extend the ideas introduced in the previous chapter, to create a super phase array (SPA) - a phase array which is more compact than any conventional phase array yet without the loss of directivity (see fig 6.1) .

6.2 SPA and beam-forming

6.2.1 Phase array + transparent SS = SPA

As we have seen, a *transparent super-scatterer* (transparent SS) (section 5.4.1), is a scatterer which compactifies a region of transparent space[1] to a smaller region within

[1]This region may or may not be surrounding the transparent SS

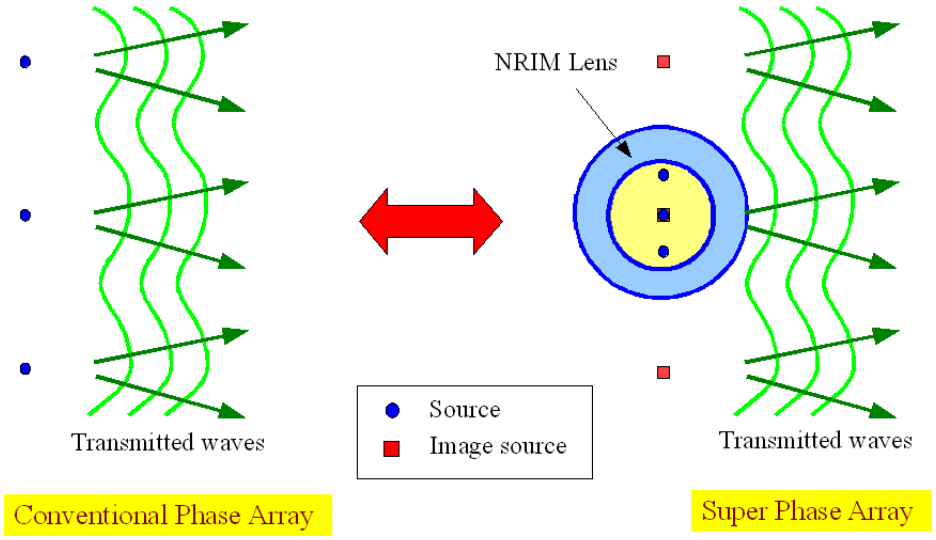


Figure 6.1: A conventional phase array can in principle recreate any wavefront when each transmitter of the array is radiating at the right amplitude and phase. A smaller super phase array can emulate a physically larger conventional phase array by amplifying the evanescent optical modes.

the scatterer. Conversely, this implies that any object (scatterers/transmitters) placed within the transparent SS would appear larger by the degree of compaction. If we now embed a conventional phase array in a transparent SS, we would get a super phase array (SPA) (see fig 6.1). To illustrate the principles we will focus only on specific case of the cylindrically symmetric transparent SS in this paper. We can easily generalise this to other geometry by using transformation optics (section 4.2). The permittivity and permeability ($\boldsymbol{\epsilon}$ and $\boldsymbol{\mu}$ respectively) for a cylindrical transparent SS is given by eqn (5.6) with $\epsilon_{\text{eff}} = 1$. As discussed previously, a transparent SS then behaves like a magnifying glass - a *superlens* [18, 23, 91, 98] - such that objects within are magnified by a factor of $r_1/r_3 = r_2^2/r_3^2$. What is remarkable is that any object with a radius larger than r_3^2/r_2 would cast an image larger than the physical size of the lens ($> r_2$), something which cannot be achieved via conventional lens. Now this implies, if we embed a phase array within such a lens, the array would be magnified by this factor. In addition if the embedded array has a size larger than r_3^2/r_2, then the image of the array would appear bigger than the physical size of the setup.

6.2.2 N-array and beam-forming

Now we shall briefly discuss how phase arrays in general transmit radiation of a desired pattern - beam forming. By varying the amplitude and the phase of the input for each transmitter in the phase array, we can reshape the transmitted wavefront in any manner we desire. In this chapter we will explore two specific examples of such beam forming using the super phase array - beam steering and beam focusing.

Firstly consider a linear phase array with N evenly distributed transmitters (let N be an odd number). Let each transmitter be labeled $n = 1$ to N, and let each transmitter be separated by a distance r_0. We note that for the phase array to work $r_0 < \lambda$ where λ is the wavelength of the transmitted wave in the medium that the phase array is embedded in. Transmitters that are spaced larger than the wavelength apart will interfere non-trivially in the far-field.

Suppose the linear array lies along the x axis, with the center of the array ($n = (N-1)/2$) at the origin ($x = y = 0$). If we want to recreate a wavefront which has the following field amplitude $\Psi(x, y)\exp(-i\omega t)$ (propagating in the y direction), we can do so when the signal input for the n^{th} transmitter is given by

$$\Psi_n = \int \Psi(x, y = 0).\delta(x - n.r_0)\,\mathrm{dx} \tag{6.1}$$

For simplicity in this report we would assume $|\Psi_n| = 1$. Now we can add a further refinement to the phase array when we allow the signal input, $\tilde{I}_n$, for the n^{th} transmitter in the array to be given by

$$\tilde{I}_n = \left[A_n.\exp(-\mathrm{i}\phi_n)\right].\Psi_n \tag{6.2}$$

where A_n is the aperture function is a real function while ϕ_n dictates the additional phase to be added to the transmitted wave. To suppress side-lobes due to a finite extent of the array, we need to choose an aperture function with a smoother cut-off. For this reason, we choose the following aperture function with a Gaussian envelope

$$A_n = \exp\left[-\left(\frac{(n-(N-1)/2).r_0}{w_0}\right)^2\right] \tag{6.3}$$

where the Gaussian envelope is centered at $(N-1)/2$ transmitter and w_0 is the width of the Gaussian envelope. Here in this report, we choose $w_0 = (N-1)/2.r_0$.

Now by applying a linear phase delay to each transmitter in the phase array (assuming the transmitters are equally spaced), we can tilt a wavefront whilst preserving

its shape. That is if ϕ_n is given by

$$\phi_n = k.n.r_0 \sin(\alpha) \tag{6.4}$$

where k is the wave vector of the transmitted wave in the medium that the array is embedded in, then the wavefront can be tilted by an angle α (where $\alpha = 0$ lies in the perpendicular direction to the linear phase array) - thus achieving beam steering.

Now other than beam steering, we can demonstrate beam focusing by applying a parabolic phase shift to the array, such that if ϕ_n is given by

$$\phi_n = k\left[\sqrt{\left((n-(N-1)/2).r_0\right)^2 + f^2} - f^2\right] \tag{6.5}$$

where f is the distance from the center of the array that the beam would focus at. For $f \gg N.r_0$ the phase ϕ_n from eqn (6.5) can be simplified as

$$\phi_n \approx \frac{k}{2f}.\left((n-(N-1)/2).r_0\right)^2 \tag{6.6}$$

When we substitute eqn (6.3), (6.6) into eqn (6.2), the resulting beam profile compares closely with the initial value of the theoretical 2-D gaussian beam, and the resultant wave propagation problem can be compared with the theoretical 2-D gaussian beam propagation. In section 6.4 of the paper, we shall demonstrate the use of the super phase array to beam steer and beam focus.

6.3 Analytical model

Now having seen from section 6.2, how to create a SPA, and having briefly discussed how we can achieve beam forming with a suitable input to the phase array, here we shall discuss about the analytical methods that we use to model such a super phase array.

6.3.1 Addition theorem

First, to model the radiation from a transmitting phase array embedded in a cylindrically symmetric transparent SS, it is wise to decompose the transmitted wave into a series of cylindrical waves (which respects the cylindrical symmetry of the lens). Initially this may seem to be a futile task since a linear phase array clearly breaks the cylindrical symmetry of the problem. This however can be circumvented when we

make use of the *addition theorem* [95] to displace the non-centric transmitters to the origin, thus restoring cylindrical symmetry of the problem. Another very important reason for using the addition theorem to move the sources to the center, is to create a source-less region ($\forall r \neq 0$) and thus make use of the field symmetries afforded by PLT (section 4.3) to obtain field solutions within the lens. Thus, by displacing or re-locating all the transmitting sources to the origin we can then make use of the result from section 5.3.2, to determine the exact field solutions of a super phase array.

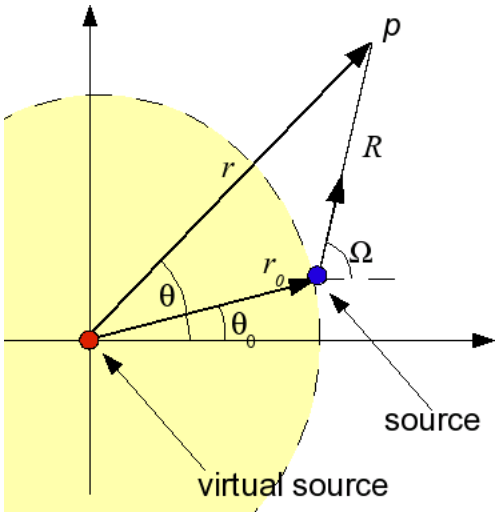


Figure 6.2: Illustration of the addition theorem. We can create the fields of a displaced source by placing an infinite series of virtual sources at the origin.

Now, suppose if we have a point source with angular coordinates (r_0, θ_0), which emits cylindrical waves of angular order ν (Hankel function of the 1st kind of order ν). According to the addition theorem, we can recreate the displaced point source, by placing an infinite number of point sources (with all angular orders) at $r = 0$ (see fig 6.2) given by

$$H_{\nu}^{(1)}(kR).e^{\mathrm{i}\nu(\Omega-\theta_0)} = \sum_{m=-\infty}^{\infty} J_m(kr_0)H_{\nu+m}^{(1)}(kr).e^{\mathrm{i}(\nu+m)(\theta-\theta_0)} \; r > r_0 \qquad (6.7)$$

where the left hand side of eqn (6.7) is the outgoing cylindrical wave centered at (r_0, θ_0)), and the right hand side is the outgoing wave for an infinite series of sources (of all angular orders) centered at the origin, weighted by some bessel function $J_m(kr_0)$.

In this report we shall assume the sources in the phase array to be a simple dipoles aligned along the axial direction, so all the transmitting sources have angular

order $\nu = 0$. Now we note that the field for a single displaced source (at (r_0, θ_0)) or an infinite series of sources located at the origin are exactly identical for $r > r_0$, but for the later the field diverges for $r < r_0$. This has some physical implications for the superlens, in that the (perfect) image of this divergent region is also (anomalously) divergent, even though the region of space where the image sits on does not contain any divergent sources. This poses a problem since such an unphysical situtation is impossible, it therefore implies that a superlens cannot exist in the first place [99]. Fortunately this problem can be resolved and we shall address this problem later in section 6.3.3.

6.3.2 Transfer matrices

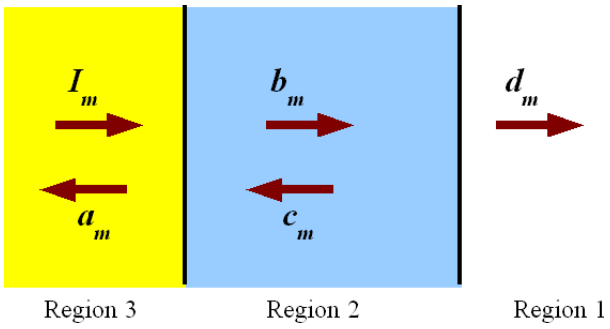


Figure 6.3: By matching boundary conditions at the interface, we can determine the field amplitudes for each cylindrical wave mode of order m.

The analysis of the SPA follows largely from the previous chapter (section 5.3.2), using the method of transfer matrices [94], so we shall not go too deeply into the details. The only difference is in the field solutions. The solution for the electric field vector is given by $E_z^{(I)}(r, \phi)$, where the superscript denotes the region, according to the definition from before (section 5.2.1; fig 5.3). The field solutions for the various regions in the transparent SS are then given by the following:

$$E_z^{(1)} = E_{z0} \sum_{m=-\infty}^{m=\infty} \left[d_m H_m^{(1)}(k_1 r) \right] \mathrm{i}^m e^{(\mathrm{i}m\phi - \mathrm{i}\omega t)}, \quad r \geq r_2 \tag{6.8}$$

$$E_z^{(2)} = E_{z0} \sum_{m=-\infty}^{m=\infty} \left[b_m H_m^{(1)}(k_2 \left[\frac{r_2^2}{r} \right]) + c_m J_m(k_2 \left[\frac{r_2^2}{r} \right]) \right] \mathrm{i}^m e^{(\mathrm{i}m\phi - \mathrm{i}\omega t)}, \; r_3 \leq r \leq r_2 \tag{6.9}$$

$$E_z^{(3)} = E_{z0} \sum_{m=-\infty}^{m=\infty} \left[I_m H_m^{(1)}(k_3 r) + a_m J_m(k_3 r) \right] \mathrm{i}^m e^{(\mathrm{i}m\phi - \mathrm{i}\omega t)}, \quad r \leq r_3 \tag{6.10}$$

With the following wave vectors in the various regions given by:

$$\begin{aligned} k_1 &= \omega/c \\ k_2 &= (1 - \mathrm{i}\delta)k_1 \\ k_3 &= \left(\frac{r_2}{r_3}\right)^2 k_1 \end{aligned} \tag{6.11}$$

where δ is the loss tangent - a measure of losses in the NRIM layer of the transparent SS.

I_m, b_m, d_m and a_m, c_m of eqn (6.8)-(6.10) are the *scattering coefficients* of the outgoing and incoming the cylindrical waves respectively. Except for I_m, all the other coefficients are unknown and when they are determined, would give the exact field solution to the problem. The coefficient I_m is dependent on the configuration and the signal input of the phase array. Using the addition theorem from eqn (6.7), we can shift all the transmitters to the origin. Together with the signal input $\tilde{I}_n$ (from eqn (6.2)) for the n^{th} transmitter of the array, this would give us:

$$I_m = \sum_{n=0}^{N} \tilde{I}_n J_m(k_3 r_n) \exp(\mathrm{i}m\theta_n) \tag{6.12}$$

where (r_n, θ_n) are the position vectors of the n^{th} transmitter. For our particular configuration - the linear phase array - these are given by

$$r_n = \left(n - \frac{(N-1)}{2}\right).r_0 \tag{6.13}$$

$$\theta_n = \left(1 - \Theta\left(n - \frac{(N-1)}{2}\right)\right).\pi \tag{6.14}$$

Now we can determine the remaining 4 unknown scattering coefficients by matching boundary conditions at the interface of each region (see fig 6.3), namely that the tangential E and H field vectors projected onto the surface of the interface has to be continuous, as we did before in section 5.3.2 (eqn (5.24)-(5.28)). These coefficients are calculated explicitly and can be referred to in appendix A.4 (eqn (A.10)).

6.3.3 Resolving divergences

The PLT (section 4.1.1) tells us that the fields within a medium (say PRIM) is a mirror image (in some planar coordinates) to its complementary (say NRIM). This means that if we know what the field solution is like for a PRIM, we can immediately write down the field solution for its complementary by reflection. Now the perfect

lens theorem only holds true when there are no sources in between the two media. If we have any sources between, we need to translate these sources (for instance via the addition theorem from section 6.3.1) outside the region of interest before we can apply the perfect lens theorem. Thus when we have a non-centric source in a cylindrical perfect lens, we need to relocate the source to the orgin in order to determine the fields in the NRIM layer. This relocation according to the addition theorem would create a virtual region of divergent fields and this virtual region would in turn cast a divergent image as illustrated in fig 6.4(a). This divergence in the image region now

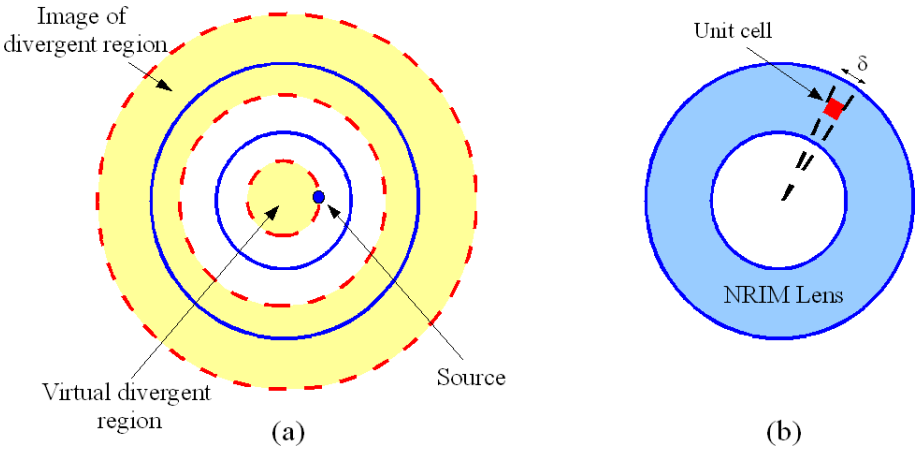


Figure 6.4: Fig (a) illustrates the problem of field divergence for a perfectly homogenous perfect lens. This problem of divergence can be accounted for since all real materials have losses or have a finite length scale where homogenity of the NRIM breaks down as shown in fig (b)

is not merely a numerical construct, but physically present, implying that it is not physically possible for a homogeneous NRIM to exist in the first place. In a similar argument others have disputed the existence of a homogeneous NRIM based on this divergence [99]. It should also be noted that the exact solution for the asymptotic behaviour of these divergences are discussed in [86, 100].

Now this apparent paradox, however, can be accounted for by limiting the divergence in eqn (6.7) through 1) imposing a higher angular momentum cutoff 2) imposing losses in the NRIM 3) considering a finite time interval in the measurement of fields. Firstly the source of the divergence is due to the higher angular order terms in eqn (6.7). These terms, however, do not contribute to the divergence in the image region because:

1. Higher angular momentum cutoff - All real materials are inhomogeneous at some length scale . For a NRIM, the length scale at which we would see this inhomogenity is about the size, δ, of the individual meta-particles (say split-ring resonators etc). Therefore the perfect lens theorem does not apply when field fluctuations are at a length scale, $\eta < \delta$. For a cylindrical wave of angular order ν, and a meta-particle at a radial distance r_m, the length scale of field fluctuation near the meta-particle is given by $\eta \approx 2\pi.r_m/\nu$ (fig 6.4(b)). This means that any cylindrical waves with angular order $\nu > 2\pi.r_m/\delta$, would not see the perfect lens, hence would not contribute to the infinite series in eqn (6.7), curtailing the divergence.

2. Losses in NRIM - We have seen in section 2.3 $\epsilon, \mu < 0$ materials are generally dispersive hence inherently lossy. We also see in section 5.4, that the higher angular order cylindrical waves present in the NRIM material are more affected by losses, thus losses in the NRIM would naturally impose a higher angular momentum cutoff to the series in eqn (6.7).

3. Finite time interval - Generally NRIM works on the principle of resonance (section 2.3 and 3.2), and these resonances take time to be established [92, 93], so the perfect lens scenario strictly holds true only when $t \to \infty$. In general the higher angular order terms of the excitation field takes a longer time to be established so even in the case where there are no inhomogenity/losses, the higher angular order terms will only contribute to the image as $t \to \infty$. For finite time intervals therefore, we would not see this divergence.

We shall discuss points 2) and 3) more quantitatively in chapter 7.

6.4 Results

Now applying the analytical methods introduced in section 6.3, we can examine how losses in general affects the performance of such an array. First, to understand how losses affects a general super phase array, we would study how losses affects a single displaced antenna within a transparent SS in section 6.4.1. Following that in section 6.4.2 we would demonstrate the performance of a super phase array in beam tilting and beam forming in comparison to a normal phase array.

6.4.1 Single displaced antenna

Generally a transmitter placed at $(x_0, 0)$ within a transparent SS, would create an image/impression of a virtual transmitter at $(x_{\text{image}}, 0)$ (where $x_{\text{image}} = r_2^2/r_3^2.x_0$). This means that if a transmitter is placed at distances $x_0 > r_3^2/r_2$ then the image would exist outside the physical structure of the super phase array. This result is clearly shown in fig 6.5. Fig 6.5(a) and (c) are the ray solutions, while fig 6.5(b) and (d) are the full wave solutions for transmitters placed at $x_0 > r_3^2/r_2$ and $x_0 < r_3^2/r_2$ respectively.

It is instructive to take note of the ray diagram for $x_0 > r_3^2/r_2$ fig (6.5(a)). Here we can see that there are 2 types of rays emitting from the source given by the blue and red+green rays (see section 5.3.1; fig 5.4). The first set are the blue rays (called the *impact rays*), which impacts the NRIM layer and gets refracted by it through the conventional Snell's law. The second set, the red+green rays, are more interesting and they are called the *non-impact rays*. The red self-closed loops are localised resonant optical modes in the NRIM layer, which are evanescently coupled to the green rays - rays that do not impact the superlens at all. In general, the smaller (red) self-closed loops are coupled to non-impact (green) rays with a larger impact parameter . Now, because the smaller self closed loops are coupled to non-impact rays that are further away, the coupling strength for these loops are weaker than larger loops. Hence, any losses in the NRIM layer would therefore destroy the coupling of the smaller self closed loops first before the larger ones.

In general then, impact rays are even more robust than the non-impact rays to losses, and non-impact rays with smaller impact parameters are more robust than larger ones.

This can be clearly seen in fig 6.6. Fig 6.6 (a) and (b) are plots for the field amplitude $|E_z|$ as a function of x at a distance $y = 28.75$, for a single antenna. These correspond to the same values of x_0 as in Fig 6.5(a) and (c) respectively. From fig 6.6(a), we can clearly see that as losses increase, the field strength $|E_z|$ for rays with larger impact parameter decay first, and this corresponds to a dip in $|E_z|$ centered at $x = r_2^2/r_3^2.x_0$ (the position of the largest impact parameter). Eventually with sufficient losses, all the evanescently coupled non-impact rays are killed leaving only the impact rays. From fig 6.6(b), since all rays are impact rays, this configuration is

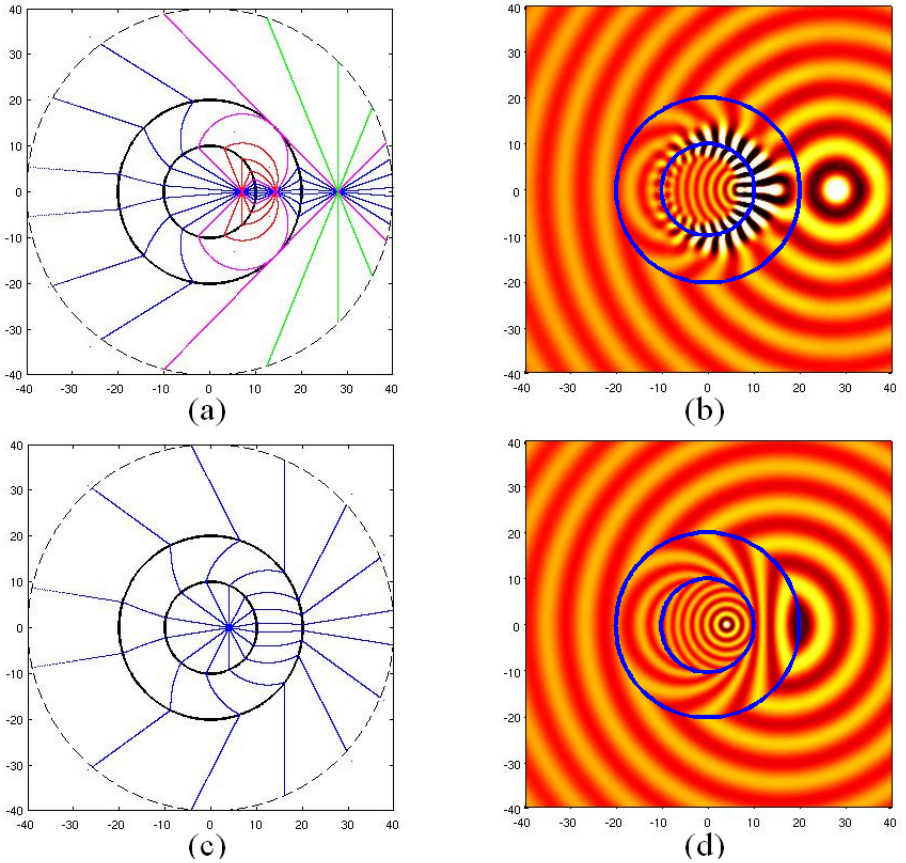


Figure 6.5: Fig (a) and (b) shows the ray and full wave solution respectively of a single antenna displaced by $x = x_0 = 7, y = 0$ from the origin. Similarly fig (c) and (d) shows the ray and wave solution for $x = x_0 = 4, y = 0$. The outer and inner radius of the NRIM is $r_2 = 20$, and $r_3 = 10$. For fig (a) and (c), the blue and magenta rays are impact rays, while the red and green rays are non-impact ones.

more robust to losses, and we do not see any dip in $|E_z|$.

6.4.2 N-array antenna

Having seen the effects of losses - that they affect the non-impact rays (with larger impact parameters) more than the non-impact rays - we can now understand how losses in general affect super phase arrays. Here in this section, we shall demonstrate the ability of an N-array SPA to beam steer and beam focus, and we shall demonstrate how even with losses, they can outperform conventional phase array.

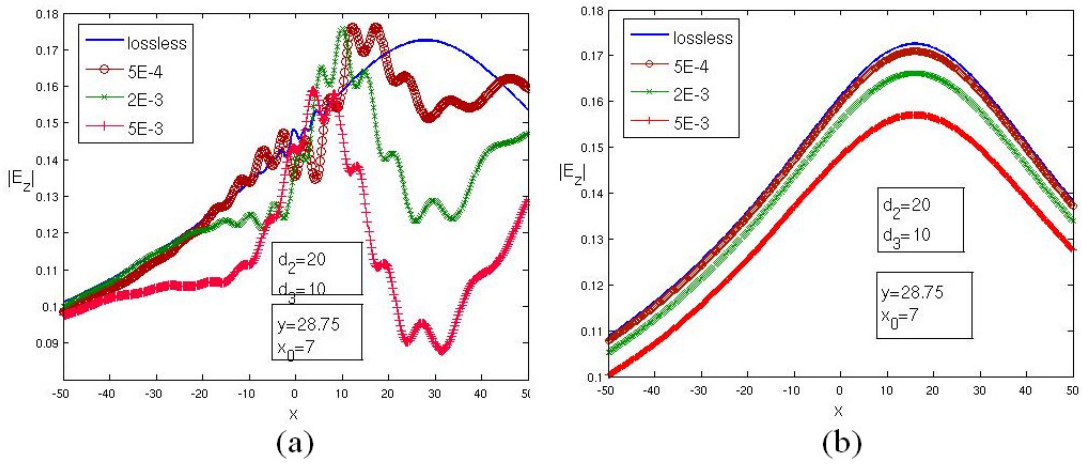


Figure 6.6: Fig (a) and (b) shows the field amplitude $|E_z|$ as a function of x at a distance $y = 28.75$, for a single antenna displaced at $x = x_0 = 7, y = 0$ and $x = x_0 = 4, y = 0$ units away from the origin.

6.4.2.1 Beam steering

Fig 6.7(a) shows the contour plot of a $N = 19$ SPA with each element seperated by $r_0 = 1$. The signal input is given a linear phase shift according to eqn (6.4) such that the beam is tilted by $\alpha = \pi/10$. Now the outer and inner radius of the NRIM is $r_2 = 20$, and $r_3 = 10$, so this means that for a perfectly lossless NRIM, the SPA has a physical size of $d = 2.r_2 = 40$, but a virtual size of $d_{\text{virtual}} = r_2^2/r_3^2.N.r_0 = 76 > d$ - about twice the physical extent.

Now since the directivity (inverse of angular spread) is proportional to the extent of the phase array, a SPA would have a directivity d_{virtual}/d better than a normal phase array with the same physical extent. Indeed when we look at the gain of our SPA (see fig 6.7(b)), we can clearly see that a lossless SPA has a directivity about twice that of a normal phase array (with physical extent of $d = 40$). As we have discussed, we would expect with increasing losses, the virtual extent of the super phase array would decrease and as expected, we see that the directivity of the super phase array drops correspondingly. Still, even with a moderate amount of losses at $\delta = 3 \times 10^{-2}$ the directivity a lossy super phase array still out performs that of a normal phase array.

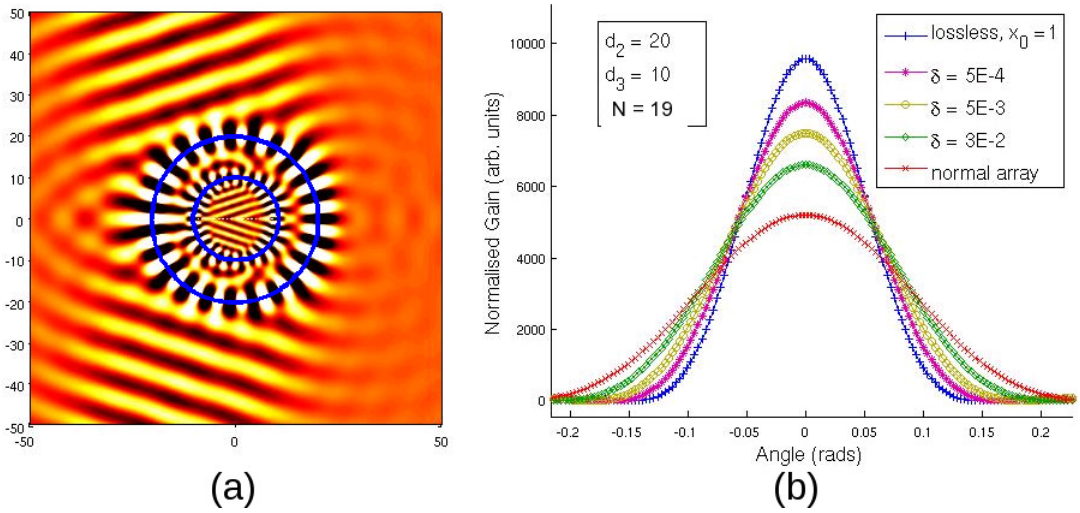


Figure 6.7: Fig (a) shows the contour plot of a $N = 19$ array with each element seperated by $r_0 = 1$ and the signal input to each with a linear phase shift (given by eqn (6.4)) such that a planar waveform tilted at angle $\alpha = \pi/10$. The outer and inner radius of the NRIM is $r_2 = 20$, and $r_3 = 10$, and losses is $\delta = 5 \times 10^{-4}$. Fig (b) shows how the gain of the same setup is affected by losses

6.4.2.2 Beam focusing

Now when we apply a near-parabolic phase shift according to eqn (6.5), we would expect the SPA to focus to a spot a distance $f_0 = r_2^2/r_3^2.f$ units away. Here in fig 6.8 (a) we can see the super phase array (with losses $\delta = 5 \times 10^{-4}$) focusing light to a tight spot at $x = 0, y = f_0 = 48$.

Now the focusing power (the inverse of the angular spread) of a phase array is again proportional to the extent of the array, so we would expect the focal size of our SPA to be d_{virtual}/d smaller than a normal phase array with the same physical extent. Indeed if we examine the field strength at the focus, $|E_z|$, as a function of x (see fig 6.8), we can see that a slightly lossy super phase array ($\delta = 5 \times 10^{-5}$) has about twice the focusing power than a normal phase array. Again with increasing losses, the performance of a super phase array, as we would expect, drops.

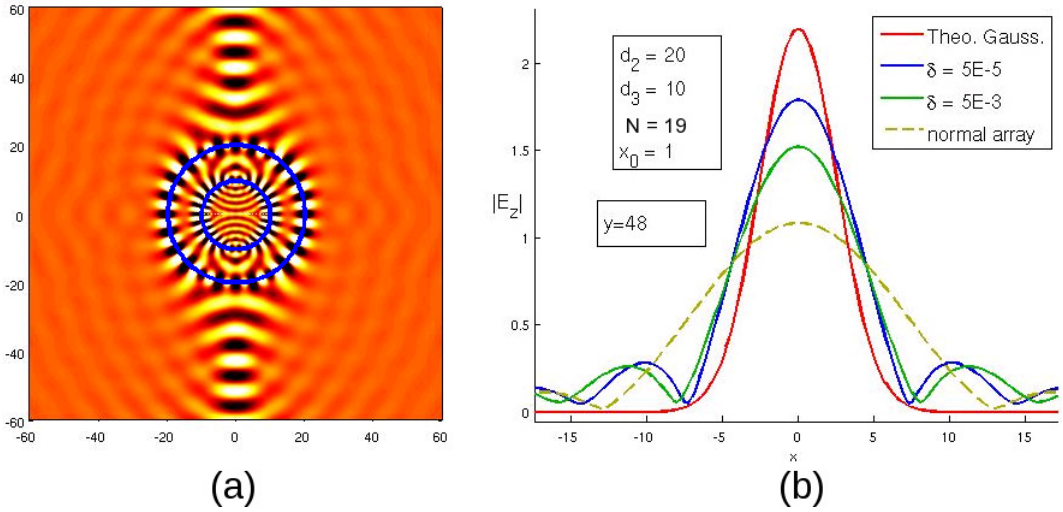


Figure 6.8: Fig (a) shows the contour plot of a $N = 19$, with each element seperated by $r_0 = 1$ and the signal input to each with a near-parabolic phase shift (given by eqn (6.5)) such that a focus is created at $f_0 = 48$. The outer and inner radius of the NRIM is $r_2 = 20$, and $r_3 = 10$, and losses is $\delta = 5 \times 10^{-4}$. Fig (b) shows how the field amplitude $|E_z|$ at the focus is affected by losses.

6.5 Concluding remarks

We have demonstrated how to create a SPA by embedding a normal phase array within a transparent SS, and how by varying the signal input to the phase array, we can alter the radiation pattern - in particular beam tilting and beam forming. We have also outlined a simple analytical procedure to study the full wave solution of the super phase array, by using the addition theorem and transfer matrices. The former is crucial in extending the validity of field symmetries imposed by PLT.

Through the addition theorem, and the PLT, we have also shown the potential problem that the analysis of a perfect lens would pose, namely that fields (when calculated in frequency domain) would unphysically diverge in some regions of space. This issue is subsequently addressed in section 6.4, namely by considering the fact that all real materials are non-homogenous (at some length scale), lossy, and divergences only occurs at $t = \infty$; curtailing the unphysical divergences. The last two points - the effects of losses and time dependence of the perfect lens - we shall discuss in the next chapter.

Finally we also examine how losses in general affects the performance of a SPA,

namely that losses in the NRIM would destroy the non-impact rays with the largest impact parameter first followed by impact rays. Nevertheless, even with moderate losses, it has been shown that SPA has a better directivity, and focusing power than a normal phase array (of the same physical extent), indicating the real possibility of using CPL for enhancement of standard phase arrays.

7. Dynamics of the perfect lens

The advantage of the perfect lens over conventional lenses, lies in it's ability to manipulate not only the light rays but also the evanescent near fields. Undoubtedly, the richness of the perfect lens has open up many new applications previously inaccessible to conventional optics. With transformation optics (chapter 4), we can now design perfect lenses of arbitrary geometry. In particular, we have examined the interesting class of compact perfect lens (CPL). These lenses not only *transfer* optical information from the object to image plane, they also *"super-magnify"* objects which are embedded within them, to sizes much larger than the lens itself. This has applications where we can now "super-compactify" and enhance the properties of scatterers (chapter 5) and transmitters (chapter 6). Besides imaging [19], based on it's optical anti-matter property perfect lenses also have other unexpected applications, such as cloaking "at a distance" [27] and casting optical illusions [28].

While these and many other applications are fascinating, most if not all, the current applications in the literature are based on *steady state*. In reality "perfect lensing", being a resonant phenomenon (see section 2.3), takes time to develop, hence it is natural to ask the following: "how long does this take?" and "what are the effects of losses?" While these were answered before [92, 101, 102], the solutions obtained mainly apply to the flat perfect lens. In view of this and the richness of the general perfect lens, we derive a more general method applicable to lenses of any *arbitrary geometry*.

7.1 Model of a lossy dispersive lens

Since we are interested in the time evolution of a *general* compact perfect lens, we can broadly divide the space into three regions denoted by I =1, 2 and 3, corresponding

to the space outside, within and enclosed by the lens (fig 7.1(a)) . Quantities Q (fields and permeabilities etc) in a specific region I are denoted by Q_I . For our model, we shall assume that region 1 is vacuum and region 3 is designed to look transparent.

To study the time evolution we begin from Maxwell's equations in the frequency domain,

$$\nabla \times \mathbf{E}_I = -i\omega \boldsymbol{\mu}_I.\mathbf{H}_I \quad \nabla \times \mathbf{H} = i\omega \boldsymbol{\epsilon}_I.\mathbf{E}_I \tag{7.1}$$

where $\boldsymbol{\epsilon}_I(\omega), \boldsymbol{\mu}_I(\omega)$ is the permitivity and permeability in region I . Here the physical content of the evolution as we shall shortly see, is captured by the frequency dispersion of $\boldsymbol{\epsilon_2}(\omega)$, $\boldsymbol{\mu_2}(\omega)$. For simplicity let us assume that $\boldsymbol{\epsilon_2}(\omega, \mathbf{x}) = \boldsymbol{\mu_2}(\omega, \mathbf{x})$, and

$$\boldsymbol{\epsilon_2}(\omega, \mathbf{x}) = \Gamma(\omega, \mathbf{x}).\hat{\boldsymbol{\epsilon}}_{\mathbf{2}}(\mathbf{x}) \tag{7.2}$$

where $\hat{\boldsymbol{\epsilon}}_{\mathbf{2}}(\mathbf{x})$ is the permitivity of the lossless perfect lens. $\Gamma(\omega, \mathbf{x})$ is a function which captures the temporal dispersion of the permittivity. At the working frequency ($\omega = \omega_0$) of the lens, $\Gamma(\omega_0, \mathbf{x}) = 1$. Assuming that the temporal dispersion is slowly varying with space ($\Gamma(\omega, \mathbf{x}) \approx \Gamma(\omega)$), and for small frequency deviation ($\omega = \omega_0 + \delta\omega$), we can expand this to first order, as $\Gamma(\omega) \approx (1 + \gamma)$, where $\gamma = \delta\omega.\frac{\partial \Gamma(\omega_0)}{\partial \omega} = \delta\omega.\dot{\Gamma}(\omega_0)$ (henceforth overdots implies derivative i.e. $\dot{Q}(\zeta) = \partial_\zeta Q(\zeta)$) . Effects of losses can also be included by allowing γ to be complex; $\gamma = (\omega - \omega_0).\dot{\Gamma}(\omega_0) - i\sigma$ (where $\sigma \geq 0$ is the loss tangent which we assume to first order to be constant).

7.2 Simplification via symmetry

In general the solution of the fields for the outermost region is simple, since $\epsilon_1 = \mu_1 = 1$ (for some geometries, these have well known solutions[1]). In contrast, the fields within the lens generally are not easily solved. A perfect lens with an arbitrary geometry may have a complicated permitivity/permeability that is both anisotropic and a varying function of space ($\boldsymbol{\epsilon_2}(\omega, \mathbf{x}), \boldsymbol{\mu_2}(\omega, \mathbf{x})$), making the solution of the fields within the lens highly non-trivial. This is further complicated if we consider effects of temporal dispersion and losses.

[1]Since $\epsilon_1 = \mu_1 = 1$, the Maxwell's equations can be written as a single vector Helmholtz equation ($\nabla \times \nabla \times \mathbf{A} - \omega_0^2/c^2 \mathbf{A} = 0$), and this has well known solutions ([103] Pg 1762-1784).

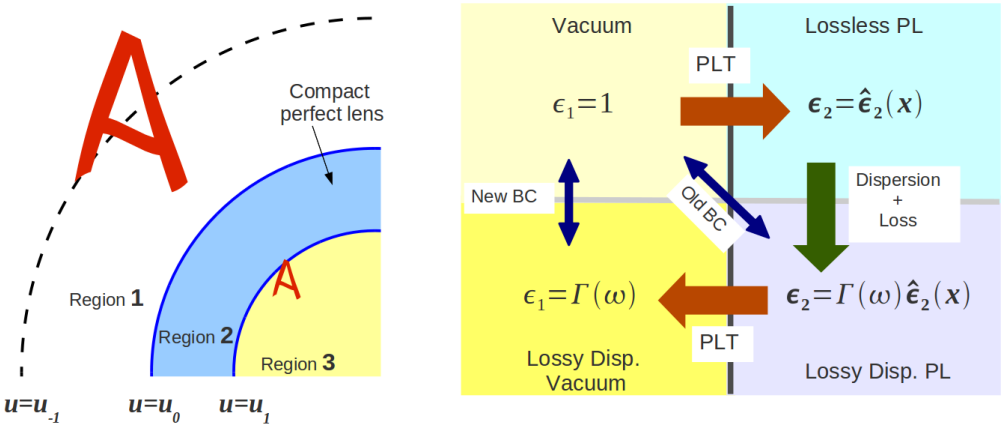


Figure 7.1: Fig (a) illustrates a *general* compact perfect lens (geometry need not be cylindrical). Here the embedded object and its magnified image is denoted by the red font 'A'. The compact perfect lens not only translates but also enlarges the image. Fig (b) shows the schematic of the simplification of boundary conditions (BC). The various quadrants represent the type of materials involved. The complex BC of a lossy dispersive perfect lens is translated to a simplified BC with a "lossy dispersive vacuum"

Fortunately this difficulty can be circumvented if we make use of the symmetry properties of the field solutions imposed by the perfect lens theorem (PLT) (section 4.1). The PLT states that, a perfect lens can be viewed as an optical construct, where fields within the lens (region 2) are a mirror copy of the fields in the space (region 1) that the lens was designed to see through (fig 7.1(a)). This implies that the complicated fields within region 2 can be represented by their simpler image fields in region 1. (these pair of fields/space are referred to as *complementary*). This association of complementary fields therefore implies that complicated boundary conditions at the interface between region 2 and 3 can now be translated to simpler boundary conditions embedded in region 1. (see fig 7.1(b))

Now the deviation, due to losses and dispersion, of the permittivity (permeability) $\boldsymbol{\epsilon_2}(\omega, \mathbf{x})$ from $\hat{\boldsymbol{\epsilon}}_\mathbf{2}(\mathbf{x})$ means that the fields in region 2 are no longer complementary to vacuum in region 1; rather it would be complementary to a *'lossy dispersive material'* given by PLT to be:

$$\boldsymbol{\epsilon_1}(\omega, \mathbf{x}) = \boldsymbol{\mu_1}(\omega, \mathbf{x}) \approx (1 + \gamma) \tag{7.3}$$

It is important to note that the permittivity given above in eqn (7.3) is still *spatially invariant* hence simpler to deal with than eqn (7.2).

Thus, in the same way, we can apply the above discussion of material parameters to the description of fields. If we know the field solutions in region 1 that is filled with vacuum, then the field solutions (in region 1) that is complementary to a lossy dispersive lens (region 2) can be obtained by simple perturbation from these *known solutions*. Now the advantage we gained from this perspective is that the fields thus described are *independent of the detailed description* of the perfect lens and the matching of boundary conditions is *solely dependent* on the geometry of the lens (since the geometry of the lens determines the form of the vacuum field solutions we use)

To see this consider the following. First we consider the problem described by some general set of coordinates given by $\{u, v, w\}$ such that $u = u_j$ (for some constant u_j; $j = \pm 1, 0$) corresponds to the boundaries of the lens - where u_0 and u_1 corresponds to the outer and inner surface (the image plane), and u_{-1} to the object plane/complementary surface to u_1 (see fig 7.1(a)[2]). If we solved for the E field in region 1, using this coordinate system, the solutions can be written as a sum of eigen-modes, where the m-eigenmode is given by $f_m^{\pm}(\gamma|u)$; the '+' and '−', denotes the forward and backward waves respectively; the first argument indicate that these fields are propagating in a material given by eqn (7.3), and the second set of arguments are the coordinates (where u is the only variable, v, w are constant). Thus, written in this denotation, $f_m^{\pm}(0|u)$ would therefore correspond to field solutions for a perfect vacuum.

Similarly we can denote the eigen-modes in region 2 and 3 by $g_m^{\pm}(\gamma|u)$ and $h_m^{\pm}(0|u)$ respectively. The E fields in the various regions of space are then given by:

$$E_1 = \sum_m I_m f_m^+(0|u) + a_m f_m^-(0|u), \quad u \geq u_0 \tag{7.4}$$

$$E_2 = \sum_m b_m g_m^+(\gamma|u) + c_m g_m^-(\gamma|u), \quad u_0 \geq u \geq u_1 \tag{7.5}$$

$$E_3 = \sum_m d_m h_m^+(0|u), \quad u_1 \geq u \tag{7.6}$$

[2]Note the placement of the object and image plane is reversed with respect to the figure. This corresponds to the scattering scenario of chapter 5. Though the object and image plane is readily interchangeable

where I_m is a known coefficient determined by the initial conditions of the object field at $u = u_{-1}$, while a_m, b_m, c_m and d_m are unknown coefficients (see fig 6.3) to be determined by matching boundary conditions.

Now if we have the E fields we can determine the H fields using eqn (7.1). To fix the unknown coefficients a_m, b_m, c_m and d_m we need to match the tangential E and H fields at the boundaries. However at this point it is easy to see that this set of boundary conditions (denoted as "old BC" in fig 7.1(b)) would be difficult to solve. Now, we can simplify the BC, by considering the *field symmetries* due to PLT. The E fields in region 2, at the two boundaries of the lens can then be rewriten as $g_m^{\pm}(\gamma|u_0) = f_m^{\mp}(\gamma|u_0)$, and $g_m^{\pm}(\gamma|u_1) = f_m^{\mp}(\gamma|u_{-1})$. Similarly the E fields in region 3, at the inner boundary can be written as $h_m^{\pm}(u_1) = f_m^{\pm}(0|u_{-1})$, where all the E fields at the boundaries are now solely described by fields embedded within region 1!

Applying the PLT therefore, we would get the following simplified BC (denoted by "new BC" in fig 7.1(b)) at $u = u_0$ and $u = u_1$ respectively:

$$\begin{pmatrix} f_m^{+}(0|0) & f_m^{-}(0|0) \\ f_m^{+\prime}(0|0) & f_m^{-\prime}(0|0) \end{pmatrix}_{\parallel} \cdot \begin{pmatrix} I_m \\ a_m \end{pmatrix} = \begin{pmatrix} f_m^{+}(\gamma|0) & f_m^{-}(\gamma|0) \\ f_m^{+\prime}(\gamma|0) & f_m^{-\prime}(\gamma|0) \end{pmatrix}_{\parallel} \cdot \begin{pmatrix} c_m \\ b_m \end{pmatrix}$$
$$\begin{pmatrix} f_m^{+}(\gamma|-1) & f_m^{-}(\gamma|-1) \\ f_m^{+\prime}(\gamma|-1) & f_m^{-\prime}(\gamma|-1) \end{pmatrix}_{\parallel} \cdot \begin{pmatrix} c_m \\ b_m \end{pmatrix} = \begin{pmatrix} f_m^{+}(0|-1) & f_m^{-}(0|-1) \\ f_m^{+\prime}(0|-1) & f_m^{-\prime}(0|-1) \end{pmatrix}_{\parallel} \cdot \begin{pmatrix} d_m \\ 0 \end{pmatrix} \tag{7.7}$$

where the arguments u_0 and u_{-1} are replaced by numbers 0 and -1 respectively for concision [3]. The first row of the matrices in eqn (7.7) are the E fields while the second are the H fields (from eqn (7.1)) - thus the primed superscript indicates $f_m^{\pm\prime} = -\boldsymbol{\mu}^{-1}.\nabla \times (f_m^{\pm})$. The $\parallel$ sign in the subscript indicates that each element of the matrix is projected onto the u surface. For simplicity we shall assume this projection and drop this sign. The elements of the column vectors, $T_m = a_m/I_m$, $R_m = d_m/I_m$ are the *transmission* and *reflection* coefficients for the m-eigenmode, while c_m, b_m are the amplitudes of the outgoing and incoming eigenmodes within the lens. Note in the simplified BC, everything is written in terms of known solutions embedded in region 1 (a homogeneous medium)!

[3] So $f_m^{\pm}(\gamma|u_0) = f_m^{\pm}(\gamma|0)$ and $f_m^{\pm}(\gamma|u_{-1}) = f_m^{\pm}(\gamma|-1)$.

7.3 General solution of perfect lens

Now we can easily solve the simplified BC (eqn (7.7)), for the transmission and reflection coefficients of a given m-eigenmode

$$T_m(\omega) = \frac{d_m}{I_m} = \frac{1}{\Delta_m}.C_7C_8 \tag{7.8}$$

$$R_m(\omega) = \frac{a_m}{I_m} = -\frac{1}{\Delta_m}.\left(C_1C_2 - C_3C_4\right) \tag{7.9}$$

where the denominator term Δ_m is given by

$$\Delta_m(\omega) = C_2C_5 - C_4C_6 \tag{7.10}$$

where the various function C_i are given by

$$\begin{array}{rclrcl} C_1(\gamma) &=& [f_m^+(\gamma|0), f_m^+(0|0)] & C_5(\gamma) &=& [f_m^+(\gamma|0), f_m^-(0|0)] \\ C_2(\gamma) &=& [f_m^+(0|-1), f_m^-(\gamma|-1)] & C_6(\gamma) &=& [f_m^-(0|0), f_m^-(\gamma|0)] \\ C_3(\gamma) &=& [f_m^+(0|0), f_m^-(\gamma|0)] & C_7(\gamma) &=& [f_m^+(\gamma|-1), f_m^-(\gamma|-1)] \\ C_4(\gamma) &=& [f_m^+(\gamma|-1), f_m^+(0|-1)] & C_8(\gamma) &=& [f_m^+(0|0), f_m^-(0|0)] \end{array} \tag{7.11}$$

where $[a,b] = a.b' - b.a'$ and $a' = \left(-\boldsymbol{\mu}^{-1}.\nabla \times (a)\right)$. We note that when we have an 'ideal' perfect lens, that is in the absence of losses and at the perfect lens working frequency ($\gamma = 0$), it can be easily seen that ($C_2(0) = C_7(0)$, $C_5(0) = C_8(0)$, $C_4(0) = C_6(0) = 0$), $T_m(\omega_0) = 1$ while $R_m(\omega_0) = 0$ which is what we expect. With the equations above, we can now study what happens when we include effects of dispersion and losses (for $\gamma \neq 0$). Before we despair at the complexity of the transmission and reflection coefficients we note that for small γ, the various C_i could be Taylor expanded and C_2, C_3, C_5, C_7 are all $O(1)+O(\gamma)$ while C_1, C_4, C_6 are all $O(\gamma)$. Thus for small γ, retaining the lowest order terms we have,

$$\begin{array}{rcl} T_m(\omega) \approx & \frac{1}{\Delta_m}\left(C_{-1}^{-+}(0)C_0^{+-}(0)\right) \\ R_m(\omega) \approx & \frac{1}{\Delta_m}\left(\dot{C}_0^{++}(0)C_{-1}^{-+}(0) - C_0^{-+}(0)\dot{C}_{-1}^{++}(0)\right)\gamma \\ \Delta_m(\omega) \approx & C_{-1}^{-+}(0)C_0^{+-}(0) - \dot{C}_{-1}^{++}(0)\dot{C}_0^{--}(0)\gamma^2 \end{array} \tag{7.12}$$

where the various function $C_i^{\pm\pm}$ are given by: $C_i^{\pm\pm}(\gamma) = [f_m^{\pm}(\gamma|i), f_m^{\pm}(0|i)]$ (for $i = 0, -1$); the overdots on $C_i^{\pm\pm}$ implies $\partial/\partial\gamma$; and $\gamma = \dot{\Gamma}(\omega_0).(\omega - \omega_0) - i\sigma$.

Now, all the physics of time evolution is captured by the analytic structure of these transmission and reflection coefficients, so we shall briefly discuss about the

analytic properties of $T_m(\omega)$ and $R_m(\omega)$. The poles of $T_m(\omega)$ and $R_m(\omega)$ which are given by the simple zeroes of $\Delta_m(\omega)$, are denoted as $\omega_m = \{\omega \in \mathbb{C} | \Delta_m(\omega) = 0\}$. Because $\Delta_m(\omega)$ is quadratic in ω , there are two (complex) roots given by

$$\omega_{m\pm} = \omega_0 \pm \eta_m + i\hat{\sigma} \tag{7.13}$$

where the $'+'$ subscript refers to the higher frequency and vice-versa,$\hat{\sigma} = \sigma/\dot{\Gamma}(\omega_0)$ is the rescaled losses and

$$\eta_m^2 = \frac{1}{\dot{\Gamma}(\omega_0)^2} . \frac{C_{-1}^{-+}(0) C_0^{+-}(0)}{\dot{C}_{-1}^{++}(0) \dot{C}_0^{--}(0)} \tag{7.14}$$

The real part of these roots $\Re(\omega_{m\pm})$, corresponds to the resonant frequency of the lens[4], where the '+' and '−' subscripts refers to the resonant frequencies of the *antisymmetric* (ASPP) and *symmetric* (SSPP) *surface plasmon polariton* modes respectively. Thus, η_m can be understood to be the coupling strength between these modes.

7.4 Equivalence to simple harmonic oscillators

Now eqn (7.12) strictly holds for $T_m(\omega)$ for positive ω. We can analytically continue this for negative ω if we take into account that T_m, R_m as a function of time are real (the reality condition); that is $T_m(\omega) = T_m^*(-\omega)$ etc. Hence the full T_m should be $T_m(\omega) \sim 1/((\omega - \omega_{m-})(\omega - \omega_{m+})(\omega + \omega_{m-}^*)(\omega + \omega_{m+}^*))$ where the first two poles are for positive ω and the later two are added on for negative ω. Similarly for $R_m(\omega)$ preserving the poles and zeroes, we can analytically continue to negative frequency to get $R_m(\omega) \sim (\omega^2 - \omega_0^2 - 2i\omega\hat{\sigma})/((\omega - \omega_{m-})(\omega - \omega_{m+})(\omega + \omega_{m-}^*)(\omega + \omega_{m+}^*))$.

The transmission and reflection coefficients are then given by:

$$\begin{aligned} T_m(\omega) =& -(2\omega_0\bar{\eta}_m)^2 . \frac{1}{((\omega_0^2 - \omega^2) + 2\omega_0\bar{\eta}_m + 2i\omega\hat{\sigma})((\omega_0^2 - \omega^2) - 2\omega_0\bar{\eta}_m + 2i\omega\hat{\sigma})} \\ R_m(\omega) =& 2\omega_0\bar{\eta}_{m,1} . \frac{(\omega^2 - \omega_0^2 - 2i\omega\hat{\sigma})}{((\omega_0^2 - \omega^2) + 2\omega_0\bar{\eta}_m + 2i\omega\hat{\sigma})((\omega_0^2 - \omega^2) - 2\omega_0\bar{\eta}_m + 2i\omega\hat{\sigma})} \end{aligned} \tag{7.15}$$

where all the 'barred' complex quantities are defined as $\bar{\eta}_m = \Re(\eta_m) + i.\frac{\omega}{\omega_0}\Im(\eta_m)$.

[4]The zeroes of Eqn(7.10), corresponds to the resonant frequency of the perfect lens. Calculating this explicitly for the slab perfect lens then gives us $\Delta_m = (\epsilon_2 k_{z,1} + \epsilon_1 k_{z,2})^2 - (\epsilon_2 k_{z,1} - \epsilon_1 k_{z,2})^2 \exp(2k_{z,2}d) = 0$, which is the equation for the suface plasmon dispersion relation [104].

The constant prefactors[5] in front of the zeroes and poles are added on to satisfy the condition that T_m, R_m in eqn (7.15) are equivalent to the $T_m(\omega > 0)$ $R_m(\omega > 0)$ in eqn (7.12) for $\omega \sim \omega_0$. If we make the following correspondence

$$\begin{aligned} x_l &\rightarrow E_{\text{ref.}}(u = u_{-1}, \omega) \\ x_r &\rightarrow \tfrac{\bar{\eta}_{m,1}}{\bar{\eta}_m} E_{\text{trans.}}(u = u_1, \omega) \\ f &\rightarrow 2\omega_0 \bar{\eta}_{m,1} E_{\text{inc.}}(u = u_{-1}, \omega) \end{aligned} \tag{7.16}$$

We can now re-write all these (eqn (7.15)) in a compact matrix form as

$$\begin{pmatrix} \left(\left(\omega_0^2 - \omega^2\right) + 2i\hat{\sigma}.\omega\right) & -2\omega_0\bar{\eta}_m \\ -2\omega_0\bar{\eta}_m & \left(\left(\omega_0^2 - \omega^2\right) + 2i\hat{\sigma}.\omega\right) \end{pmatrix} \begin{pmatrix} x_l \\ x_r \end{pmatrix} = \begin{pmatrix} f \\ 0 \end{pmatrix} \tag{7.17}$$

If we perform a time domain Fourier transform, (replacing $i\omega$ with ∂_t) on this matrix equation, we can show that the *dynamics* of the perfect lens is then equivalent to

$$\begin{aligned} \ddot{x}_l + 2\hat{\sigma}.\dot{x}_l + \omega_0^2 x_l - 2\omega_0 \Re(\eta_m) x_r - 2\Im(\eta_m)\dot{x}_r &= f \\ \ddot{x}_r + 2\hat{\sigma}.\dot{x}_r + \omega_0^2 x_r - 2\omega_0 \Re(\eta_m) x_l - 2\Im(\eta_m)\dot{x}_l &= 0 \end{aligned} \tag{7.18}$$

which is the equation of motion for a system of 2 coupled simple harmonic oscillators each with a natural frequency of $\omega = \omega_0$! (see fig 7.2) For large m, the fields are predominantly evanescent hence $\eta_m \sim \Re(\eta_m)$ (since all C_i's would be real) and we can ignore the imaginary parts or the velocity dependent coupling in eqn (7.18). One can then easily show that the above formulation is exactly equivalent to Gomez Santos analysis of the flat perfect lens [92].

The strength of the evanescent field coupling is proportional to η_m, which in turn is a measure of the splitting of resonant frequency of the degenerate normal modes from $\omega_0 \rightarrow \omega_{m\pm}$. Before we continue to solve for the time evolution of the lens, let us determine the normal modes of eqn (7.18). When $\sigma = 0$ and $f = 0$, the normal modes are given by $x_\pm = x_l \mp x_r$ for $|x_l| = |x_r| = 1/\sqrt{2}$, where the $x_\pm$ corresponds to normal modes with eigenfrequencies $\omega_{m\pm}$. Note that x_+ and x_- is equivalent to the antisymmetric and symmetric surface plasmon-polariton normal modes respectively. This is what we ought to expect since the antisymmetric plasmon modes are higher in frequency than the symmetric modes for a metallic slab. For the low loss perfect

[5] Explicitly the prefactor $\eta_{m,1}$ is given by $\eta_{m,1} = -\frac{(\dot{C}_1(0)C_2(0) - \dot{C}_4(0)C_5(0))}{\Gamma(\omega_0).\dot{C}_4(0)C_6(0)} \underset{m\rightarrow\infty}{\approx} \frac{1}{\Gamma(\omega_0)}.\frac{C_5(0)}{C_6(0)}$. The last approximation arises because for large m, $f_m^+(\gamma|-1), f_m^-(\gamma|0) \gg f_m^-(\gamma|-1), f_m^+(\gamma|0)$, this means that *for large enough* γ, that $C_4, C_6 \gg C_2, C_3, C_5, C_7, C_8 \gg C_1$

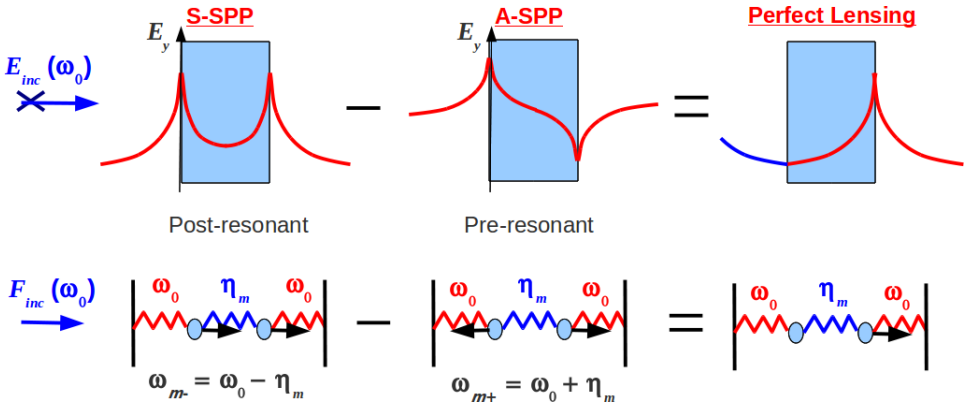


Figure 7.2: Illustration of the analogy between the perfect lens and it's mechanical analogue. An incident field at ω_0 would excite both the symmetric and antisymmetric normal modes (with natural frequencies given by ω_{m-} and ω_{m+} respectively) equally. The superposition of these modes would result in a perfect reflectionless transmission ($R_m(\omega_0) = 0,\ T_m(\omega_0) = 1$).

lens, the driving field E_{inc} at the perfect lens working frequency $\omega = \omega_0$, would excite both the symmetric and antisymmetric normal modes $\omega_{m\pm}$ equally such that the superposition of these normal modes would result in $x_l = 0$ and $x_r = 1$ which of course is equivalent to $T_m(\omega_0) = 1$, $R_m(\omega_0) = 0$ (see fig 7.2).

7.5 Dynamics and limits of *any* perfect lens

Now the time evolution of the perfect lens can be easily obtained from eqn (7.18). When the incident electric field is $E_{\text{inc.}}(u = u_{-1}, t) = \Theta(t)e^{i\omega_0 t}$ the transmitted electric field will be given by: $E_{\text{trans.}}(t) = A(t)e^{i\omega_0 t} + c.c$, where the envelope function $A(t)$ (for large m) is given by:

$$A(t) \simeq \left(\frac{\eta_m^2}{(\eta_m^2 + \hat{\sigma}^2)}\right).(1 - \cos(\eta_m t)\exp(-\hat{\sigma}t)) \tag{7.19}$$

where the term in the first bracket is the steady state solution (as $t \to \infty$) (equivalent to the transmission coefficient $T_m(\omega_0)$) and the second term in the second bracket is the transient term, a consequence of the beating between the $\omega_{m\pm}$ normal modes.

The time t_m, it takes for an m-eigenmode to be established is inversely proportional to the coupling strength η_m, between these modes; $t_m \sim 1/\eta_m$. Since η_m tends to fall off for larger m, this implies that these larger m-eigenmodes takes a longer

time to be established. Consequently, since the smallest feature the lens can resolve is $\Delta x \sim 1/m$, this means the higher resolution would take a much longer time to be developed. In principle, knowing η_m would tell us how long we have to wait before the lens operates at a level where we can see what we want to see. Consequently we can reduce this lag time by selecting materials with smaller dispersion. In addition with eqn (7.19) we can also derive a criterion to determine when losses would dominate and kill the perfect lensing effect. This would occur when the denominator term is dominated by losses - when $\sigma > \dot{\Gamma}(\omega_0)\eta_m$. Substituting eqn (7.14) into this criterion, we can define a critical loss σ_m:

$$\sigma_m^2 = \dot{\Gamma}(\omega_0)^2\eta_m^2 = \left|\frac{C_{-1}^{-+}(0)C_0^{+-}(0)}{\dot{C}_{-1}^{++}(0)\dot{C}_0^{--}(0)}\right| \tag{7.20}$$

where any loss $\sigma > \sigma_m$ would block the transmission of that m-eigenmode. Since σ_m is a monotonically decreasing function with respect to m, eqn (7.20) also tells us the largest m-eigenmode that can be transmitted through - the largest $m = m_c$ satisfying $\sigma_m > \sigma$; m_c in turn would determine the best resolution possible.

7.6 Examples

In this section we shall demonstrate the universality of our analysis by applying the same framework for two different types of perfect lenses - the flat and the cylindrical. We will work out the time it takes for image formation and the limits to resolution.

7.6.1 Flat perfect lens

We can now compare our results with previous work on the time evolution and limits of the flat perfect lens. First, we choose a coordinate system for the flat lens, of thickness d, and the obvious candidate is the cartesian, $\{u, v, w\} = \{x, y, z\}$, where $u_{\pm 1} = \pm d$, $u_0 = 0$. For TM polarisation the E field eigenmodes given by $f_m^{\pm}(\gamma|u) = \exp(\mp k_z z)\hat{\mathbf{y}}$ where $k_z = \sqrt{m^2 - \epsilon(\omega)\mu(\omega).\omega^2/c^2}$ with $\epsilon(\omega) \approx 1 + \gamma$ for small losses and dispersion. Substituting this into eqn (7.14) we get (for large m), the coupling strength to be $\eta_m \sim 2(\dot{\Gamma}(\omega_0)^{-1}\exp(-md)$, which is exactly the same as that Gomez-Santos derived [92]. The time it takes for image formation then is $t_m \sim 1/\eta_m$. Similarly from eqn (7.20), the critical loss (for large m) is $\sigma_m \approx 2\exp(md)$, which tells us that for losses given by σ, the largest m-eigenmode which can be

transmitted through is $m_c \sim \ln(\sigma/2)/d$. Since the limit of image resolution is given by $\Delta x \sim 2\pi/m_c$ we can therefore show that for the slab lens the limit of resolution is given by $\Delta x \sim d/(2\pi.\ln(\sigma/2))$ same as that derived by Smith *et al* [101] and Merlin [102]

7.6.2 Cylindrical perfect lens

Before we discuss the analysis, first we note (from section 5.4.1) that a cylindrical perfect lens with outer and inner radii d_2 and d_3, would *project* an image *magnified* by a factor of d_2^2/d_3^2 at a radii d_1. This means that for the right parameters, some embedded objects spaced at $d < \lambda$ apart can be magnified to sizes $> \lambda$ which can then be visible (resolved) in the far-field (fig 7.4(a)). However for objects which are too closely spaced ($d < 1/m_c$), such lens would be unable to resolve these objects. Now to be more precise, we consider the following.

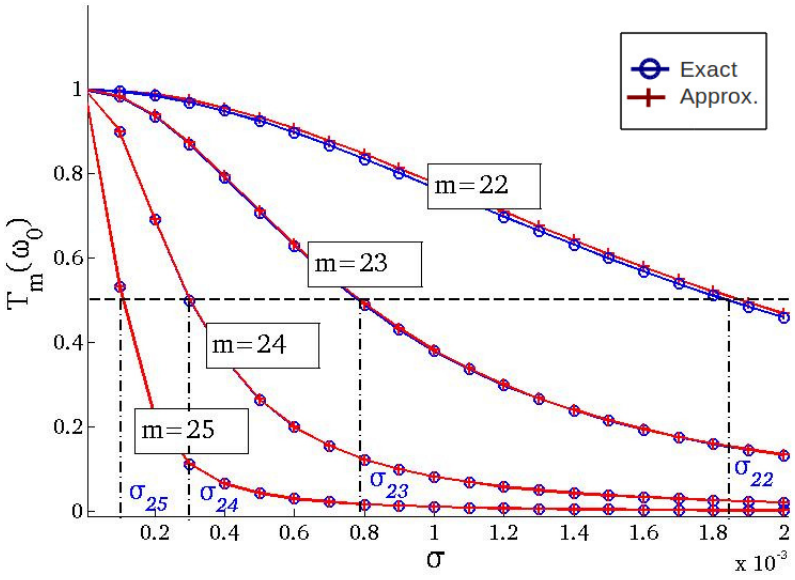


Figure 7.3: Graph of transmission coefficient $T_m(\omega_0)$ as a function of loss σ for the cylindrical perfect lens. The curves are for various m-eigenmode (labelled inset). Here we can see that there is an excellent agreement between numerics (from section 5.4.1) and the approximation (using eqn (7.12)). The critical loss σ_m denoted in the graph, are given by the values of σ where $T_m(\omega_0) = 0.5$.

For the cylindrical lens, the obvious coordinate system to use is the cylindrical polar, $\{u, v, w\} = \{r, \theta, z\}$, where $u_{-1} = d_1$, $u_0 = d_2$ and $u_1 = d_3$. For TE

polarisation the E field eigenmodes are given by $f_m^-(\gamma|u) = H_m^{(1)}(kr)e^{im\phi}\hat{\mathbf{z}}$ and $f_m^+(\gamma|u) = J_m(kr)e^{im\phi}\hat{\mathbf{z}}$, where $k = \sqrt{\epsilon(\omega)\mu(\omega)}\omega/c$ with $\epsilon(\omega) = \mu(\omega) = 1+\gamma$. Substituting these into eqn (7.20), we can determine the critical loss for an m-eigenmode:

$$\sigma_m^2 = \frac{\left(k_0^2 d_1 d_2\right)^2}{[\dot{J}_m(k_0 d_1), J_m(k_0 d_1)][H_m^{(1)}(k_0 d_2), \dot{H}_m^{(1)}(k_0 d_2)]} \tag{7.21}$$

Eqn (7.21), can then be substituted into eqn (7.19) to determine the transmission coefficient $T_m(\omega_0)$ of the lens. Now we can compare the validity of this theoretical result with numerical simulations of $T_m(\omega_0)$ as a function of loss σ of the lens ($d_2 = 20$ and $d_3 = 10$). As can be seen in fig 7.3, the theoretical result compares very well indeed with numerical simulation. Secondly, we note that as expected, losses affect the transmission of larger m eigenmodes more. Thirdly, as an example, we can see from fig 7.3 that for $\sigma \sim 1.8 \times 10^{-3}$, $m_c = 22$. This translates to an angular resolution of $\Delta\theta = 2\pi/m_c$ or $\Delta x \sim \lambda/3$. Together with it's inherent magnification (by factor of d_2^2/d_3^2), this means that using such a lens, a subwavelength object with size $\lambda/3$ would cast a wavelength size ($4 \times \lambda/3$) image (fig 7.4). The lens thus, enables the subwavelength object to be visible in the far field. Furthermore, using eqn (7.21) and a typical dispersion rate $\dot{\Gamma}(\omega_0)$ (estimation based on fishnet structure at $\omega_0 = 170THz$ [13]), we can easily determine t_m (see section 7.5) and show that such an image would take roughly $\sim 60ps$ to be formed (fig 7.4(b)).

7.7 Concluding remarks

Although we have studied and understood much of the mechanics of the compact perfect lens in chapters 5 and 6, this was done so *numerically,* which lacks quantitative predictive power. Here in this chapter, we have shown *analytically* how to understand the *dynamics* of the *general* perfect lens, through which we obtain a *quantitative*, *predictive* measure of the limits and performance of *any* perfect lens.

In summary, we have shown the analogy between a general perfect lens with a set of coupled oscillators. From this, we have a *quantitative* description of the mechanics of the perfect lens, enabling us to determine how losses affects the perfect lens. We can also determine the time required for a particular resolution to occur, which is important in sensing applications. The question of time evolution, is also important, since recent work [44], indicates that NRIM with gain can be achieved using a pulsed

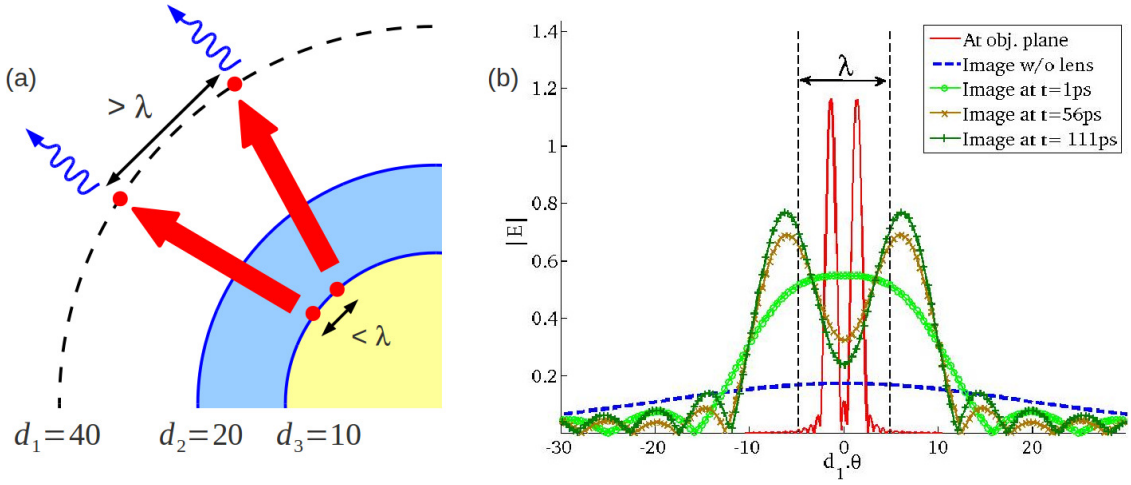


Figure 7.4: Time evolution of an image using a cylindrical perfect lens (losses, $\sigma = 1.8 \times 10^{-3}$). Fig (a) show the schematic of setup. Sub-wavelength objects can be converted to wavelength sized images, which can then be detected in the far field (blue waves). Fig (b) the object is a subwavelength ($\lambda/3$) double slit. Without the lens, the slits are not resolved. With the lens and enough time ($\sim 60ps$; calculation based on the fishnet structure [13]), a clearly *resolved* and *magnified* ($4\times$) image is formed.

pump. This means that for perfect lensing to be observed, the temporal pulse width of the pump has to be larger than this delay time. In this regard, we have shown how we can decrease this delay time by designing meta-materials with smaller dispersion. Finally this formulation we have discussed, is *universal*, in the sense that it does not depend on the details of the lens.

8. Overcoming losses - phase conjugate lens

So far we have seen some of the fascinating properties of NRIM (chapter 2), the *chief* of these, is the "perfect lens" effect - the capacity of a NRIM to optically cancel out the presence of its surrounding PRIM media (chapter 4). In chapters 5 and 6, we saw how PLs created out of such materials, can be exploited to enhance and compactify existing EM devices, and we saw numerically and later analytically (chapter 7), how losses in the NRIM can severely limit the performance of these PLs.

Aside from this, the PL effect is also constrained by the conservation of energy; to optically cancel a *lossy* PRIM space would require a NRIM lens with gain. Therefore to construct an 'ideal' perfect lens - one which can see through anything, even through obstacles with losses - would require some means to add gain to the lens. It is therefore not difficult to see that adding gain to NRIM, is of an imminent and potentially rewarding challenge [38]. Various schemes to add gain have been proposed in the past [39–43], stability of such systems were studied [105, 106] and in recent years seems to bear some promising fruit [44, 45]. While this remains an active area of research, such schemes are not easily implementable in a general PL, since the gain required may have to be spatially varying and precise. It may be that to make practical PL we need a *paradigm shift*, from such a *bottom-up* to a new *top-down* approach: Can we make a PL *directly* without being overly bothered about the details of how to make a low-loss NRIM?

Recently [107], Pendry made use of the intimate connection between *phase conjugation* (PC) and negative refraction as a novel route to a simple PL. The scheme is simple. By sandwiching a slab of vacuum between two phase conjugating sheets (PCS), and applying sufficient gain in the PCS, Pendry showed that this compos-

ite slab behaves as a homogeneous NRIM with refractive index $n = -1$. This is attractive, both in it's simplicity and the fact that gain can be easily incorporated by pumping more power into the PCS. In addition, it has also been shown how this scheme can be experimentally implemented [108], so this in principle should be realisable (at least for propagating waves).

Although it was hinted [107], it was not clear whether this can also be employed for a general non-homogeneous NRIM. It is therefore the intent of this report is to generalise the results of [107]; by introducing a simple strategy for creating the most general inhomogeneous planar NRIM lens using PC. By adding gain, we can then show that such 'active' perfect lenses, can surpass the limits of conventional 'passive' perfect lenses, allowing us even to look through lossy translucent materials.

8.1 Strategy

Before we discuss the strategy, we need to lay down one reminder, one assertion and one terminology. First we are reminded that a perfect lens is a *complementary media* (optical antimatter) to its surrounding space. The prescription for constructing a perfect lens is encoded in the PLT (section 4.1.1), which simply states that the CM has to be a *mirror-copy with* all eigenvalues *reversed* in sign - of which the sign reversal is the more difficult to achieve. The *assertion*, which we shall prove later, is that *phase conjugation* of fields is the mechanism for such sign reversal. And, the *term* for the optical construct, which performs such spatial phase conjugation, is the *Phase Conjugation Sheet* (PCS). In section 8.6 we will describe in detail how to construct such PCS.

First, it is sufficient to note at this point what this PCS does, is it reflects and transmits incident light in such a way that the E fields are firstly *spatially phase conjugated* with respect to the incident fields and secondly *amplified* (the degree of amplification shall be referred to as gain). Second, in section 8.6 we shall show that such PCS is very easy to construct using readily available technology. Now for ease of presentation for the rest of the chapter, we shall assume the surrounding space be a PRIM and the lens to be NRIM.

Here then is the simple strategy [109] :

Given a PRIM slab, find another copy of this slab that is a mirror copy to the first. If we sandwich this mirror-copy between two phase conjugate sheet (PCS) of sufficient "gain", then this slab together with the two PCS becomes a NRIM lens that is complementary to the first PRIM space. (See fig 8.1)

The scheme above is general and applicable to any spatially inhomogeneous PRIM [1], even PRIM which are not time reversal symmetric (lossy materials). The catch in this scheme of course is 'sufficient gain', and we shall show later more quantitatively what 'sufficient' means.

As a matter of notation, the material parameters of the PRIM space are denoted by $\boldsymbol{\epsilon(x), \mu(x)}$. The material parameters for the mirror-copy PRIM are given by $\boldsymbol{\bar{\epsilon}(\bar{x}), \bar{\mu}(\bar{x})}$, where the 'barred' quantities are spatial reflections of the 'un-barred' ones (i.e. if $\mathbf{x} = [x, y, z]$ then $\bar{\mathbf{x}} = [-x, y, z]$ when reflected about $x = 0$ plane; also $\bar{\epsilon}$ has eigen-vectors/optical axes which are spatially reflected with respect to $\boldsymbol{\epsilon}$) (see fig 8.1)

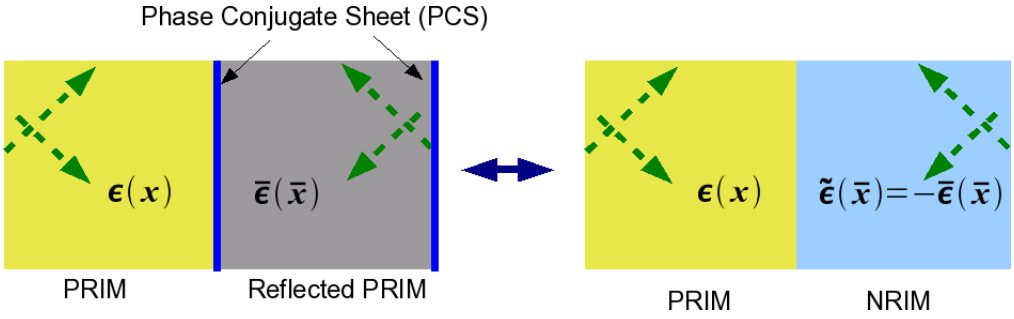


Figure 8.1: Illustration of the strategy. The green dashed lines, ξ_1, ξ_2, indicates the directions of the eigenvectors/optical axes of the PRIM with material parameters $\boldsymbol{\epsilon, \mu}$. Quantities with overhead 'bars' are spatial reflections of 'un-barred' ones. A reflected-copy PRIM sandwiched between two PCS of sufficient gain is equivalent to an effective NRIM lens, that behaves as an optical antimatter/complementary to the PRIM space

[1] The scheme even holds for materials of indefinite signature

8.2 Relationship between eigensolutions

To prove the above strategy (section 8.1), we need first to establish a simple relationship between the field solutions within these two PRIM slabs that are separated by a PCS. Consider two planar slabs of materials described by a Cartesian coordinate system $\{x, y, z\} = \{x, \mathbf{x}_\perp\}$, where the x axis is normal to the slabs and $\mathbf{x}_\perp$ is the perpendicular direction. Let $x < 0$ be filled with the first medium with material parameters $\boldsymbol{\epsilon}(\mathbf{x}), \boldsymbol{\mu}(\mathbf{x})$ (generally inhomogeneous and may be dissipative), and $x > 0$ be filled with the second medium $\bar{\boldsymbol{\epsilon}}(\bar{\mathbf{x}}), \bar{\boldsymbol{\mu}}(\bar{\mathbf{x}})$ [2], and $x = 0$ filled with a PCS. Now the (time harmonic, spatial) Maxwell's equations for $x < 0$ is given by

$$\begin{aligned} \nabla \times E &= -i\omega \boldsymbol{\mu}.H \\ \nabla \times H &= i\omega \boldsymbol{\epsilon}.E \end{aligned} \quad , \quad x < 0 \tag{8.1}$$

Suppose also, that the spatial solutions (of the electric field) to Maxwell's equations for $x < 0$ are given by $E = f_n^{\pm}(x, \mathbf{x}_\perp)$ [3] where the $\pm$ superscript represents the left going $(-)$ and the right going $(+)$ waves and the n subscript indicates it's the n^{th} eigenmode to the equations. Now because we are only interested in the propagation in the x direction, we can ignore $\mathbf{x}_\perp$, simplifying the notation to $E = f_n^{\pm}(x)$.

In general the presence of the PCS at $x = 0$ has two effects on the eigenmodes. Firstly the PCS would perform a phase conjugation to the spatial parts of the eigenmodes. We note that this spatial phase conjugation is also equivalent to frequency inversion[4] $\omega \to -\omega$ [107, 110]. Secondly the PCS can amplify/attenuate, as well as mix the eigenmodes (fig 8.2(b)). This second effect accounts for gain due to phase conjugation, as well as the fact that phase conjugation in general is dependent on the linear momentum of the incoming wave[5]. For the moment we will delay the second consideration to the next section, while we will focus on the first point that passing through a PCS would perform a frequency reversal.

[2] The notation is such that any 'barred' quantities are spatial reflection about $x = 0$ of the 'un-barred' ones

[3] Where $f_n^{\pm}(x, \mathbf{x}_\perp)$ in general is a vector valued function. In general we can always find a orthogonal complete set of basis function, and in this paper we will assume that $\{f_n^{\pm}(x, \mathbf{x}_\perp)\}$ is such a set.

[4] As we can see if $\psi = A(\mathbf{x})e^{i\omega t} + c.c$ then $\psi^* = A^* e^{i\omega t} + c.c = Ae^{i(-\omega)t} + c.c$ (where the $*$ is a spatial phase conjugation operator).

[5] This mixing of eigenwaves at the PCS was not accounted for in [110]

The presence of the PCS then implies that the Maxwell's equations for $x > 0$ is given by

$$\begin{aligned} \nabla \times E &= -i(-\omega)\bar{\boldsymbol{\mu}}.H \\ \nabla \times H &= i(-\omega)\bar{\boldsymbol{\epsilon}}.E \end{aligned} \quad , \quad x > 0 \tag{8.2}$$

Now we note from PLT (see section 4.1), that $\tilde{\boldsymbol{\epsilon}} = -\bar{\boldsymbol{\epsilon}}; \tilde{\boldsymbol{\mu}} = -\bar{\boldsymbol{\mu}}$ is the optical complementary of $\boldsymbol{\epsilon}, \boldsymbol{\mu}$; this implies that if $g_n^{\pm}(x)$ is the (spatial) solution to the Maxwell's equations for $x > 0$, then according to `PLT`, $g_n^{\pm}(x)$ will be a mirror image/spatial reflection of $f_n^{\pm}(x)$. Now for the field solutions to obey causality or the radiation condition, we need $\lim_{x\to\infty} |g_n^{+}(x)| \to 0$, that is fields going away from the interface must decay to zero. Since, we note that $\lim_{x\to-\infty} |f_n^{-}(x)| \to 0$, this means that the right going eigenmode for $x > 0$ is the spatial reflection of the left going eigenmode for $x < 0$, that is $g_n^{+}(x) = \bar{f}_n^{-}(x)$. In turn this also means that $g_n^{-}(x) = \bar{f}_n^{+}(x)$ (where the 'barred' quantities are spatial reflections of the 'un-barred' ones) (see fig 8.2(a)).

Now if instead we consider, a finite slab of material with $\boldsymbol{\epsilon}(\mathbf{x}), \boldsymbol{\mu}(\mathbf{x})$ occupying a space $-d < x < 0$, and another slab of material with $\bar{\boldsymbol{\epsilon}}(\bar{\mathbf{x}}), \bar{\boldsymbol{\mu}}(\bar{\mathbf{x}})$ occupying a space $0 < x < d$, combined with 2 PCS at $x = 0$ and $x = d$; then the same results would hold. The eigenmodes for $-d < x < 0$, would be a spatially reflected copy with respect to the eigenmodes in $0 < x < d$. (see fig 8.2(a)). In the later section we will see that the presence of the second PCS plays a crucial role in transforming the medium in $0 < x < d$ into a true optical complementary medium to the medium in $-d < x < 0$.

8.3 Proof of strategy

Now we shall calculate the overall transmission and reflection coefficients of the two slabs of materials we have previously considered, and show that under certain conditions, the second slab of material (with the two phase conjugation sheets) would behave as a optical complementary (a perfect lens) to the first, so that the overall transmission matrix would be $\mathbf{1}$.

Here we use the bra and ket notation to write the eigenwaves as $|f_n^{\pm}(x)\rangle$, and $|g_n^{\pm}(x)\rangle$[6]. Note that using this notation, $\langle f_n^{\pm}(x)|$ is defined as $\langle f_n^{\pm}|\, f_m^{\pm}\rangle = \delta_{nm}$

[6]By construction $\langle f_n^{\pm}|\, f_m^{\pm}\rangle = \delta_{nm}$. This is almost certainly true since Maxwell's equations are Hermittian

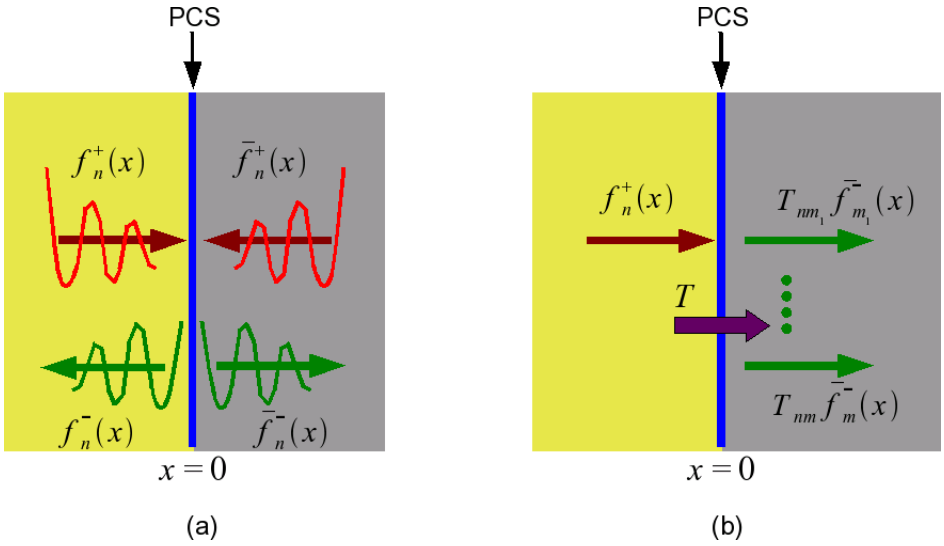


Figure 8.2: Fig (a) illustrates the relationship between the eigenmodes on both sides of the PCS, where the eigenmodes on the right of the PCS is the spatial reflection of the left. The directions of the arrow shows the flow of energy. In particular the right propagating wave is changed from $f_n^+(x)$ on the left of the PCS to $\bar{f}_n^-(x)$ on the right. Fig (b) shows the effect of channel mixing in general, so that an incoming wave $f_n^+(x)$ is scattered to $T_{nm}\bar{f}_m^-(x)$, where T_{nm} encodes the gain/attenuation due to the PCS.

(same for $\langle g_n^\pm(x)|$). *Unless otherwise stated we shall assume the Einstein's summation convention to hold throughout the report.* Now we can define a propagation matrix/operator for $-d < x < 0$, as $P^\pm(x', x) = |f_n^\pm(x')\rangle \langle f_n^\pm(x)|$. Where the propagation matrix allows us to propagate any arbitrary wave function $|\Psi\rangle$ from x to x' by $P^+(x', x)|\Psi\rangle$ (if $x < x'$, that is right going) and by $P^-(x', x)|\Psi\rangle$ (if $x > x'$, that is left going). Similarly for $0 < x < d$, the propagation matrix is given by $Q^\pm(x', x) = |g_n^\pm(x')\rangle \langle g_n^\pm(x)|$. Now using the results of the previous section this propagation matrix can be written more precisely as $Q^\pm(x', x) = \left|\bar{f}_n^\mp(x')\right\rangle \left\langle \bar{f}_n^\mp(x)\right|$.

As we only consider propagation from the $x = -d$ to $x = d$ plane we need only the following:

$$\begin{aligned} P^+(0,-d) &= |f_n^+(0)\rangle \langle f_n^+(-d)| &= P^+ \\ P^-(-d,0) &= |f_n^-(-d)\rangle \langle f_n^-(0)| &= P^- \\ Q^+(d,0) &= \left|\bar{f}_n^-(d)\right\rangle \left\langle \bar{f}_n^-(0)\right| &= Q^+ \\ Q^-(0,d) &= \left|\bar{f}_n^+(0)\right\rangle \left\langle \bar{f}_n^+(d)\right| &= Q^- \end{aligned} \tag{8.3}$$

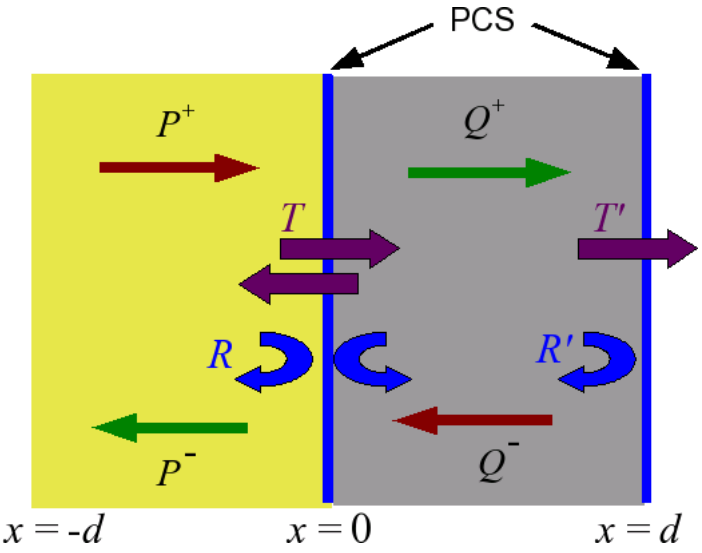


Figure 8.3: Illustration of the various matrices in section 8.3. $P^{\pm}$, $Q^{\pm}$ are the propagation matrices which propagates fields between planes $x = -d$ to $x = 0$ and $x = 0$ to $x = d$ respectively. T, T' (and R, R') are the transmission (and reflection) matrices of the PCS at $x = 0$ and $x = d$ respectively.

Now we can take into account the second consideration of the PCS - that there is an amplifying/attenuation effect and that phase conjugation in general is an function of *linear momentum* - implying that the PCS can also mix eigenwaves (fig 8.2(b)). To model the transmission and reflection of waves at the PCS, we need to define the transmission and reflection matrices at the PCS. Without loss of generality we can assume the transmission (reflection) of a PCS is symmetric (reciprocal); in the sense that transmission (reflection) of a wave traveling from left to right of the PCS is the same in reverse. With this we can define the following transmission matrices:

$$\begin{aligned} T &= \left|\bar{f}_n^-(0)\right\rangle T_{nm} \left\langle f_m^+(0)\right| \\ &= \left|f_n^-(0)\right\rangle T_{nm} \left\langle \bar{f}_m^+(0)\right| \end{aligned}, \quad x = 0 \tag{8.4}$$

$$T' = \left|f_n^+(d)\right\rangle T'_{nm} \left\langle \bar{f}_m^-(d)\right|, \quad x = d \tag{8.5}$$

where the matrix elements T_{nm} and T'_{nm} describes how waves from channel m is scattered to waves in channel n, for the PCS at $x = 0$ and $x = d$ respectively (see fig 8.2(b)), in general these elements are non-diagonal (for the explicit calculation of T_{nm} and T'_{nm} see appendix A.5). Similarly we can define the reflection matrices R and R' for the PCS at $x = 0$ and $x = d$ respectively.

With all these in place (see fig 8.3) we can now calculate the overall transmission/transfer matrix, $\hat{T}_0$ which is given by:

$$\begin{aligned}\hat{T}_0 &= T'.Q^+\left(1+[R.Q^-.R'.Q^+]+[R.Q^-.R'.Q^+]^2+\ldots\right).T.P^+ \\ &= T'.Q^+.\left(\sum_{n=0}^{\infty}[R.Q^-.R'.Q^+]^n\right).T.P^+ \\ &= T'.Q^+.\left(\mathbf{1}-[R.Q^-.R'.Q^+]\right)^{-1}.T.P^+\end{aligned} \tag{8.6}$$

where we used the formulae for the geometric progression for the second line, and $\mathbf{1}$ is the identity matrix. Now if we allow the gain of the reflection matrices to be sufficiently large such that the diagonal elements of the matrices in square brackets $M=[R.Q^-.R'.Q^+]$ is much larger than 1 - that is $M_{nn}=\sum_m R_{nm}R'_{mn}\gg 1$ (no sum over n) - we get from eqn (8.6) the following $\hat{T}_0$:

$$\begin{aligned}\hat{T}_0 &\approx -T'.Q^+.\left([R.Q^-.R'.Q^+]\right)^{-1}.T.P^+ \\ &= -T'.Q^+.[Q^+]^{-1}.R'^{-1}.[Q^-]^{-1}.R^{-1}.T.P^+ \\ &= -\left(T'R'^{-1}\right).[Q^-]^{-1}.\left(R^{-1}T\right).P^+\end{aligned} \tag{8.7}$$

Now, if we design the phase conjugate sheet such that $\left(T'R'^{-1}\right)=\left(R^{-1}T\right)=\mathbf{1}$ we will get:

$$\hat{T}_0\approx -\left[Q^-\right]^{-1}P^+ \tag{8.8}$$

Since the propagation matrix $Q^-=\left|\bar{f}_n^+(0)\right\rangle\left\langle\bar{f}_n^+(d)\right|$, this implies that $[Q^-]^{-1}=\left|\bar{f}_n^+(d)\right\rangle\left\langle\bar{f}_n^+(0)\right|$. Now using again the fact that $\bar{f}^+(x)$ is the spatial reflection of $f^+(x)$, this implies that $[Q^-]^{-1}=|f_n^+(-d)\rangle\langle f_n^+(0)|=[P^+]^{-1}$ (see eqn (8.3)), thus:

$$\hat{T}_0\approx -\mathbf{1} \tag{8.9}$$

Eqn (8.9) implies that any fields at $x=-d$ (object) plane is ideally replicated at $x=d$ (image) plane - the combined effect of these two slabs therefore cancels each other optically.

Finally it should be noted for the above analysis to be valid, the simplification from eqn (8.6) to eqn (8.7) requires the diagonal elements of $M=[R.Q^-.R'.Q^+]$ to be much larger than 1, that is written explicitly:

$$M_{nn}=\sum_m R_{nm}R'_{mn}\gg 1,\quad \text{(no summation over } n) \tag{8.10}$$

where the matrix element R_{nm} and R'_{nm} can be calculated in the same way as eqn (A.12, A.13). This condition given by eqn (8.10), then tells us quantitatively

how much gain the 2 PCS slabs require, in order for the composite slab to behave effectively as a NRIM.

Before we proceed, it should be noted that the key to deriving eqn (8.9) is for the geometric progression: $\sum_{n=0}^{\infty} M^n = (1-M)^{-1}$, in eqn (8.6) to hold for $M_{nn} > 1$. While some may object that this is not convergent [111], we can get around this restriction by appealing to analytic continuation [95, 112], as long as we include all terms up to $n = \infty$. This summation identity would still hold and the derivation for eqn (8.6) would still be valid. In any case we can bypass this problem entirely, as we can derive eqn (8.6) without any infinite sum (see appendix A.6 for an alternate derivation).

Secondly, It should also be that while the derivation for eqn(8.6) holds even for $\|M\| \gg 1$, the minus sign in the the denominator of eqn(8.6), that is $((1-M)^{-1})$, can be a potential problem; especially for some eigenmodes where $M = \mathbf{1}$, would mean that $\hat{T}$ is singular. This problem can be circumvented by designing $R = -R'$ for the two PCS[7]. Then the denominator of eqn (8.6) would be replaced by $(1+M)^{-1}$ and the result would be regular for all values of gain.

8.4 Examples and applications

First, we shall demonstrate that the above "strategy" (section 8.1) can be applied, to construct a simple PCL to "see through" a simple slab of vacuum. For a slab of vacuum, the eigen-solutions are $\left|f_q^{\pm}(x)\right\rangle = |q\rangle\, e^{\pm i k_x x}$ where $k_x = \sqrt{k_0^2 - q^2} = a + ib$, $k_0^2 = \omega^2/c^2$ and q is the transverse momentum states. We can easily show that the transmission and reflection matrices are given by $T = |-q\rangle\, t(q)\, \langle q|$, $T' = |-q\rangle\, t(q) \exp(-2i.ad)\, \langle q|$ and $R' = |-q\rangle\, r(q) \exp(-2i.ad)\, \langle q|$, $R = |-q\rangle\, r(q)\, \langle q|$. Together with the propagation matrices (eqn 8.3) and eqn (8.6), we can show the overall transmission matrix $\hat{T}_0$ is given by:

$$\begin{aligned} \hat{T}_0 &= T'.Q^+.\left(\mathbf{1} - [R.Q^-.R'.Q^+]\right)^{-1}.T.P^+ \\ &= \frac{t^2 \exp(-2b.d)}{1 - r^2 \exp(-2b.d)}\, |q\rangle\, \langle q| \end{aligned} \tag{8.11}$$

where $b = \left|\Im\left(\sqrt{k_0^2 - q^2}\right)\right|$, and eqn (8.11) is essentially the same result as Pendry's derivation for the simple vacuum-PCL [107]. Now we can see that for the PCSs

[7] This can be achieved via a simple phase shift of π radians for one of the pumps of one of the PCS

to behave as a PCL for the q-eigenmode, the gain of the PCS $|r(q)|$, has to satisfy condition (8.10):

$$M_{qq} = r(q)^2 \exp\left(-2b(q).d\right) \gg 1 \tag{8.12}$$

If we insert this condition into eqn (8.11), and set $t(q) = r(q)$, we can easily see that $\hat{T}_0 \approx -\mathbf{1}$ - the perfect lensing scenario - where the q-eigenmode would be perfectly translocated to the image plane at $x = d$ as postulated by Pendry [107]. Since the resolution of the lens depends on how large q is, we see from eqn (8.12), to obtain a better resolution we would need more gain.

Now on to our second example, if instead of vacuum, we want to "see through" a lossy slab of material, can we repeat this strategy? From the conservation of energy, we know that to restore the image, it is necessary for the lens to have gain, which is precisely what a PCL has. It is counter-intuitive, but if we put a copy of the *lossy* medium between 2 PCS , according to our stratagem, it ought to be "inverted" and become an "complementary lens with *gain*" instead. In place of vacuum if we put a homogeneous lossy slab, then going through the same mathematics, basically we would get the same result as eqn (8.11) except $k_0^2 = \omega^2/c^2(1 + i\delta)$ where δ is the loss tangent of the obstacle. Similarly, we would obtain the same condition eqn (8.12), in order for $\hat{T}_0 \approx -\mathbf{1}$ for the q-eigenmode. All this is made more explicit, when we consider the following numerical simulation of what we have discussed (fig 8.4 and 8.5).

As expected in the presence of a lossy obstacle (fig 8.4(b)), we can no longer see the object (fig 8.5(b)). When we partially fulfill the criterion set by the "strategy" (section 8.1), that is if we only have a simple vacuum-PCL - PCSs with sufficient gain but without the mirror-copy in between (fig 8.4(c)) - then we would see some coarse details of the object (fig 8.5(c)). Now if we fully satisfy all requirements, that is if we have an exact-PCL - with sufficient gain *and* with a mirror-copy of the lossy slab (fig 8.4(d)) - then we can clearly see a resolved image of the object ((fig 8.5(d))).

Note that the gain required of the PCS in the PCL must exceed/compensate the loss of the obstacle that one is trying to see through (quantitatively, eqn (8.12)). In this numerical experiment, a modest gain= 50 for each PCS is sufficient to "see through" a lossy obstacle with loss tangent, $\delta = 0.12$. Again, in principle the greater the gain, the more details we can resolve. Now all these, is a truly remarkable

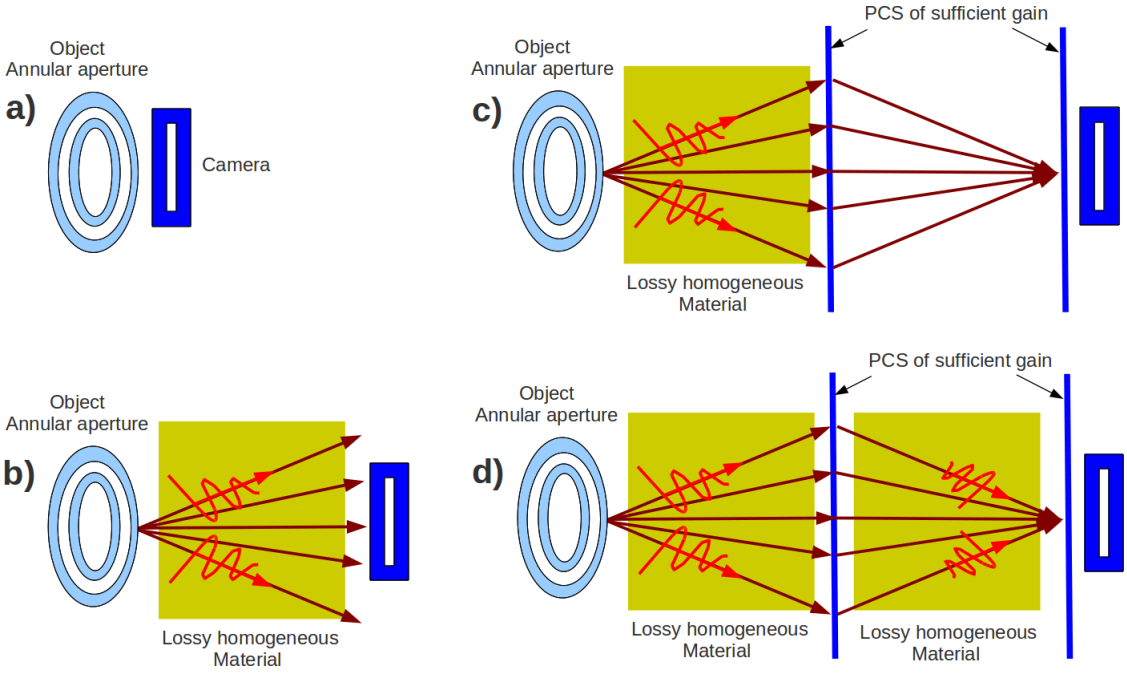


Figure 8.4: Numerical experimental setup. Fig (a) the object is a double annulus. Fig (b) the object is blocked by a lossy slab of material. Fig (c) a simple vacuum-PCL (gain= 50), which performs phase conjugation but has no mirror-copy between, is use to image the object Fig (d) an exact-PCL (gain= 50), satisfying all requirements in section 8.1, is use to image the object.

result, as we now have a simple strategy/scheme to create an "active" perfect-lens that can see through even a lossy and in principle spatially inhomogeneous obstacle, something which cannot be done by conventional passive perfect-lens. Now we are free to imagine scenarios where we can construct perfect lenses which can see through translucent or disordered media such as skin as long as we fulfill all the requirements of the PCL (see fig 8.6).

8.5 Summary of requirements

So in summary what are the requirements to implement the strategy laid out in section 8.1, and what advantages do we gain from making perfect lenses from PCL?

Table 8.1, lays down *four* key requirements to construct such lenses. First and foremost we need a PCS which performs phase conjugation *and* second, it has to transmit and reflect the phase conjugated output equally. We shall see in section 8.6

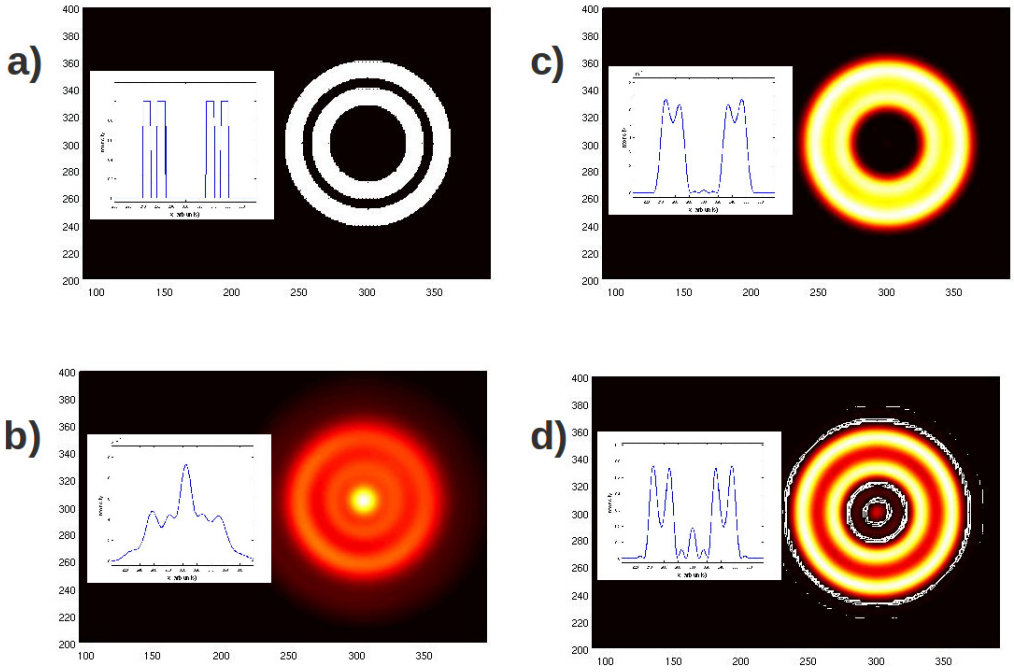


Figure 8.5: Numerical results (a)-(d) corresponding to the setup in fig 8.4. Plots of normalised Intensity: Fig (a) initial field (annulus $d_1 = 1.5\lambda, d_2 = 2\lambda, d_3 = 2.5\lambda, d_4 = 3\lambda$). Fig (b) after propagating through $5.5\lambda$of lossy material (loss tangent $\delta = 0.12$). Fig (c) after passing through a vacuum-PCL (gain= 50). Fig (d) after passing through an exact-PCL. Figure inset shows the intensity cross-sectional profile.

how this can be implemented easily using readily available techniques. If we have such a PCS then to see through an obstacle up to the desired resolution, all we need is enough gain. In principle the more gain we add the better the resolution. Finally if we have prior knowledge of constutive parameters of the obstacle, and if we have a reflected copy of the obstacle, then we can construct a perfect PCL. The question next is what advantages does a PCL have over conventional perfect lens constructed from NRIM metamaterials? Table 8.2 lists the comparison between these two types of lenses. The key distinction between a PCL and a conventional NRIM PL is that the former is a top-down while the later is a bottom-up design. The bottom-up approach begin by a careful *micro*-design of the microstructure (metaparticles), followed by homogenisation as an effective material (see chapter 3). As such the design of such lenses are much more involved. If the obstacle is spatially inhomogeneous (in ϵ, μ and losses), the metaparticles have to be spatially varying in a very *precise* way, adding

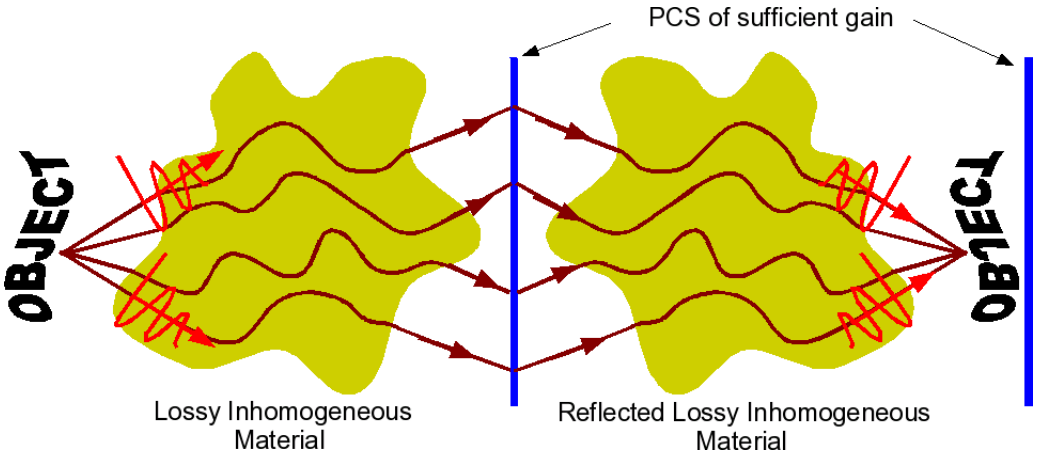


Figure 8.6: Illustration of the perfect PCL. A suitably reflected-PRIM sandwiched between a pair of PCS with sufficient gain is effectively an a 'ideal' perfect lens, that can restore the fields of the object even when these fields have propagated through a lossy medium.

Requirements	Implementation
Phase conjugation	4-wave mixing
$T = R$ and $T' = R'$	Can be made exact by design (See section 8.6)
Enough gain; $M_{nn} \gg 1$, to resolve the n-eigenmode	Sufficient power through pump
Reflected copy of obstacle	Prior knowledge of obstacle

Table 8.1: Requirements for constructing a PCL.

to the complexity of design. Besides this, as we have seen in chapter 3 (section 3.1.1) the plasmonic property of metals forms a natural upper limit to optical frequency NRIM.

In contrast the top-down approach of the PCL circumvents the complexity of the bulk by doing away the need for microstructures. The presence of the PCS "inverts" the properties of the PRIM-copy that is inserted between the PCSs, *macroscopically* giving us an effective NRIM. This inversion is also effective for transforming lossy materials to materials with gain. Such an approach as we have shown is *universal* requiring only 4 requisites (table 8.1), while the former NRIM design is *problem specific*, dependent on the types of applications. In particular gain, especially if spa-

tially varying gain in the bulk is required, is more easily and naturally implemented in the PCS than in the former. Additionally we see that such a *microstructure-less* approach also removes the optical frequency limit of the NRIM. The trade-off of the PCL, of course is that the complexity of the bulk is now transferred to the complexity of the PCS and the scaling limit is now due to the degree of non-linearity of the PC material.

Conventional NRIM PL	PCL
Complexity in bulk microstructure	Complexity in PCS
Spatial variations difficult to implement; through careful design of microstructures	Spatial variations easy to implement in bulk
Mutual coupling of microstructures non-trivial	Mutual coupling absent in bulk
Scaling limitations due to properties of metals	Scaling limits due to non-linearity of PCS
NRIM design is problem specific	PCL design is universal
Gain not easy to control in bulk	Gain easy to control in PCS
Passive PL can't see through lossy obstacles	Active lens - can see through lossy obstacles

Table 8.2: Comparison between a conventional NRIM PL and a PCL

8.6 Experimental setup

While we have demonstrated theoretically how a PCL works. The question remains, how simple is it to implement this experimentally/practically? The purpose of this section is to show how using readily available technology, such a PCL can be constructed.

8.6.1 Phase conjugation sheet

The key ingredient for the PCL is the PCS. And the key property of the PCS is the ability to phase conjugate the input signal.

First, phase conjugation is fundamentally a non-linear process, very well studied [113–132], has been observed and used in numerous optical experiment/applications [116]. There are a number of non-linear processes which can give rise to phase conjugation; such as the degenerate 4WM [113, 118–126], frequency-difference generation (3WM) [114, 115] and stimulated scattering of a highly multimode pump beam [128]. The degenerate 4WM in an isotropic material, is of particular note, since it always satisfy the phase matching condition (unlike 3WM which requires only PC in certain directions), thus we can get PC over a broad angular spectrum. The phenomena of PC from degenerate 4WM can be understood from holography: one of the pump beam interferes with the input wave, to write a grating/holographic image in the non-linear medium, while the second pump beam reads this interference pattern and projects out a PC output. The amplitude of the output wave is dependent on the intensity of the pump waves, as such with enough power, the output can be amplified in comparison to the input.

Besides this, the degree of amplification is also dependent on the degree of non-linearity of the PC media. The types of non-linear media which can be used to perform such 4WM are Kerr-like [118–120], resonant (absorbing/amplifying) [121–123] or photo-refractive [124–126, 133] media, hence a number of possibilities. In this section, we shall use the Kerr-like degenerate 4WM [118–120] to highlight the phase conjugation process. If $E_{p1,2}$ are two equal amplitude counter-propagating pump beams, while E_1, E_2 are the input and output signals, and if we assume negligible pump depletion, and slowly varying amplitude approximation, the 4 waves can be written as:

$$E_{p1}(\mathbf{x},t) = \frac{1}{2}A_p \text{exp}\left[i(\omega t - \mathbf{k_p}.\mathbf{x})\right] + c.c \tag{8.13}$$

$$E_{p2}(\mathbf{x},t) = \frac{1}{2}A_p \text{exp}\left[i(\omega t + \mathbf{k_p}.\mathbf{x})\right] + c.c \tag{8.14}$$

$$E_1(\mathbf{x},t) = \frac{1}{2}A_1(\mathbf{x},t) \text{exp}\left[i(\omega t - \mathbf{k_1}.\mathbf{x})\right] + c.c \tag{8.15}$$

$$E_2(\mathbf{x},t) = \frac{1}{2}A_2(\mathbf{x},t) \text{exp}\left[i(\omega t - \mathbf{k_2}.\mathbf{x})\right] + c.c \tag{8.16}$$

The pumps and the input signal, E_{p1}, E_{p2}, E_1, interact in the nonlinear medium inducing a non-linear polarisation wave, which from phase matching ($\pm\mathbf{k_{p1}} \mp \mathbf{k_{p2}} \pm \mathbf{k_1} = \pm\mathbf{k_2}$) and frequency matching ($\pm\omega_{p1} \pm \omega_{p2} \pm \omega_1 = \pm\omega_2$), is given by

$$P_2(\mathbf{x},t) = \frac{1}{2}\chi^{(3)}A_p^2 A_1^*(\mathbf{x},t) \text{exp}\left[i(\omega t + \mathbf{k_1}.\mathbf{x})\right] + c.c \tag{8.17}$$

where $\chi^{(3)}$ is the third order non-linear susceptibility. This non-linear polarisation wave P_2 re-radiates to give rise to a fourth wave E_2, at ω traveling in the direction $\mathbf{k_2} = -\mathbf{k_1}$, *counter-propagating* to E_1. It is easy to see that $A_2 \propto A_1^*$, therefore the output wave E_2, is *backward* PC with respect to E_1 . It can also be seen that, the amplification of the backward PC wave depends on the degree of nonlinearity $\chi^{(3)}$ and the intensity of the pumps A_p^2.

Such classical degenerate 4WM, however, only produces a backward PC wave. To construct a PCS we would still need a forward PC output. Although, via a 3WM [114, 115] or a 4WM where the pump beams are no longer counterpropagating [129], we can produce a forward PC wave; however such setup are only valid over a restricted angular spectrum. A better alternative is to make use of internal reflections inside the non-linear slab to perform simultaneous forward and backward PC over the whole angular spectrum. This was first theoretically studied [130] and experimentally proven [131, 132] in the 90s. Recently Aubry *et al* revisited this idea [108] and proposed a combination of PC media with a half-silvered mirror (50-50 mirror) to create such a PCS. The partially reflected light from the half-silvered mirror would be PC to produce the forward PC (see fig 8.7). Using a photorefractive media $BaTiO_3$, with realistic absorption, Aubry showed that such a PCS can achieve a theoretical amplification of $\sim 10^2$ (for intensity) for some propagating waves. Further he also demonstrated that such a PCS can be used to make a vacuum-PCL, and demonstrated how well it performs as an imaging device.

8.6.2 Further simplification

In the strategy, proposed in section 8.1, we require 2 sets of PCS to form a cavity (fig 8.8(a)). It turns out that this can be relaxed by replacing one of the PCS with a half-silvered mirror (fig 8.8(a)). The first PCS would provide the crucial PC while the half-silvered mirror would form a reflected image of this PCS. This image then acts as the second PCS and completes the PCL. While this may be a simplification, the issue with this simplified approach (fig 8.8(b)) is that the overall gain is decreased (since the half-silvered mirror has no gain), thus a greater amount of pumping per PCS is required to obtain the same resolution performance as the original approach (fig 8.8(a)).

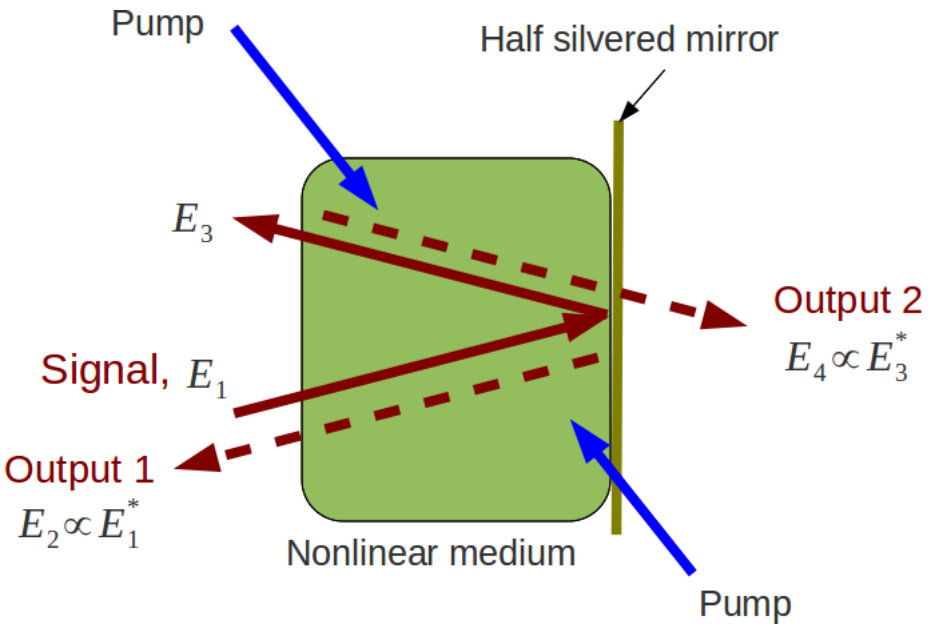


Figure 8.7: Schematics of the PCS based on Aubry's design [108]. The PC waves are indicated by a dashed arrow. The incident field (signal) E_1 generates a backward PC output E_2, from 4 wave mixing. The signal E_1, is also partially reflected from the half-silvered mirror (E_3), which is PC as well. This is partially transmitted through the half-silvered mirror to give a forward PC output E_4.

Now to construct a PCL, another vital requirement other than PC, is the PCS must satisfy the second requirement (table 8.1) - the equipartition of outputs ($T = R$). While the scheme using Aubry's PCS (fig 8.7) does satisfy this condition, it does so *approximately* for a small range of angles (close to normal). Here we propose another scheme which can satisfy the requirements for a broad range of angles (fig 8.9) *exactly*. The scheme basically separates out the task of PC and redistribution of the phase conjugated output in two separate steps. First we would use the nonlinear media as a PCM [117], to perform the necessary phase conjugation, then we would use a half-silvered (50-50) mirror to equally divide the PC output. In this way we can guarantee that we would satisfy $T = R$ precisely for as broad a range of angles as the half-silvered mirror affords. The PCM together with the half-silvered mirror can then be collectively termed as the "PCS". On first sight this second scheme seems similar to Aubry's, though there is a slight distinction in that the PCM does not produce any forward PC wave, thus there is no coupling between the backward and forward

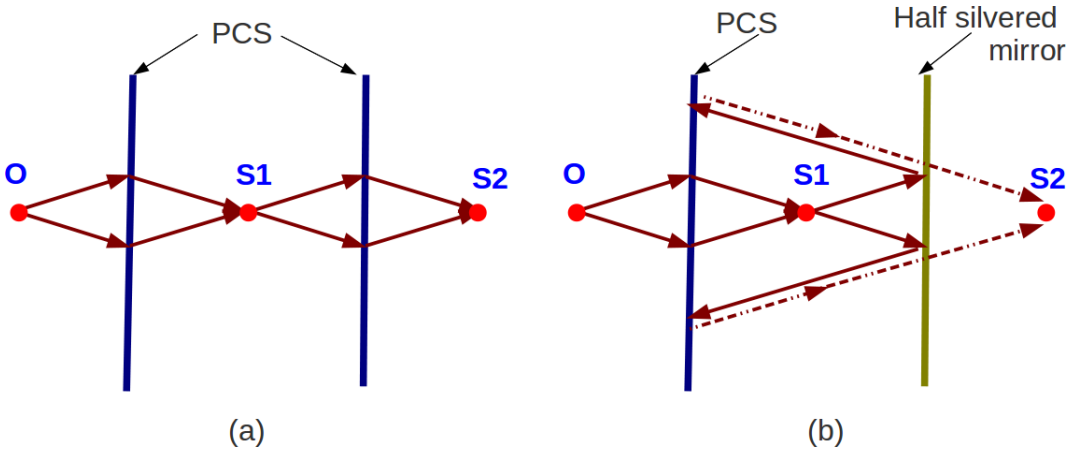


Figure 8.8: Simplification to design. Fig (a) the strategy for constructing a PCL as described in section 8.1 requires 2 PCS. Fig (b) this can be simplified to one PCS, since the image of a PCS due to the presence of a half-silvered mirror behaves as the second PCS.

PC waves. And it is this lack of coupling which broadens the angular spectrum of the PCS satisfying the equipartition requirement exactly.

Incidentally the separation of the PC material from the half-silvered mirror also has another implication. In Aubry's scheme, owing to the proximity between the non-linear media and the half-silvered mirror, it is possible that such a PCS can amplify evanescent near fields. Conversely and unfortunately for our scheme, such evanescent near field amplification is less likely, hence PCL constructed using our scheme may not exhibit sub-wavelength imaging, though it ought to exhibit the ability to see through lossy materials.

8.7 Concluding remarks

We have demonstrated a simple, *universal* approach to constructing an *active perfect lens* , which we call a PCL. Such a lens is "perfect" not only in its subwavelength resolution, it is also "perfect" because it can "see through" lossy obstacles. The theoretical proof for the PCL relies on general, arbitrary eigen-solutions, which bears no distinction between the evanescent near fields and propagating far fields. Thus in the same framework/proof we can demonstrate both subwavelength resolution and its "see through" ability.

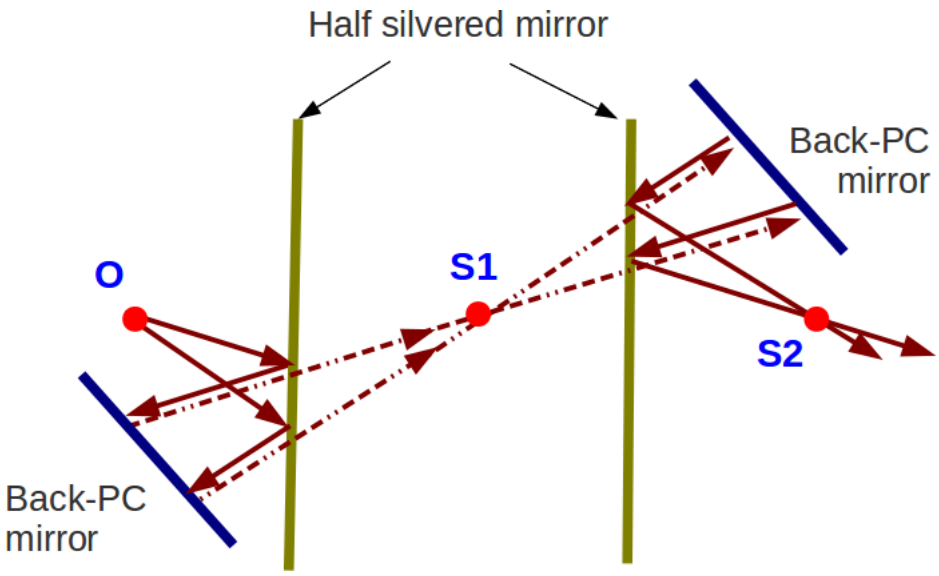


Figure 8.9: A PCL design *without* forward PC (as described in fig 8.8) which only requires a simple standard PCM [117]. This design is better since the requirement of making the transmission and reflection coefficient equal, $T = R$, is *exact*.

We show that the image resolution obtained improves with increasing gain in the PCSs. In theory with sufficient gain we can even restore the evanescent near fields for sub-wavelength imaging. In practice, the restoration of the near fields requires inaccessibly large gain in the PCSs and remains to be seen if it is possible [8]. Nevertheless restoration of the *decaying propagating waves* - that exist in lossy PRIM - can be shown to be easily acheivable with current PC materials[9]. Thus we should still be able to use these lenses to see through lossy, disordered, translucent materials.

The construction of such a PCL requires only 4 requistes (table 8.1). In section 8.6, we demonstrated how the first two requistes could be satisfied. The third and in particular, the fourth, may be relaxed depending on the quality of image desired (for instance compare fig 8.5(c) and (d)). The fourth point is important as we rarely have perfect knowledge of the obstacle we are trying to see through. This implies that

[8] Although, Phase Conjugation (with gain) for near fields have been observed in literature [134–137]

[9] For instance in Fig 8.5(d), the gain required for a lossy material (loss tangent $\delta = 0.12$) is ~ 50. According to Aubry's PCL [108], a gain of ~ 10 (in amplitude) within the same order of magnitude is achievable with photo-refractive materials such as $BaTiO_3$.

if we just want to see "something", we may make use an "approximate" mirror-copy of the obstacle, to construct an "approximately-good-enough" PCL to do the job. Finally the generality of the NRIM obtained through this scheme, implies that we can use transformation optics to deform this planar NRIM to other geometries thus obtaining a more general perfect lens.

9. Conclusion

We come now to the conclusion of this report. First we will briefly outline what we have presented in the report, then we will discuss the importance of what we have done, and finally what further work can be done.

First the outline: we begin in chapter 2, to introduce what is negative refraction and what are some properties of materials, we call NRIM, which exhibits negative refraction. The chief property of interest to us, is perfect lensing - the ability of NRIM to optically cancel the presence of another material. We saw in chapter 2 that thermodynamics constrain NRIM to be dispersive, and this in turn (we saw later in chapter 7) implies that negative refraction takes a finite time to develop. Following this, in chapter 3, we introduce the concept of homogenisation and show how that led to designer materials call metamaterials. The possibility to construct these metamaterials lifts the concept of NRIM from abstraction to reality. While such designer-materials, can in principle be fabricated, we saw the process of designing these materials are involved, with several considerations, and physical limits to the operating frequencies of such materials. More importantly, as we shall see later, losses in metamaterials are a major challenge and obstacle to practical devices which we saw in chapters 5 and 6.

Following this, in chapter 4, we depart from material-design and focus on device-design - that is assuming if we have such materials what can we do with them - and here we introduce the twin concepts of perfect lens theorem and transformation optics. In particular transformation optics is the more general concept, deeply rooted in the powerful principle of general covariance. The passive view of TO enables us to have a more unified classification of EM configurations, leading to simplification of seemingly difficult EM problems. Subtly this concept was repeatedly used in the later chapters (chapter 7 and 8) to simplify the calculations. The active view of

TO led to materials - transformation media - which bends light according to design. Though TO and PLT, gives us a prescription of how to design devices, the trade-off is that such devices are generally anisotropic. In particular anisotropicity in μ, implies in the necessity for magnetic metamaterials, which are more difficult to implement and are more prone to losses. Fortunately, the coordinate transformations used in TO are not unique, and we saw how we can select transformations which minimises anisotropy.

Following this prescription to device-design, we next move on to applications of TO. In chapter 5 and 6 we describe how through TO we can design a special type of PL - the compact perfect lens (CPL) - which can super-magnify objects embedded within, enhancing both the scattering (chapter 5) and transmission properties (chapter 6) of existing devices. In these chapters, through numerical analysis, we saw how losses poses a significant challenge to the performance of these devices. In chapter 7, we introduce a *universal* analytical framework, through which we can *quantitatively* determine how loses affects perfect lensing. In addition, we also discuss the parallel issue of dynamics/time evolution of the general PLs, and gave a theoretical estimate of how long it takes for perfect lensing to be established. In particular we found that the time taken for PL to be established is inversely proportional to the dispersion of ϵ and μ.

From chapters 5, 6 and 7, we know that the problem of losses is a significant challenge that has to be addressed. This brings us to chapter 8, where we propose a paradigm shift, beginning not from homogenisation (chapter 2), but using phase conjugation as a method to "invert" the signs of ϵ and μ to obtain CM. We call such PL the phase conjugate lens (PCL). These PCLs are complementary not only to lossless media, they can also be complementary to lossy media. This allows us to envision a new type of "see-through lens" - one which can see through any type of lossy, disordered, translucent obstacle. In chapter 8, we compare this new top-down approach to PL design with the traditional bottom-up design, and we also proposed practical means to construct these PCLs.

Following the outline, we now discuss the importance of what we have done. First, this report strives to balance between specificity and generality. We illustrated concepts in each chapter with specific examples, with specific applications - namely PLs

- yet these specific concepts are generalised, and set in a more universal framework (take chapters 7 and 8 as an example), which hopefully can be exported for other applications. Secondly, we strive to balance between utility and understanding, that concepts are studied not only for their practicality but also understanding how and why they work - that PLs are not only studied for their practicality, but also to understand how and why they are different to conventional optical devices. Thirdly we hope that we have demonstrated what we set out to achieve; that we can take concepts and *systematically* process them to produce devices (see fig 1.1 in chapter 1). Fourthly we hope that this work can open up new avenues through which we can design metamaterial devices. In particular, we hope that we demonstrated the possibility of employing non-linear processes like PC, in a new paradigm of metamaterial design. Other than imaging, it may be that PCL/PC design could be used for other devices like the light-trapping device based on negative Goos-Hanchen shifts [48]. Finally the PCL which we propose in our work, if it works, has properties that go beyond traditional passive PL. In particular, such lenses can "see-through" translucent obstacles, capable of reversing both phase *and* energy loss, enabling truly "perfect" imaging.

Having discussed the importance of our work, the question is what more can or needs to be done? This work is of course by no means complete, and in many ways there are several important questions to be asked. First we have only studied (in chapter 7) the dynamics of the "traditional" post-resonant PL. Much work need to be done with regards to the dynamics of the PC process in the PCL [138]. In particular the PCL is based on PC with gain, and stability would be a practical issue. It ought to be noted, that even if the PCL is unstable, it may be possible to have some kind of conditional stability by switching on or switching off of the PC for instance, to achieve some kind of dynamical stability. For instance Boardman *et al* [105] demonstrated that if the instability is of a *convective* type, then it may be possible to achieve some form of dynamic stability. Related to question of dynamics would be the parallel question about the frequency bandwidth of such lenses. It would be interesting to determine whether there are physical limitations to bandwidth, if there are what are they, and if so can we make PCL with a broader bandwidth than traditional post-resonant PL. Second, we have only discuss Kerr-like degenerate

4WM to achieve the requiste PC in PCL. The question would be what other type, or what advantages do we gain from other types of PC processes. For instance, can we obtain faster PC? Can we obtain a stronger non-linear response? Are other types of PC process more stable? What are the physical limitations? And so on. Third, PC is a type of time-reversal at one frequency. If this is so, the question would be whether time-reversal *with gain* can be used for constructing broadband PCL. Recent advances in time-reversal technology can now enable fast broadband time-reversal [139]. The difference between a time-reversal imaging [140] and a time-reversed type of PCL is that the later reverses both phase and energy, enabling us to see through lossy obstacles. Fourth, the PCL that we have presented in principle works for both propagating and evanescent near fields, however in practice the PC process for evanescent near fields are still too weak for evanescent field restoration. PC for evanescent near fields is thus something worth looking into.

Recently there is a proposal of using disordered media to scatter evanescent near fields to the far field, then following this, by using PC/time-reversal Lerosey *et al* [141] could enable below diffraction limit focusing of microwaves. It would therefore be interesting to think about whether a similar approach could be use together with the PCL proposed to obtain a subwavelength "see through" lens. Now, moving away from the topic of PCL, we also proposed in chapter 4, section 4.2.4, an optimisation method by which we can select quasi-conformal type of transformations (coordinate transforms which minimises anisotropy). It would be interesting to see if this can be implemented for a simple 3-D configuration to obtain TO media with minimal anisotropy. If so, it would be interesting to see if we can further simplify such TO media by doing away with magnetic metamaterials much like the 2-D carpet cloak proposed by Li *et al* [33]. Finally the analytical method proposed in chapter 7, to analyse the dynamics of a PL so far works for PL of any arbitrary geometry. It would be easy to extend this to multi-layered PL by means of transfer matrices [94]. Such a multi-layered PL for instance has the advantage over a single thick slab of PL, in that the evanescent near field enhancement is spread over many layers hence it ought to be more robust to losses [142]. One approximation of such layered lens for instance is the hyperlens [88–90], which has been experimentally demonstrated to convert near fields to far-fields enabling subwavelength imaging using geometrical

optics. The question then how does time evolution of a multi-layered PL/hyper Lens scale with the number of layers? It would be interesting to see if a similar universal analytical framework proposed in chapter 7 can be applied for such multi-layered lenses.

A. Appendix

A.1 Dispersion of wire-mesh

The problem of determining the electric response of the wire mesh structure can be recasted as a problem in terms of capacitances and inductances [66, 67]

If the wires each has a conductivity σ and the total inductance per unit length of wire, L, and we apply an electric field E_z, then the current I would flow in the wires given by Maxwell-Faraday's law as

$$E_z = \mathrm{i}\omega LI + \sigma\pi r^2 I = \mathrm{i}\omega L_{eff}\pi r^2 nev \tag{A.1}$$

where $L_{eff} = (L - \mathrm{i}\frac{\sigma}{\omega}\pi r^2)$. Noting that the polarization per unit volume in a homogenized medium is given by

$$P_z = (\epsilon_{eff} - 1)\epsilon_0 E_z = \frac{n_{eff} ev}{\mathrm{i}\omega} = -\frac{E_z}{\omega^2 a^2 L_{eff}} \tag{A.2}$$

where we subsitituted v using eqn (A.1) and n_{eff} using eqn (3.11) we can find ϵ_{eff} if we know what L_{eff} is. We can estimate the inductance of the wire mesh, L, by calculating the magnetic flux per unit length passing through a plane between the wire and the point of symmetry (a point midway between two wire pairs):

$$\begin{aligned} \phi &= \mu_0 \int_r^{\frac{a}{2}} H(\rho)d\rho = \frac{\mu_0 I}{2\pi}\int_r^{\frac{a}{2}} \ln\left[\frac{1}{\rho} - \frac{1}{a-\rho}\right] d\rho \\ &= \frac{\mu_0 I}{2\pi}\ln\left[\frac{a^2}{4r(a-r)}\right] \end{aligned} \tag{A.3}$$

Noting that $\phi = LI$, we can therefore determine L, hence L_{eff} giving us

$$\epsilon_{eff}(\omega) = 1 - \frac{\omega_p^2}{\omega^2 + \mathrm{i}\omega.(\epsilon_0 a^2\omega_p^2/\pi r^2\sigma))} \tag{A.4}$$

the effective Drude model of the wire mesh structure; where $\omega_p = \frac{2\pi c^2}{a^2\ln(a/r)}$ (same as eqn (3.13)), and damping parameter $\gamma = (\epsilon_0 a^2\omega_p^2/\pi r^2\sigma)$.

A.2 Dispersion of SRR

First consider a periodic array (see fig 3.4) of concentric cylindrical metallic shells with a gap in them (see Fig 3.5 (b)) This is known as the split-ring resonator (SRR) structure. Assume that a magnetic field of magnitude, H_0, is applied along the length of the cylinders. This will drive an induced current along the shell of the SRR in the direction as shown fig 3.5(b). The large gap in each ring prevents the current, j from flowing around in a single ring, and the circuit is completed across the small capacitive gap between the two rings. Assuming the gap, d is very small compared with the mean radius of the cylinder r, and that the capacitance due to the large gaps in any single ring is negligible, we balance the electromotive forces around the circuit using the Maxwell-Faraday law we obtain

$$\begin{aligned} -\oint_S \dot{B}_z.d\sigma_z &= \oint_C \mathbf{E}.d\mathbf{l} \\ \Rightarrow -\mathrm{i}\omega\mu_0\pi r^2 H_i &= 2\pi r\rho j - \frac{j}{\mathrm{i}\omega C} \end{aligned} \tag{A.5}$$

where ρ is the resistivity of the cylindrical shell, and $C = \epsilon\epsilon_0\pi r/3d$ is the effective capacitance of the SRR with ϵ as the dielectric permittivity of the material in the gap between the cylinders. H_i is the magnetic field inside the cylinder which is assumed to be uniform and it differs from the applied magnetic field H_0 because of the current, j flowing in the cylindrical shells. We note firstly that in the absence of an applied H_0 field, a single semi infinitely long cylinder with a current j in the circumference of the cylinder, would generate a magnetic field $H_1 = j$ along the axis of the cylinder. Now if we consider an infinite 2-D simple square array of such cylinders each separated by a distance of a. And using the idea that since $\nabla.\mathbf{B}$ =0, the magnetic flux inside all the cylinders has to be equal to the magnetic flux outside all the cylinders as well. We can then easily deduce that there is a depolarising magnetic field $H_{\text{depolarisation}} = -H_1\frac{\pi r^2}{a^2}$. This means that when we apply a magnetic field H_0 into this infinite array, taking into account the depolarisation field, the local magnetic field in the host is

$$\begin{aligned} H_{\text{local}} &= H_0 + H_{\text{depolarisation}} \\ &= H_0 - j\frac{\pi r^2}{a^2} \end{aligned} \tag{A.6}$$

Hence applying the Maxwell Ampere Law we find that the final corrected magnetic field inside each cylinder, H_i is related to the applied magnetic field H_0 by

$$\begin{aligned} H_i - H_{\text{local}} &= j \\ \Rightarrow H_i &= \left(H_0 - j\frac{\pi r^2}{a^2}\right) + j \end{aligned} \tag{A.7}$$

Now inserting eqn (A.7) into eqn (A.5) we can determine what j is, which we can substitute back into eqn (A.6) to determine the local magnetic field within the host, H_{local}. Then using Pendry's homogenisation technique, as discussed in section 3.1.2 in particular eqn (3.5) and eqn (3.7), we see that $H_{eff} = H_{\text{local}}$, and $B_{eff} = \mu_0 H_0$ so that the effective permeability according to eqn (3.1) is

$$\mu_{eff} = \frac{B_{eff}}{\mu_0 H_{eff}} = 1 - \frac{\pi r^2/a^2}{1 - (3d/\mu_0\epsilon_0\epsilon\pi^2\omega^2 r^3) + \mathrm{i}(2\rho/\mu_0\omega r)} = 1 + \frac{f\omega^2}{\omega_r^2 - \omega^2 - \mathrm{i}\Gamma\omega} \tag{A.8}$$

and thus we have which has a Lorentz type dispersion. Here $f = \pi r^2/a^2$ is the filling fraction of the cylinder compared to the host medium, $\Gamma = (2\rho/\mu_0 r)$ is the damping parameter and:

$$\omega_r = \left(\frac{3d}{\mu_0\epsilon_0\epsilon\pi^2 r^3}\right)^{1/2} \tag{A.9}$$

as the resonant frequency.

A.3 Group theoretical considerations in metamaterial design

The geometry and orientation of the individual metaparticle affects the magneto-electric response (or the constitutive parameters) of the metamaterial. A systematic approach to design of a metamaterial is to consider group symmetries [76]. The essence of the method is as follows:

1. First identify the point group symmetry of the metaparticle.
2. Determine the *irreps* of the metaparticle using the Shur orthogonality theorem.
3. Associated with each irrep is a linear basis function which transforms as an irrep of the group. The x, y, z functions are associated with E fields and the $R_i = \varepsilon_{ijk}\partial_k$ (R_i is the rotation about i-axis; where $i, j, k = x, y, z$) with B fields.

4. This implies that if an irrep contains only x, y, z basis functions then the metaparticle is purely electric in response (similar for magnetic fields), while a mix of x, y, z and $R_{x,y,z}$ basis function indicates an electro-magnetic (bianisotropic) response.

5. Repeat the procedure for a single unit cell to determine the response of the metamaterial

We can also invert such an approach. That is given a particular desired type of magneto-electric response how do we design the appropriate metaparticle?

For instance, from a quick survey of all crystallographic point group character tables, we can easily see that to construct a *3D* isotropic magnetic metamaterial free from magneto-optical activity, then we have to use metaparticles/unit cells with the following point group symmetries: T_h , T_d, I_h, and O_h (Schönflies notation).

A.4 Scattering coefficients of the SPA

The scattering coefficients of eqn (6.8) to eqn (6.10) are given by:

$$\begin{aligned} a_m &= \tfrac{C_1C_2-C_3C_4}{C_2C_5-C_4C_6}.I_m \\ b_m &= \tfrac{2\mathrm{i}}{\pi}\cdot\tfrac{1}{k_3r_3}\cdot\tfrac{C_2}{C_2C_5-C_4C_6}.I_m \\ c_m &= -\tfrac{2\mathrm{i}}{\pi}\cdot\tfrac{1}{k_3r_3}\cdot\tfrac{C_4}{C_2C_5-C_4C_6}.I_m \\ d_m &= \left(\tfrac{2\mathrm{i}}{\pi}\right)^2\cdot\tfrac{1}{k_2r_2}\cdot\tfrac{1}{k_3r_3}\cdot\tfrac{1}{C_2C_5-C_4C_6}.I_m \end{aligned} \tag{A.10}$$

where I_m is given by eqn (6.12) and the constants C_1 to C_6 are given by:

$$\begin{aligned} C_1 &= H_m^{(1)}(k_2r_1)H_m^{(1)\prime}(k_3r_3) - H_m^{(1)}(k_3r_3)H_m^{(1)\prime}(k_2r_1) \\ C_2 &= J_m(k_2r_2)H_m^{(1)\prime}(k_1r_2) - H_m^{(1)}(k_1r_2)J_m'(k_2r_2) \\ C_3 &= J_m(k_2r_1)H_m^{(1)\prime}(k_3r_3) - H_m^{(1)}(k_3r_3)J_m'(k_2r_1) \\ C_4 &= H_m^{(1)}(k_2r_2)H_m^{(1)\prime}(k_1r_2) - H_m^{(1)}(k_1r_2)H_m^{(1)\prime}(k_2r_2) \\ C_5 &= J_m(k_3r_3)H_m^{(1)\prime}(k_2r_1) - H_m^{(1)}(k_2r_1)J_m'(k_3r_3) \\ C_6 &= J_m(k_3r_3)J_m'(k_2r_1) - J_m(k_2r_1)J_m'(k_3r_3) \end{aligned} \tag{A.11}$$

where the wavevectors k_1 to k_3 is given by eqn (6.11) and $r_1 = r_2^2/r_3$.

A.5 Explicit calculation of elements of transmission matrices

In general because phase conjugation depends only on the transverse momentum, the transmission matrix is only diagonal in the momentum basis, hence these elements are given explicitly by

$$T_{nm} = \sum_k \left\langle \bar{f_n}^-(0) \right| -k\rangle \, t(k) \hat{\Phi} \, \langle k \left| f_m^+(0) \right\rangle , \text{ (no sum over m)} \tag{A.12}$$

$$T'_{nm} = \sum_k \left\langle f_n^+(d) \right| -k\rangle \, t(k) \hat{\Phi} \, \langle k \left| \bar{f}_m^-(d) \right\rangle , \text{ (no sum over m)} \tag{A.13}$$

where $\langle k \left| f_m^{\pm}(x) \right\rangle = \int d\mathbf{x}_\perp f_m^{\pm}(x, \mathbf{x}_\perp) e^{ik.\mathbf{x}_\perp}$ is the projection of the eigenwave from $|f_m^{\pm}(x)\rangle$ basis to $|k\rangle$ basis[1], and $\langle f_n^{\pm}(x)| \, k\rangle$ is the reverse. $t(k)$ is a real function which determines the gain for plane waves with transverse momentum k. $\hat{\Phi}$ is a phase conjugation operator which acts only on $\mathbb{C}$ numbers, performing complex conjugation on the right of the operator (If a is a complex number then$\hat{\Phi}a = a^*$). This phase conjugation operator is necessary to impose the right boundary conditions at the phase conjugation sheets. We note that we can move $\mathbb{C}$ numbers to the right of the operator by performing complex conjugation on that number so that $\hat{\Phi}ab = a^*\hat{\Phi}b$. This means that eqn (A.12) and eqn (A.13) can be rewritten as:

$$T_{nm} = \sum \hat{\Phi} \left[\left\langle \bar{f_n}^-(0) \right| -k\rangle \right]^* t(k) \, \langle k \left| f_m^+(0) \right\rangle , \text{ (no sum over m)} \tag{A.14}$$

$$T'_{nm} = \sum_k \hat{\Phi} \left[\left\langle f_n^+(d) \right| -k\rangle \right]^* t(k) \, \langle k \left| \bar{f}_m^-(d) \right\rangle , \text{ (no sum over m)} \tag{A.15}$$

Now the expression for the reflection matrices are the same so that the explicit elements of $M = [R.Q^-.R'.Q^+]$ given by $M_{ln} = R_{lm}R'_{mn}$ is given by:

$$\begin{aligned} M_{ln} &= \sum_m R_{lm} R'_{mn} \\ &= \sum_m \left[\sum_{k'} \left\langle \bar{f}_l^-(0) \right| -k\rangle \, r(k) \hat{\Phi} \, \langle k \left| \bar{f}_m^+(0) \right\rangle \sum_k \left\langle \bar{f}_m^+(d) \right| -k\rangle \, r(k) \hat{\Phi} \, \langle k \left| \bar{f}_n^-(d) \right\rangle \right] \\ &= \sum_m \left[\sum_{k'} \left\langle \bar{f}_l^-(0) \right| -k\rangle \, r(k) \left[\langle k \left| \bar{f}_m^+(0) \right\rangle \right]^* \sum_k \left[\left\langle \bar{f}_m^+(d) \right| -k\rangle \right]^* r(k) \, \langle k \left| \bar{f}_n^-(d) \right\rangle \right] \end{aligned} \tag{A.16}$$

where we used the property illustrated in eqn (A.14), (A.15) and the fact that $\hat{\Phi}\hat{\Phi} = 1$ to remove the complex conjugation operator. The diagonal elements of M obtained

[1]The Fourier transform of the eigenwave at the sheet

from eqn (A.16) is important in determining how much gain the phase conjugation sheets require in order to observe the effect of negative refraction - that is $M_{nn} = \sum_m R_{nm} R'_{mn} \gg 1$.

A.6 Alternative calculation of overall transfer matrix

A common objection might be raised about the derivation of eqn (8.6). The key to deriving eqn (8.6) is the summation $\sum_{n=0}^{\infty} M^n = (1-M)^{-1}$ for all M except for $M = 1$. Some might object that the summation identity only converges for M such that $M_{nn} < 1$. Strictly speaking one can overcome this by appealing to analytic continuation, as long as we include all the terms up to $n = \infty$, and this summation identity should still hold.

In anticipation of this objection, this subsection is an alternative derivation of eqn (8.6). Using the method of undetermined coefficients. Define the following undetermined matrices A, B, C and D such that (if $|\psi\rangle$ is the field at $x = -d$) $|A\rangle = A|\psi\rangle$ is the field at $x = 0^-$ similarly $|B\rangle = B|\psi\rangle$ at $x = 0^+$, $|C\rangle = C|\psi\rangle$ at $x = d^-$ and $|D\rangle = D|\psi\rangle$ at $x = d^+$. Taking into account the boundary conditions, the undetermined matrices then satisfies the following coupled simultaneous equation

$$\begin{aligned} A &= R.P^+ + T.Q^- C \\ B &= T.P^+ + R.Q^- C \\ C &= R'Q^+ B \\ D &= T'Q^+ B \end{aligned} \tag{A.17}$$

Solving for these we get

$$\begin{aligned} A &= R.P^+ + T.Q^- R'Q^+ \left(1 - RQ^- R'Q^+\right)^{-1} TP^+ \\ B &= \left(1 - RQ^- R'Q^+\right)^{-1} TP^+ \\ C &= R'Q^+ \left(1 - RQ^- R'Q^+\right)^{-1} TP^+ \\ D &= T'Q^+ \left(1 - RQ^- R'Q^+\right)^{-1} TP^+ \end{aligned} \tag{A.18}$$

where we note that $D = \hat{T}_0$ in eqn (8.6)

Note firstly that the above derivation does not require any summation identity. In addition we note that since all the undetermined matrices A, B, C and D are finite even for M such that $M_{nn} > 1$, therefore eqn (A.18) is a valid solution to the

scattering problem. By uniqueness theorem then, since this is a valid solution it is also the only unique solution.

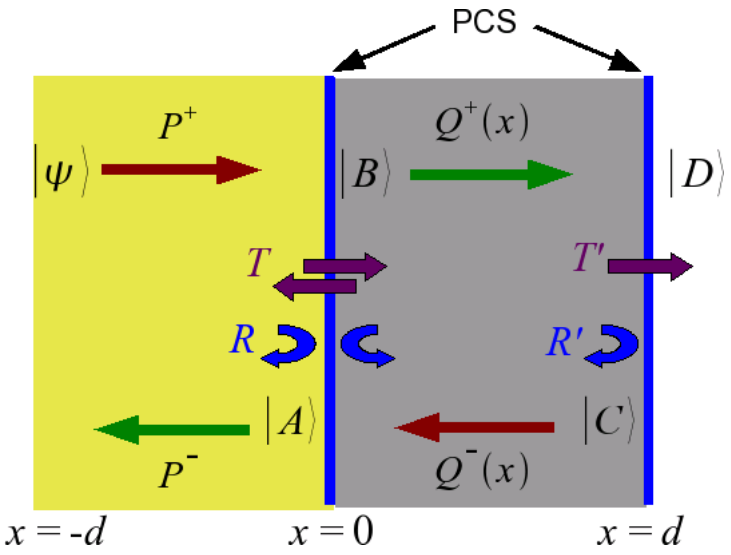


Figure A.1: Illustration of the various matrices used in section A.6

Bibliography

[1] James Clerk Maxwell. *A Treatise on Electricity and Magnetism.* Clarendon Press Series, 1873.

[2] Jackson JD. *Classical Electrodynamics.* John Wiley and Sons, 2nd edition, 1975.

[3] Landau LD, Lifshitz EM, and Pitaevskii LP. *Electrodynamics of Continuous Media.* Pergamon Press, 2nd edition, 1984.

[4] Veselago VG. The electrodynamics of substances with simultaneously negative values of ε and μ. *Soviet Phys. Ups.*, 10:509, 1968.

[5] Pendry JB, Holden AJ, Stewart WJ, and Young I. Extremely low frequency plasmons in metallic mesostructures. *Phys. Rev. Lett.*, 76:4773–6, 1996.

[6] Pendry JB, Holden AJ, Robbins DJ, and Stewart WJ. Low frequency plasmons in thin - wire structures. *J Phys.: Condens. Matter*, 10:4785–809, 1998.

[7] Pendry JB. Magnetism from conductors and enhanced non-linear phenomena. *IEEE Trans. Micr. Theo. Tech.*, 47:2075, 1999.

[8] Smith DR, Padilla WJ, Vieer DC, Nemat-Nasser SC, and Schultz S. Composite medium with simultaneously negative permeability and permittivity. *Phys. Rev. Lett.*, 84:4184–87, 2000.

[9] Shelby RA, Smith DR, and Schultz S. Experimental verification of a negative index of refraction. *Science*, 292:77, 2001.

[10] Zhang S, Fan W, Malloy KJ, Brueck SR, Panoiu NC, and Osgood RM. Near-infrared double negative metamaterials. *Optics Express*, 13:4922–4930, 2005.

[11] Dolling G, Enkrich C, Wegener M, Soukoulis CM, and Linden S. Low-loss negative-index metamaterial at telecommunication wavelengths. *Optics Lett*, 31(12):1800–1802, 2006.

[12] Dolling G, Enkrich C, Wegener M, Soukoulis CM, and Linden S. Simultaneous negative phase and group velocity of light in a metamaterial. *Science*, 312:892–4, 2006.

[13] Valentine J, Zhang S, Zentgraf T, Ulin-Avila E, Genov DA, Bartal G, and Zhang X. Three-dimensional optical metamaterial with a negative refractive index. *Nature*, 455:376–9, 2008.

[14] Shalaev VM, Cai W, Chettiar UK, Yuan H K, Sarychev AK, Drachev VP, and Kildishev AV. Negative index of refraction in optical metamaterials. *Optics Lett*, 30:3356–58, 2005.

[15] Yannopapas V and Moroz A. Negative refractive index metamaterials from inherently non-magnetic materials for deep infrared to terahertz frequency ranges. *J Phys:Condens. Matt*, 17(25):3717, 2005.

[16] Alu A, Salandrino A, and Engheta N. Negative effective permeability and left handed materials at optical frequencies. *Optics Express*, 14:1557–66, 2006.

[17] Shalaev VM. Optical negative-index metamaterials. *Nature Photonics*, 1:41–8, 2007.

[18] Pendry JB. Negative refraction makes a perfect lens. *Phys. Rev. Lett.*, 85:3966–69, 2000.

[19] Fang N, Lee H, Sun Cheng, and Zhang X. Sub-diffraction-limited optical imaging with a silver superlens. *Science*, 308:534–537, 2005.

[20] Iyer A, Kremer P, and Eleftheriades GV. Experimental and theoretical verification of focusing in a large, periodically loaded transmission line negative refractive index material. *Optics Express*, 11:696–708, 2003.

[21] Grbic A and Eleftheriades GV. Overcoming diffraction limit with a planar left handed transmission-line lens. *PRL*, 92:117403, 2004.

[22] Zhu J and Eleftheriades GV. Experimental verification of overcoming the diffraction limit with a volumetric veselago-pendry transmission-line lens. *PRL*, 101:013902, 2008.

[23] Pendry JB and Ramakrishna SA. Focussing light using negative refraction. *J Phys.: Condens. Matter*, 15:6345–64, 2003.

[24] Tao Yang, Huanyang Chen, Xudong Luo, and Hongru Ma. Superscatterer: Enhancement of scattering with complementary media. *Optics Express*, 16(22):18545–50, 2008.

[25] Wee WH and Pendry JB. Shrinking optical devices. *New Journal of Physics*, 11:73033–56, 2009.

[26] Wee WH and Pendry JB. Super phase array. *New Journal of Physics*, 12:033047, 2010.

[27] Yun Lai, Huanyang Chen, Zhao-Qing Zhang, and C. T. Chan. Complementary media invisibility cloak that cloaks objects at a distance outside the cloaking shell. *Phys. Rev. Lett.*, 102:093901–4, 2009.

[28] Yun Lai, Ng Jack, Chen HY, Han DZ, Zhang ZQ, and C. T. Chan. Illusion optics: The optical transformation of an object into another object. *Phys. Rev. Lett.*, 102:253902, 2009.

[29] Pendry JB, Shurig D, and Smith DR. Controlling electromagnetic fields. *Science*, 312:1780–2, 2006.

[30] Misner CW, Thorne KS, and Archibald W. *Gravitation*. W H Freeman and Company, 1973.

[31] Post EJ. *Formal Structure of Electromagnetics: General Covariance and Electromagnetics*. Dover, 1997.

[32] Ward AJ and Pendry JB. Refraction and geometry in maxwells equations. *J. Mod. Opt.*, 43(4):773–93, 1996.

[33] Li Jensen and Pendry JB. Hiding under the carpet: A new strategy for cloaking. *Phys Rev Lett*, 101:203901, 2008.

[34] Valentine J, Li J, Zentgraf T, Bartal G, and Zhang X. An optical cloak made of dielectrics. *Nature Materials*, 8:568–71, 2009.

[35] Liu Y, Zentgraf T, Bartal G, and Zhang X. Transformational plasmon optics. *Nano lett*, 10(6):1997–7, 2010.

[36] Schurig D. An aberration free-lens with zero f-number. *New Journal of Physics*, 10:115034, 2008.

[37] Kundtz N and Smith DR. Extreme-angle broadband metamaterial lens. *Nature Materials*, 9:129–32, 2010.

[38] Zheludev NI. The road ahead for metamaterials. *Science*, 328:582–3, 2010.

[39] Ramakrishna SA and Pendry JB. Removal of absorption and increase in resolution in a near-field lens via optical gain. *Phys. Rev. B*, 67:201101, 2003.

[40] Popov AK and Shalaev VM. Compensating losses in negative-index metamaterials by optical parametric amplification. *Optics Lett*, 31(14):2169–71, 2006.

[41] Sivan Y, Xiao S, Chettiar UK, Kildishev AV, and Shalaev VM. Frequency-domain simulations of a negative-index material with embedded gain. *Optics Express*, 17(26):24060–74, 2009.

[42] Fang A, Koschny Th, Wegner M, and Soukoulis CM. Self-consistent calculation of metamaterials with gain. *Phys Rev B*, 79:241104, 2009.

[43] Dong Z-G, Liu H, Li T, Zhu Z-H, Wang S-M, Cao J-X, Zhu S-N, and Zhang X. Optical loss compensation in a bulk left-handed metamaterial by the gain in quantum dots. *Appl. Phys. Lett.*, 96:02409, 2010.

[44] Wuestner S, Pusch A, Tsakmakidis KL, Hamm JM, and Hess O. Overcoming losses with gain in a negative refractive index metamaterial. *Phys Rev Lett*, 105:127401, 2010.

[45] Xiao S, Drachev VP, Kildishev AV, Ni X, Chettiar UK, Yuan H-K, and Shalaev VM. Loss-free and active optical negative-index metamaterials. *Nature*, 466:735–8, 2010.

[46] Ramakrishna SA and Olivier JM. Resolving the wave vector in negative refractive index media. *Optics letters*, 30(19):2626–8, 2005.

[47] Shadrivov IV, Zharov AA, and Kivshar YS. Giant goos-hanchen effect at the reflection from left-handed metamaterials. *Appl. Phys. Lett.*, 83(13):2713, 2003.

[48] Kosmas LT, Boardman AD, and Hess O. Trapped rainbow storage of light in metamaterials. *Nature*, 450:397–401, 2007.

[49] Ramakrishna SA and Grzegorczyk TM. *Physics and Applications of Negative Refractive Index Materials*. SPIE Press, 2009.

[50] Chen XL, He M, Du YX, Wang WY, and Zhang DF. Negative refraction: An intrinsic property of uniaxial crystals. *Phys. Rev. B*, 72:113111, 2005.

[51] Luo C, Johnson SG, Joannopoulos JD, and Pendry JB. All-angle negative refraction without negative effective index. *Phys Rev B*, 65:201104, 2002.

[52] Depine RA and Lakhtakia A. A new condition to identify isotropic dielectric-magnetic materials displaying negative phase velocity. *Microwave and Opt Tech Lett*, 41(4):315–6, 2004.

[53] Kinsler P and McCall MW. Criteria for negative refraction in active and passive media. *Microwave and Opt Tech Lett*, 50(7):1804–1807, 2008.

[54] Grzegorczyk TM and Kong JA. Electrodynamics of moving media inducing positive and negative refraction. *Phys Rev B*, 74:033102, 2006.

[55] Ziolkowski RW and Heyman E. Wave propagation in media having negative permitivity and permeability. *Phys Rev E*, 64:056625, 2001.

[56] Lindell LV, Tretyakov SA, Nikoskinen KI, and Ilvonen S. Bw media - media with negative parameters capable of supporting backward waves. *Microwave Opt Tech Lett*, 31(2):129–133, 2001.

[57] Tuck C Choy. *Effective medium theory: principles and applications*. Oxford University Press, 1999.

[58] Milton GW. *The theory of composites*. Cambridge University Press, 2002.

[59] Ashcroft NW and Mermin DN. *Solid State Physics*. Brooks Cole, 1976.

[60] O'Brien S and Pendry JB. Magnetic activity at infrared frequencies in structured metallic photonics crystals. *J. Condes. Matt.*, 14(25):6383, 2002.

[61] Zhou J, Koschny Th, Economou EN, Pendry JB, and Soukoulis CM. Saturation of the magnetic response of split ring resonators at optical frequencies. *Phys. Rev. Lett.*, 95:223902, 2005.

[62] Klein MW, Enkrich C, Wegener M, Soukoulis CM, and Linden S. Single-slit split-ring resonators at optical frequencies: limits of size scaling. *Optics Letters*, 31(9):1259–61, 2006.

[63] Tretyakov S. On geometrical scaling of split-ring and double-bar resonators at optical frequences. *Metamaterials*, 1(1):40–43, 2007.

[64] Frankel T. *The Geometry of Physics*. CUP, 2nd edition, 2003.

[65] Lindell IV. *Differential Forms in Electromagnetics*. IEEE, 2004.

[66] Maslovski SI, Tretyakov SA, and Belov PA. Wire media with negative effective permittivity a quasistatic model. *Micro. and Opt. Tech. Lett.*, 35(1):47–51, 2002.

[67] Belov PA, Marques R, Maslovski SI, Nefedov IS, Silveirinha M, Simovski CR, and Tretyakov SA. Strong spatial dispersion in wire media in the very large wavelength limit. *Phys Rev B*, 67:113103, 2003.

[68] Merlin R. Metamaterials and the landau-lifshitz permeability argument: Large permittivity begets high-frequency magnetism. *PNAS*, 106(6):1693–5, 2009.

[69] O'Brien S and Pendry JB. Photonic band-gap effects and magnetic activity in dielectric composites. *J. Condes. Matt.*, 14(15):4035, 2002.

[70] Bohren CF and Huffman DR. *Absorption and Scattering of Light by Small Particles*. Wiley-Interscience, 1998.

[71] Bohren CF. Applicability of effective medium theories to problems of scattering and absorption by non-homogeneous atmospheric particles. *J. Atmos. Sci.*, (43):468–475, 1986.

[72] O'Brien S, MacPeake D, Ramakrishna SA, and Pendry JB. Near infrared photonic bandgaps and non-linear effects in negative magnetic materials. *Phys Rev B*, 69:241101, 2004.

[73] Tretyakov SA, Shivola AH, Sochava AA, and Simovski CR. Magnetoelectric interactions in bi-anisotropic media. *J. Electromagn. Waves Appl.*, 12(4):481–97, 1998.

[74] Demetriadou A and Pendry JB. Extreme chirality in swiss roll metamaterials. *J. Condes. Matt.*, 21(37):376003, 2009.

[75] Pendry JB. A new route to negative refraction. *Science*, 306:1353–5, 2004.

[76] Padilla WJ. Group theoretical description of artificial electromagnetic metamaterials. *Optics Express*, 15(4):1639, 2007.

[77] Kafesaki M, Tsiapa I, Katsakrakis N, Koschny, Soukoulis C M, and Economou E N. Left-handed metamaterials: The fishnet structure and its variations. *Phys Rev B*, 75:235114, 2007.

[78] Aubry A, Lei DY, Maier S Fernandez-Domninguez AI, Sonnerfraud Y, and Pendry JB. Plasmonic light-harvesting devices over the whole visible spectrum. *Nano lett*, 10(7):2574–2579, 2010.

[79] Luo Y, Pendry JB, and Alexandre Aubry. Surface plasmons and singularities. *Nano lett*, 10(10):4186–4191, 2010.

[80] Schurig D, Pendry JB, and Smith DR. Calculation of material properties and ray tracing in transformation media. *Optics Express*, 14(21):9794–804, 2006.

[81] Leonhardt U and Philbin TG. Transformation optics and the geometry of light. *Prog. Opt.*, 53:69–152, 2009.

[82] Bergamin L. Generalized transformation optics from triple spacetime metamaterials. *Phys Rev A*, 78(4):043825, 2010.

[83] Bergamin L and Favaro A. Negative index of refraction, perfect lenses and transformation optics - some words of caution. *arXiv:1001.4655v1*, 2010.

[84] Leonhardt U and Philbin TG. General relativity in electrical engineering. *New Journal of Physics*, 8:247, 2006.

[85] Chen X, Luo Y, Zhang J, Jiang K, Pendry JB, and Zhang S. Macroscopic invisibility cloaking of visible light. *Nature Comm.*, 2(176):1–6, 2011.

[86] Milton GW, Nicorovici NP, McPhedran RC, and Podolskiy VA. A proof of superlensing in the quasistatic regime, and the limitations of superlenses in this regime due to anomalous localized resonance. *Proc. R. Soc. A*, 461:3999–4034, 2005.

[87] Graeme W Milton, Nicolae-Alexandru P Nicrovici, Ross C McPhedran, Kirill Cherednichenko, and Zubin Jacob. Solutions in folded geometries, and associated cloaking due to anomalous resonance. *New Journal of Physics*, 10:115021 – 41, 2008.

[88] Jacob Z, Alekeyev LV, and Narimanov E. Optical hyperlens: Far-field imaging beyond the diffraction limit. *Optics Express*, 14(18):8247–56, 2006.

[89] Salandrino A and Engheta N. Far-field subdiffraction optical microscopy using metamaterial crystals: Theory and simulations. *Phys Rev B*, 74:075103, 2006.

[90] Liu Z, Lee H, Xiong Y, Cheng S, and Zhang X. Far-field optical hyperlens magnifying sub-diffraction-limited objects. *Science*, 315:1686, 2007.

[91] Pendry JB. Perfect cylindrical lenses. *Optics Express*, 11:755–60, 2003.

[92] Gomez Santos G. Universal features of the time evolution of evanescent modes in a left-handed perfect lens. *Phys. Rev. Lett.*, 90:077401, 2003.

[93] Wee WH and Pendry JB. Universal evolution of perfect lenses. *Phys Rev Lett*, 106:165503, 2011.

[94] Markos P and Soukoulis CM. *Wave Propagation - From electrons to photonics crystals and left-handed materials.* Princeton University Press, 2008.

[95] Arfken GB and Weber HJ. *Mathematical Methods For Physicists.* Academic Press, 6th edition, 2005.

[96] Van de Hulst HC. *Light Scattering by Small Particles.* Dover, 1981.

[97] Toshiyuki Takatsuji, Mitsuo Goto, Sonko Osawa, Ruimin Yin, and Tomizo Kurosawa. Whole-viewing-angle cat's-eye retroreflector as a target of laser trackers. *Meas. Sci. Technol.*, 10:N87–N90, 1999.

[98] Pendry JB and Ramakrishna SA. Near field lenses in two dimensions. *J Phys.: Condens. Matter*, 14:1–17, 2002.

[99] Maystre D, Enoch S, and McPhedran R. Why a harmonic solution for lossless, perfectly homogeneous, left-handed material cannot exist. *J Opt. Sci. A*, 25(8):1937–43, 2008.

[100] Merlin R. Analytical solution of the almost-perfect-lens problem. *Appl. Phys. Lett.*, 84:1291–2, 2003.

[101] Smith DR, Schurig D, Rosenbluth M, Schultz S, Ramakrishna SA, and Pendry JB. Limitations on subdiffraction imaging with a negative refractive index slab. *Appl. Phys. Lett.*, 82(10):1506–8, 2003.

[102] Merlin R. Analytical solution of the almost-perfect-lens problem. *Appl. Phys. Lett.*, 84:1290, 2004.

[103] Morse PM and Feshbach H. *Methods of Theoretical Physics*. McGraw-Hill, 1953.

[104] Raether H. *Excitation of plasmons and Interband Transitions by electrons*. Springer-Verlag, 1980.

[105] Boardman AD, Rapoport YG, King N, and Malnev VN. Creating stable gain in active metamaterials. *JOSA B*, 24:A53–A61, 2007.

[106] Boardman AD, King N, Mitchell-Thomas RC, Malnev VN, and Rapoport YG. Gain control and diffraction-managed solitons in metamaterials. *Metamaterials*, 2:145–154, 2008.

[107] Pendry JB. Time reversal and negative refraction. *Science*, 322:71–3, 2008.

[108] Aubry A and Pendry JB. Mimicking a negative refractive slab by combining two phase conjugators. *JOSA B*, 27(1):72–84, 2010.

[109] Wee WH and Pendry JB. Looking beyond the perfect lens. *New Journal of Physics*, 12:053018, 2010.

[110] Maslovski S and Tretyakov S. Phase conjugation and perfect lensing. *J Appl Phys*, 94(7):4241–3, 2003.

[111] 't Hooft GW. Comment on negative refraction do not make a perfect lens. *Phys. Rev. Lett.*, 87:249701, 2001.

[112] Pendry JB. Comment on negative refraction do not make a perfect lens. *Phys. Rev. Lett.*, 87:249702, 2001.

[113] Yariv A and Pepper DM. Amplified reflection, phase conjugation and oscillation in degenerate four-wave mixing. *Optics Lett.*, 1(1):16–18, 1977.

[114] Avizonis PV, Hopf FA, Bomberger WD, Jacobs SF, Tomita A, and Womack KH. Optical phase conjugation in lithium formate crystal. *Appl. Phys. Lett.*, 31:435–437, 1977.

[115] Lefort L and Barthelemy A. Revisiting optical phase conjugation by difference-frequency generation. *Opt. Lett.*, 21:848–50, 1996.

[116] Giuliano CR. Applications of optical phase conjugation. *Phys. Today*, 34(4):27–35, 1981.

[117] Hellwarth RW. Generation of time-reversed wave fronts by nonlinear refraction. *J. Opt. Soc. Am.*, 67:1–3, 1977.

[118] Bloom DM and Bjorklund GC. Conjugate wave-front generation and image reconstruction by four-wave mixing. *Appl. Phys. Lett.*, 31:592–594, 1977.

[119] Bloom DM, Liao PF, and Economou NP. Observation of amplified reflection by degenerate four-wave mixing in atomic sodium vapor. *Opt. Lett.*, 2:58–60, 1978.

[120] Pepper DM, Fekete D, and Yariv A. Observation of amplified phase-conjugate reflection and optical parameteric oscillation by degenerate four-wave mixing in a transparent medium. *Appl. Phys. Lett.*, 33:41–44, 1978.

[121] Abrams RL and lind RC. Degenerate four wave mixing in absorbing media. *Opt. Lett.*, 2:94–96, 1978.

[122] Tomita A. Phase conjugation using gain saturation of a nd:yag laser. *Appl. Phys. Lett.*, 34:463–464, 1979.

[123] Fisher RA and Feldman BJ. On-resonant phase conjugate reflection and amplification at 10.6 microns in inverted co2. *Opt. Lett.*, 4:140–142, 1979.

[124] Feinberg J, Heiman D, Tanguay JAR, and Hellwarth RW. Photorefractive effects and light-induced charge migration in barium titanate. *J. Appl. Phys.*, 51:1297–1305, 1980.

[125] Feinberg J and Hellwarth RW. Phase-conjugating mirror with continuous-wave gain. *Opt. Lett.*, 5:519–521, 1980.

[126] White JO, Cronin-Golomb M, Fischer B, and Yariv A. Coherent oscillation by self-induced gratings in the photorefractive crystal batio3. *Appl. Phys. Lett.*, 40:450–2, 1982.

[127] Scott AM. Efficient phase conjugation by brillouin enhanced four wave mixing. *Opt. Comm.*, 45(2):127–132, 1983.

[128] Hellwarth RW. Theory of phase conjugation by stimulated scattering in a waveguide. *J. Opt. Soc. Am.*, 68:1050–6, 1978.

[129] Khyznika A, Kondilenko V, Kucherov Y, Lesnik S, Odoulov S, and Soskin M. Phase conjugation by degenerate four-wave mixing. *J. Opt. Soc. Am. A*, 1:169–175, 1984.

[130] Bledowski A, Krolikowski W, and Kujawski A. Forward phase conjugate-wave in four-wave mixing in photorefractive media. *Opt. Commun.*, 61:71–74, 1987.

[131] Tang SH, He XH, and Zhang HY. Experimental study of the forward phase-conjugate wave in degenerate four-wave mixing in linbo3:fe. *J. Eur. Opt. Soc. B*, 3:179–183, 1991.

[132] Wang F, Liu L, and Li G. Self-pumped forward and backward phase conjugator with cu-doped knsbn crystal: caused by scattering oscillation-amplification. *Quant. Opt.*, 134:195–8, 1997.

[133] Gunter P and Huignard JP. *Photo-refractive Materials and their applications.* Springer-Velag, 1988.

[134] Ujihara K. Four-wave mixing and two dimensional phase conjugation of surface plasmons. *Opt. Commun.*, 42(1):1–4, 1982.

[135] Bozhevolnyi SI, Keller O, and Smolyaninov II. Phase conjugation of an optical near field. *Opt. Lett.*, 19:1601–3, 1994.

[136] Bozhevolnyi SI, Keller O, and Smolyaninov II. Scattered light enhancement near a phase conjugating mirror. *Opt. Commun.*, 115:115–120, 1994.

[137] Vohnsen B and Bozhevolnyi SI. Near-field optical microscopy with a phase-conjugating mirror. *Opt. Commun.*, 148:331–337, 1998.

[138] Fischer RA, Suydam BR, and Feldman BJ. Transient analysis of kerr-like phase conjugators using frequency domain techniques. *Phys. Rev. A*, 23:3071–3083, 1981.

[139] Sivan Y and Pendry JB. Time reversal in dynamically tuned zero-gap periodic systems. *Phys. Rev. Lett.*, 106:193902, 2011.

[140] Fink M. Time reversed acoustics. *Physics Today*, 50(3):34–40, 1997.

[141] Lerosey G, Rosny J, Tourin A, and Fink M. Focusing beyond the diffraction limit with far-field time reversal. *Science*, 315:1120–22, 2007.

[142] Ramakrishna SA, Pendry JB, Wiltshire MCK, and Stewart WJ. Imaging the near-field. *J Mod. Opt.*, 50:1419–30, 2003.